ULTRASOUND ELASTOGRAPHY TECHNIQUES FOR THE THERAPEUTIC MONITORING OF BREAST CANCER

Andrew Di Battista
Wolfson College



Supervisor: Prof. Alison Noble

Institute for Biomedical Engineering
Department of Engineering Science
University of Oxford

Trinity Term, 2011

This thesis is submitted to the Department of Engineering Science, University of Oxford, in partial fulfillment of the requirements for the degree of Doctor of Philosophy. The thesis is entirely my own work and, except where otherwise stated, describes my own research.

Andrew Di Battista, Wolfson College, Oxford

Copyright © 2011 by Andrew Di Battista
All Rights Reserved

ULTRASOUND ELASTOGRAPHY TECHNIQUES FOR THE THERAPEUTIC MONITORING OF BREAST CANCER

Andrew Di Battista, Wolfson College, Oxford
Submitted for the degree of Doctor of Philosophy
Trinity Term, 2011

ABSTRACT

The composition, distribution and interaction of tissues found in tumours and their surrounding stroma has to date revealed a wealth of information about cancer biology. There exists a strong need to be able to measure these properties *in vivo* in order to provide further understanding and ultimately lead to better treatment for cancer patients.

These interactions can manifest themselves in the form of distinctive biomechanical properties which ultrasound elastography, an image processing technique used to evaluate tissue stiffness, is particularly well suited to monitor. Much focus of elastography in breast cancer has been on diagnosis. However, it has always lacked the selectivity and sensitivity to be of reliable use in clinic. Moreover, with simple biopsies taken as the gold standard, the position of diagnostic tool has already been filled. The focus of this doctoral research has been to evaluate the role elastography can play in breast cancer after diagnosis, when therapy begins.

Modifications and new applications of the technique were an essential part of this research. A new robust and efficient elastography algorithm was developed to meet the demands of freehand elastography imaging. In addition, a method for defining outlying data in strain images was produced which led to a technique for normalising and displaying images with a consistent colour mapping scheme.

With the basic framework in place, the exploration into the non-linear properties of tissue was carried out using hybrid freehand imaging of viscoelasticity (HYFIVE) which took advantage of high ultrasound frame rates to measure tissue creep responses. The HYFIVE system was comprised of a novel probe canister device that was capable of acquiring < 2s worth of data to produce good measures of tissue viscosity.

An experiment to show the ability of elastography to improve tumour sizing revealed a significant accuracy increase (~20%) over conventional ultrasound B-mode.

A final experiment exploited tumour/stroma behaviour to follow the response of neo-adjuvant breast cancer patients over multiple cycles of chemotherapy. Results from a pilot study suggest that elastography, in conjunction with standard B-mode, could be used as an early indicator to tumour response, with greater sensitivity over conventional ultrasound analysis.

All of the results show that ultrasound elastography can significantly contribute to the understanding of breast cancers and provide viable clinical tools to put to practical use.

ACKNOLEDEGMENTS

First and foremost, I would like to thank my supervisor, Prof. J. Alison Noble for her help, support and guidance through the long process of this thesis project.

In addition, this project would not have been possible without the cooperation of the entire Churchill Breast Care Unit of the Oxford Radcliffe NHS Trust. I would like to give special thanks to Dr. Ruth English, consultant radiologist for her incredible enthusiasm and devotion to this research. A special thanks also goes out to Dr. Rosie Adams, Dr. Vaishali Parukelar and Dr. Jane Baldwin for their participation in the scanning room.

I would also like to thank my degree funders, both at Wolfson College and at the Clarendon Scholarship Fund, for giving me the opportunity to study at Oxford.

Finally, I would like to thank Lexi who has encouraged and motivated me every step of the way, keeping me on track and helping me get over those DPhil blues!

Table of Contents

List of Figures viii
List of Tables xi
Glossary xii
Chapter 1 1
1.1 Motivation 1
1.2 Aims & Objectives 2
1.3 Clinical Application Areas 3
1.4 Contributions 3
1.5 Organization 4
1.6 Published Work 4
Chapter 2 5
2.1 Introduction 5
2.2 Biology & Medicine 5
2.2.1 Cancer of the Breast 5
2.2.2 Breast Cancer Screening 8
2.2.3 Cancer Diagnosis: To Biopsy or not to Biopsy? 9
2.2.4 Patient Management: BI-RADS and Breast Density 11
2.2.5 Therapeutic Monitoring of Cancer 13
Current State of Art in Imaging Tumour Response 14
DCE-MRI 14
FDG-PET 15
2.3 Tissue Modelling and Imaging for Elastography 18
2.3.1 Strain and the Elastic Model 18
Physics of Strain and Biomechanics 18
Stress and Strain 18
Generalized Hooke's Law 20
Poisson's Ratio 22
Modelling for Elastography 23
2.3.2 Ultrasound Imaging 25
IQ Demodulation and Envelope Detection 26
The Linear System Model 28
Speckle 29
2.4 Related Work in Elastography 30

2.4.1 ARFI and Shear Wave Imaging 30
Qualitative Imaging 32
Quantitative Imaging 32
ARFI Assumptions 33
2.4.2 MR Elastography 35
2.4.3 Quasi-Static Methods for Displacement and Strain Estimation 36
Displacement Estimation 37
Other Methods for Motion Tracking 40
Strain Estimation 41
2.5 CONCLUSION 42
Chapter 3 44
3.1 Introduction 44
3.2 Tissue Model 44
3.3 Displacement Estimation 45
3.3.1 Integral Images 45
2D Integral Images 46
3D Integral Volumes 47
3.3.2 Similarity Metrics 50
3.4 Strain Calculation 52
3.5 Experiments 56
3.5.1 1D Simulations 57
3.5.2 2D Experiments 61
Experimental setup 2D 61
Strain Ratios 63
Effects of Window Size 65
Effects of Down Sampling 67
2.5.3 3D Experiments 69
Clinical Data 76
Computation Times 78
3.6 Discussion 78
3.6.1 1D Simulations 78
3.6.2 2D and 3D Experiments 79
3.7 Conclusion 80
Chapter 4 82

4.1 Introduction 82
4.2 Quality Metrics 82
4.3 Normalization and Display 89
4.4 Conclusion 95
Chapter 5 96
5.1 Introduction 96
5.2 Materials and Methods 98
5.2.1 Hardware 98
Scanning Setup 99
5.2.2 Tissue Model, Derivation & Curve Fitting 100
5.3 Results 105
5.3.1 Phantom Experiment 105
Repeatability 107
5.3.2 Clinical Data Experiments 108
5.4 Discussion 112
5.5 Conclusion 114
Chapter 6 116
6.1 Introduction 116
6.2 Methods 117
6.2.1 Hardware Setup and Scanning Protocols 117
6.2.2 Data Selection Process and Analysis 118
6.2.3 Segmentation and Sizing 120
6.3 Sizing Results 124
6.3.1 Patient Summary 124
6.3.2 Exemplar Results 124
6.3.3 Statistical Results 127
6.4 Discussion 131
6.5 Conclusion 133
Chapter 7 134
7.1 Introduction 134
Motivation 134
7.2 Patients & Methods 135
7.2.1 Overview 135
7.2.2 Patient Recruitment 136

Scanning Protocol 136
7.2.3 Patient Dropouts\Exclusions 138
7.2.4 Imaging and Metrics (post processing) 138
The strain ratio metric 139
7. 3 RESULTS 141
7.3.2 Results from Tumour Response 141
A complete dataset 141
Sensitivity of ratio 144
7.3.3 Additional Cases 146
Incomplete Data Sets 147
Lymph Nodes 149
7.4 Discussion 151
7.5 Conclusion 153
Chapter 8 155
Summary 155
Future Work 156
3D Elastography 156
Probe Canister (HYFIVE) 157
Tumour Sizing 158
NeoAdjuvant Study 158
Appendix A 160
Coordinates Systems in Medical Imaging 160
Appendix B 161
Area Measurements Using Polygon Decomposition Method 161
REFERENCES 163

List of Figures

Figure 2.1 - Anatomy of the Breast 6
Figure 2.2 - Ultrasound Images of Cyst, Fibroadenoma and Carcinoma 8
Figure 2.3 - Tissue Elastic Modulus for Different Breast Tissue Types 11
Figure 2.4 - Tumour Stages and Stromal Activation 16
Figure 2.5 - Before and After Treatment Histology of Breast Cancer 17
Figure 2.6 - Stress and Strain 19
Figure 2.7 - Infinitesimal Strain 19
Figure 2.8 - Stress vs. Strain curves for different tissue types found in the breast 21
Figure 2.9 - The Poisson Effect 22
Figure 2.10 - Effect of Constrained Young's Modulus 25
Figure 2.11 - B-mode Image Generation 26
Figure 2.12 - IQ Demodulation 27
Figure 2.13 - Linear Model and PSF 29
Figure 2.14 - ARFI 31
Figure 2.15 - Illustration of Block Matching Algorithm 37
Figure 2.16 - Dynamic Programming Method 40
Figure 2.17 - Least Squares Gradient Estimation (LSGE) 41

Figure 3.1 - Integral Image Method: 2D 47
Figure 3.2 - Integral Image/Volume Method: 3D 48
Figure 3.3 - Calculation of Integral Volume 49
Figure 3.4 - Theoretical Signal Spectrums of pre and post compression signals 52
Figure 3.5 - Effects of Sample Rate on Strain Estimate Precision 55
Figure 3.6 - Simulated 1D Pre and Post Compression Signals 58
Figure 3.7 - Effects of Window Size on Displacement Estimate Error 59
Figure 3.8 - Comparison of Strain Estimate Methods 60
Figure 3.9 - Gradient vs. Spectral Shift Method 61
Figure 3.10 - Hardware Setup for Zonare Research Package 62
Figure 3.11 - Phantom Experiment 1 Results 63
Figure 3.12 - Phantom Experiment 1 Repeated 64
Figure 3.13 - Phantom Exp.2: Varying Displacement Field Precision (Spec. Method) 66
Figure 3.14 - Phantom Exp.2: (LSGE Method) 67
Figure 3.15 - Phantom Experiment 3: Varying Axial Sample Rate (Spectral Shift Method) 68
Figure 3.16 - Phantom Experiment 3: Varying Axial Sample Rate (LSGE Method) 69
Figure 3.17 - The C8-3 3D probe from Zonare 70
Figure 3.18 - Experimental Setup for 3D phantom studies 71
Figure 3.19 - 3D Results (CIRS Phantom) 72
Figure 3.20 - 3D Results: Repeated Scans(a-d) 73
Figure 3.21 - Clinical Data: Comparison of 2D and 3D B-mode data 76
Figure 3.22 - Clinical Data: 3D data 77
Figure 3.23 - Clinical Data: Comparison of 2D and 3D Strain data 78

Figure 4.1 - Signal Decorrelation in Olive Phantom 83
Figure 4.2 - Quality Metric Mask Generation 85
Figure 4.3 - Quality Metric Mask Sensitivity 86
Figure 4.4 - Signal Decorrelation in Homogeneous Phantom 87
Figure 4.5 - Signal Decorrelation in Circular Inclusion Phantom 88

Figure 4.6 - Signal Decorrelation with Depth 89
Figure 4.7 - The Effects of Dynamic Range on Colour Mapping 90
Figure 4.8 - Histogram Equalization 91
Figure 4.9 - Histogram Equalization(2) 92
Figure 4.10 - Histogram Equalization(3) 93
Figure 4.11 - Histogram Equalization(4) 94
Figure 4.12 - Effects of Histogram Equalization on Discretely Distributed Data 95

Figure 5.1 - Diagram and Photo of Probe Canister Device 98
Figure 5.2 - Canister Device in Operation and Resulting Applied Force 99
Figure 5.3 - The Kelvin-Voigt Model 100
Figure 5.4 - Axial Load Modelled as Ramp Function 101
Figure 5.5 - Experimental Data and Curve Fit 105
Figure 5.6 -(a)(b) Experiment 1- Phantom Data: Strain, Viscosity Images 107
Figure 5.7 - Experiment 2- P1 Data: Strain, Viscosity Images 109
Figure 5.8 - Experiment 3- P1 Data: Failed Acquisition 110
Figure 5.9 - Experiment 4- P2 Data: Strain, Viscosity Images 111
Figure 5.10 - Experiment 5- P3 Data: Strain, Viscosity Images 111
Figure 5.11 - Experiment 6- P4 Data: Strain, Viscosity Images 112

Figure 6.1 - The Zonare L10-5 Probe 117
Figure 6.2 - GUI for Analysing Elastography Data 120
Figure 6.3 - GUI Developed for Manual Segmentation 122
Figure 6.4 - Segmentation Bias and Error Modelling 123
Figure 6.5 - Segmentation Results (1) 125
Figure 6.6 - Segmentation Results (2) 125
Figure 6.7 - Segmentation Results (3) 126
Figure 6.8 - Segmentation Results (4) 126
Figure 6.9 - Segmentation Results with Posterior Shadowing 127
Figure 6.10 - B-mode vs. B+E mode Sizing Results 128
Figure 6.11 - B-mode vs. B+E mode Sizing Results (10% Shrinkage) 128
Figure 6.12 - B-mode vs. B+E mode Accuracy 129
Figure 6.13 - B-mode vs. B+E mode Accuracy (10% Shrinkage) 130
Figure 6.14 - Segmentation Error as a Function of Tumour Size 131

Figure 7.1 - Coils and Calcification used as Imaging Landmarks 138
Figure 7.2 - P1 Dataset (7 chemo cycles): Transverse Plane 141
Figure 7.3 - P1 Dataset (7 chemo cycles): Sagittal Plane 141
Figure 7.4 - Tumour and Peritumour Segmentation 142
Figure 7.5 - Strain Ratio Plots with Tumour Size Comparison (Sagittal) 143
Figure 7.6 - Strain Ratio Plots with Tumour Size Comparison (Transverse) 143
Figure 7.7 - Strain Ratio Sensitivity to Tumour Segmentation 145
Figure 7.8 - Strain Ratio Sensitivity to Peri-Tumour Segmentation 145
Figure 7.9 - P5 Dataset (7 cycles): Sagittal Plane 146
Figure 7.10 - Severe Posterior Shadowing and the Effects on Segmentation 146
Figure 7.11 - P5: Strain Ratio and Tumour Size Plots 147
Figure 7.12 - P3: Rapid Tumour Response 147
Figure 7.13 - Results from a Partial Dataset (1) 148
Figure 7.14 - Results from a Partial Dataset (2) 148
Figure 7.15 -(a,b) Lymph Node Response to Chemotherapy (1) 149

Figure 7.16 - Lymph Node Elasticity 150
Figure 7.17 - Lymph Node Elasticity (2) 150

Figure A.1 - Probe Coordinate System 160
Figure A.2 - Nomenclature of Coordinate Systems in Medical Imaging 160
Figure B.1 - Polygon Decomposition Method 161

List of Tables

Table 2.1 - Benign Lesions Found in Breast Tissue 7
Table 2.2 - BI-RADS Scoring System 11
Table 3.1 - Integral Volumes: Vertices and Signs Lookup Table 49
Table 5.1 - HYFIVE Patient Summary 108
Table 6.1 - Strain Algorithm Parameters 119
Table 6.2 - Patient Summary 124
Table 6.3 - Summary of Segmentation Results 130
Table 7.1 - Neoadjuvant Study: Patient Summary 136

Glossary

US - Ultrasound

RF - Radio Frequency

CC - Cross Correlation

NCC - Normalized Cross Correlation

SSD - Sum of Squared Differences

SAD - Sum of Absolute Differences

GUI - Graphical User Interface

MMSE - Minimum Mean Squared Error

HEQ - Histogram Equalization

LSGE - Least Squares Gradient Estimation

ROI - Region of Interest

IQ - In Phase and Quadrature Phase

DCIS - Ductal Carcinoma in situ

IDC - Invasive Ductal Carcinoma

LCIS - Lobular Carcinoma in situ

ILC - Invasive Lobular Carcinoma

HYFIVE - Hybrid Freehand Imaging of ViscoElasticity

PSF -Point Spread Function

MR - Magnetic Resonance

Chapter 1
Introduction

1.1 Motivation

This thesis explores the contributing role of quasi-static ultrasound elastography techniques to help solve the problem of breast cancer therapy monitoring and management. The aim of the following chapters is to make clear why elastography was chosen as a suitable imaging method, why ultrasound was the preferred imaging modality and why quasi-static methods above all were implemented. Encouraging results from this thesis's work will provide motivation for future research in this field.

Quasi-static ultrasound elastography is a technique used to measure the stiffness of tissues *in vivo* using conventional ultrasound imaging [1-10]. Principally, it involves taking a pair of images of the same region taken under different external stresses, tracking the relative motion incurred and measuring the amount of deformation that has taken place. If it is assumed that the internal stresses in the tissue are evenly distributed across the image plane, then the tissue stiffness can be inferred from the amount of deformation.

Because breast tumours often exhibit higher stiffness relative to their surrounding tissue [11-13], elastography is capable of providing high contrast images of lesions as well as quantitative measures of cancers in vivo. These *elastograms* or *strain images* have been used in the detection and diagnosis of malignant lesions.

Much of the focus of elastography research has long been on cancer detection and diagnosis with the aim to reduce the number of avoidable core biopsies [14-17]. This has also been the primary selling point of commercially available elastography systems from the likes of Siemens and Hitachi [18-19]. However, for a number of reasons which will be highlighted in the next chapter, elastography alone is unsuitable for use in a clinical *diagnostic* role. It has been at best helpful to clinicians providing complementary information to standard ultrasound B-mode and mammography, but generally lacks the sensitivity and specificity performance required for breast cancer screening.

It is thus no surprise that despite having been around for several decades, elastography has yet to break through into main stream clinical imaging; it remains a topic of research. It is of particular interest to understand why this is still the case and necessarily explore new avenues for this nonetheless promising technology.

1.2 Aims & Objectives

The primary aim of this work has been to improve upon existing elastography methods and search for new clinical applications of these techniques. The main feature of this research is an investigation into the relatively recent development of the clinical use of elastography in assessing breast tumour size and reaction to chemotherapy.

The primary argument for the use of ultrasound in particular over other imaging modalities is its relatively low cost, minimal scan duration and non-invasiveness. If it can be demonstrated that ultrasound elastography can suitably monitor cancer patients,

then it would have tremendous advantages over current emerging techniques like DCE-MRI and FDG-PET, both of which will be described further in Chapter 2.

1.3 Clinical Application Areas

Elastography is not exclusive to breast cancer, nor is it even limited to ultrasound (US) imaging. Both US and MR elastography [20-26] have been applied to the monitoring and diagnosis of a range of illnesses including but not exclusive to:

- Prostate cancer
- Liver fibrosis
- Thyroid disease
- Testicular cancer

Many of the techniques presented in this thesis (Chapter 3 and Chapter 4 in particular) are portable to these other clinical application areas.

Elastograms also have a use in tumour sizing [8,12] and could consequently guide surgeons with their excisions of cancerous tissue. In the case of breast cancer, accurate size information can have profound effects on treatment alternatives; making the difference between a small excision and a total mastectomy.

1.4 Contributions

This thesis presents several contributions to elastography research; they can be listed as:

- An efficient Block Matching Displacement estimator using a combination of integral images/volumes with standard similarity metrics (Chapter 3)

- An efficient and robust Spectral Shift Strain estimator (Chapter 3)
- A novel Hybrid Freehand approach to Imaging Visco-Elasticity (HYFIVE) of tissue (Chapter 5)

1.5 Organization

This thesis is organized into 8 chapters. Chapter 2 will provide the reader with the relevant background information ranging from clinical to engineering challenges of breast cancer imaging. Chapters 3 will present the proposed strain estimation algorithm. Chapter 4 will discuss the issue of data quality assessment and image normalization and display. The real clinical experiments first begin in Chapter 5, which will describe HYFIVE. Chapters 6 and Chapter 7 will focus on the clinical results from a study to examine the use of elastography for breast lesion sizing and tumour response to chemotherapy, respectively. A summary of the work presented in this thesis and interesting and motivational prospects for future work will be a focus of Chapter 8.

1.6 Published Work

A number of publications have been published on the research which are listed below:

Andrew Di Battista, J. Alison Noble "A fast and robust 3D ultrasound strain imaging algorithm for freehand scanning" *IEEE Proceedings from ISBI 2011*, pp. 528 - 531

Andrew Di Battista, J. Alison Noble, Ruth English, "Ultrasound imaging of breast lesions: a practical hybrid freehand technique for data acquisition", *Proceedings from the ASME International Mechanical Engineering Congress and Exposition*, Nov. 2011

As well as 2 posters presented at the Royal College of Radiology (RCR) Conference

English R, Di Battista A, ParulekarV, Adams RF, Baldwin JE, Noble JA "Ultrasound of the breast: a pictorial review of representative elasticity images of benign and malignant breast disease from eleven patients taking part in a study into early breast cancer" *RCR 2010*

English R, Di Battista A, Winter L, Adams RF, Noble JA, "Pilot study: The use of ultrasound elasticity imaging to monitor the response of a primary breast cancer to neoadjuvant chemotherapy", *RCR 2011*, available online from the World Wide Web:< www.rcrbreastgroup.
org/media/asm/2011Posters/P.43.pdf>

Chapter 2
Background

2.1 Introduction

This chapter provides the necessary background to help the reader appreciate both the clinical and technical aspects of elastographic imaging. Section 2.2 gives an overview of breast cancer, screening protocols and therapeutic methods in order to provide the motivation for new non-invasive imaging techniques in breast cancer therapy. Section 2.3 provides a background into the physics and modelling of tissue deformation and how ultrasound images are generated. Section 2.4 will present related work in elastography; providing a means of comparing the proposed technique to existing state of art methods. The chapter will conclude with a discussion of the role of elastography in a clinical environment, its limitations and advantages, and hopefully convince the reader of the value of quasi-static methods in the context of today's technology.

2.2 Biology & Medicine

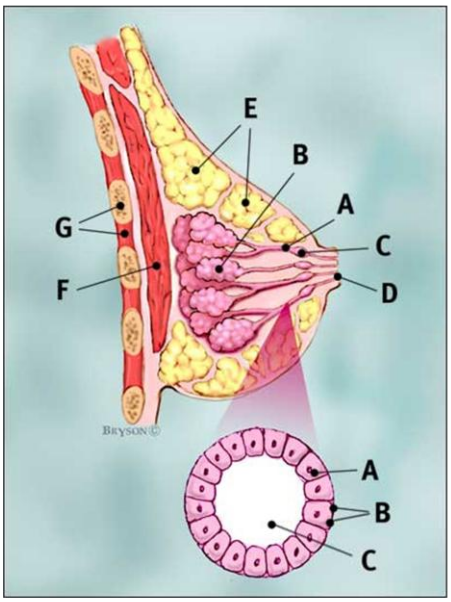
2.2.1 Cancer of the Breast

In simplest terms, cancer is characterised by uninhibited cell proliferation resulting in tumour growth [27]. Cells communicate to each other by sending signals in the form of chemicals (e.g. hormones). In addition, each cell has receptors (analogous to a radio antenna) which receive or, more accurately, bind with a specific hormone to initiate a specific cell response. Mutations in cancer cells lead them to misinterpret or over

express these signals resulting in unrestrained cell mitosis. Understanding these signalling mechanisms and how their breakdown (or combination of breakdowns) leads to tumour development is the major focus of cancer research. There are many known causes for cell mutations ranging from viral infection, genetic aberrations and chemical or radiation exposure. Linking these causes to a specific form of cancer is key to developing effective treatments.

The vast majority of malignant tumours in the breast appear as ductal or lobular carcinomas, accounting for approximately 90% of all breast cancers [28]. *Carcinomas* are tumours which originate from the epithelial (lining) layer of organ tissue and are the most common form of cancer in the body.

The types of tissue typically found in the breast are shown in Figure 2.1; it is made up mostly of adipose (fat) tissue and also features numerous milk ducts and lobules (milk producing glands).



Breast profile:
A ducts
B lobules
C dilated section of duct to hold milk
D nipple
E fat
F pectoralis major muscle
G chest wall/rib cage

Enlargement:
A normal duct cells
B basement membrane
C lumen (center of duct)

Figure 2.1- Anatomy of Breast. Image adapted from (*http://www.breastcancer.org/pictures/breast_anatomy/image_1.jsp*)

Though a breast tumour in itself may not be dangerous, if it metastasizes it can be life threatening. Cancers demonstrating this potential are referred to as invasive or infiltrating; examples being IDC (Invasive Ductal Carcinoma) and ILC (Invasive Lobular Carcinoma). These tumours breakthrough the epithelial layer (basement membrane) and spread throughout the breast. Once these cells infiltrate the lymphatic system they can infect the entire body. Cancers that have yet to display this tendency are said to remain *in-situ*, e.g. DCIS (ductal carcinoma in situ) and LCIS (lobular carcinoma in situ). Various other tumour types can be found in the breast, however these categories describe only part of the complete picture. Extensive histopathology from biopsies reveals which hormones (if any) a tumour is sensitive to; as mentioned above and later in Section 2.2.5, this plays a key decision role in terms of treatment. It is also not uncommon for anomalous *non-cancerous* growths to occur. Cysts and fibroadenomas affect 1 in 5 women in their lifetime [29]. A description of these lumps can be found in Table 2.1.

Table 2.1- Benign lesions found in the breast

	Description
Cysts	Fluid filled sacs, typically lobular in shape. They can travel within the breast tissue and can even gain or lose fluid affecting its size.
Fibroadenomas	Growth of fibrous scar-like tissue, rubbery texture, can move easily under skin, more common to younger women.

Cancerous growths typically have more random shapes, satellite growths and exhibit increased angiogenesis. They show a tendency for multifocal and multicentric distribution [30]. Moreover, cancer cells tend to be 'stiffer' then normal tissue [31]; it is this feature that is exploited by *all* elastography techniques.

Tumours also alter the extra cellular matrix (ECM) surrounding them giving them distinct mobility characteristics relative to normal healthy tissue [32], namely they show a tendency to 'slip' in and out of the imaging plane more easily. Despite all these characteristics, distinguishing one lump from another from a single image can be extremely challenging for clinicians, as Figure 2.2 demonstrates.

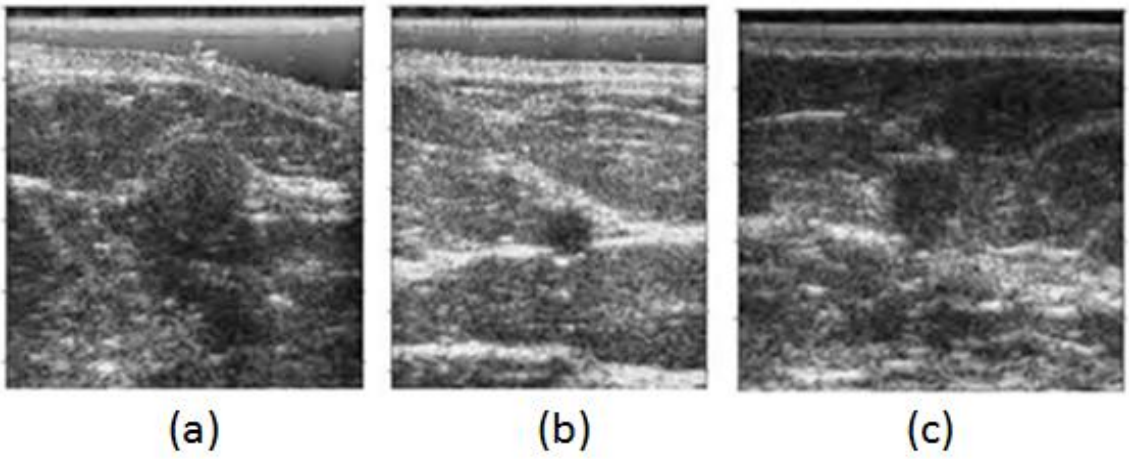


Figure 2.2- (a) Ultrasound Image of a Cysts, (b) Fibroadenoma and (c) Carcinoma. There are very few distinguishing features to tell them apart; the challenge faced by radiologist is considerable.

2.2.2 Breast Cancer Screening

Conventional breast cancer screening typically consists of a manual assessment of the lump (palpation). This is followed by a mammogram (X-ray) of the breast where any non palpable lumps may also be discovered. If the diagnosis still remains unclear, the assessment is followed by [33].

- *further mammography and ultrasound*
- *core biopsy and cytology*

It is worth noting several of the main goals set out by the NHS Breast Screening Programme (NHSBSP) [34]:

- *minimise the adverse effects of screening – anxiety, radiation dose*

and unnecessary investigations

- *diagnose cancers accurately*
- *make effective and efficient use of resources for the benefit of the whole population*
- *encourage the provision of effective and acceptable treatment that has minimal psychological or functional side effects*

Thus screening and assessment should ideally incorporate safe, comfortable procedures using the most accurate (but inexpensive) equipment available. Screening should be fast and efficient to increase throughput of patients. The aim is for women to feel encouraged to screen regularly and for the healthcare system to be able to afford it. This also highlights the level of performance the healthcare system would expect from any new emerging technology which claims to aid in any aspect of breast cancer treatment.

2.2.3 Cancer Diagnosis: To Biopsy or not to Biopsy?

A strong motivation for the use of elastography in breast cancer screening is the issue of biopsies. Approximately 8 out of 10 biopsies turn out to be negative for cancer [35]; encumbering often already limited healthcare resources. It has been suggested that elastograms could be used to discriminate between malignant and benign lesions based on quantitative measurements, thus greatly reducing the number of false positives [8,36]. However, quantitative methods to date have yet to produce the sensitivity and specificity required for dependable diagnosis [7-8,36-37]. Biopsies will continue to be carried out as long as there is the strong clinical desire to have a false negative rate of zero.

To understand why this is the case, consider the tissue elastic modulus (or Young's Modulus; defined in more detail in next section) for different tissue types found in the breast depicted in Figure 2.3. These measurements were made on ex-vivo tissue

samples placed under a compression plate under 2 separate conditions: under large external compression (resulting in 20% strain) and significantly less stress (5% strain). The graph reveals several interesting things about tissue with regards to elastographic imaging.

Firstly, it exposes the contrast that exists between different tissue types in terms of their stiffness. This is particularly prevalent at 20% pre-compression conditions. However, it also shows overlap predominantly between fibrous tissue and malignant lesions; fibrous tissue (like fibroadenomas) provide a serious challenge for radiologist to distinguish from cancers. These measurements support the concept that elastography can provide good qualitative, high contrast imaging in many cases but also suggests that the elastic modulus alone cannot always distinguish benign from malignant tissue. Further investigation in [38-39] reveals some cancers have a Young's modulus as high as 40 times that of fat while others are as stiff (if not softer) than fat. The main point that should be taken away from these experimental results is that no system based on quantitative measurement of elastic modulus will achieve 100% sensitivity and specificity in cancer diagnosis. Hence, a focus of this thesis is to explore the role of elastography after diagnosis.

Moreover, recovery of the elastic modulus from tissue motion is problematic as it depends on the external applied stress in addition to tissue properties. (More on the linear properties of tissue will be discussed in Section 2.3)

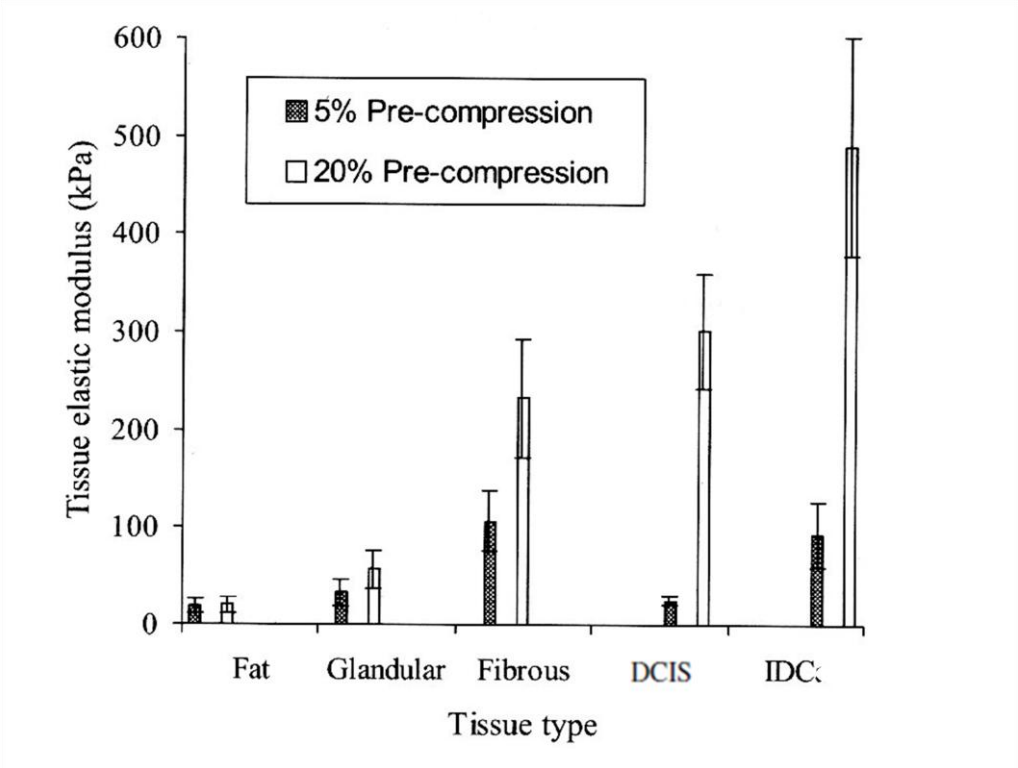


Figure 2.3- Tissue elastic modulus for different tissue types found in the breast (taken a two different compression levels). Figure adapted from [38].

2.2.4 Patient Management: BI-RADS and Breast Density

The BI-RADS (Breast Image Reporting And Data System) scale was introduced by the American College of Radiology in 1993 to help standardize the clinical assessment of breast cancers in mammography [40].

Every mammogram is assessed according to criteria such as tissue composition, the presence of calcifications and tumours and their shape and distributions. A summary of the BI-RADS scale is listed in the Table 2.2 [40].

Table 2.2 - BI-RADS Scoring System

BI-RADS Score	Description / Course of Treatment
0	Study incomplete, further imaging required
1	Negative for cancer, continue with regular screening intervals

2	Negative for cancer, but other abnormalities (e.g. cysts) were found. Continue with routine screening.
3	Small chance (~2%) of cancer, repeat mammogram in 6 months time
4	Stronger suspicion of cancer (~23-34%). A biopsy should be done
5	Very likely (~95%) to be cancer. A biopsy should be done to confirm.

It is important to note that such a well established clinical practice, which has profound effects on patient management, is based on somewhat subjective radiological findings loosely packed into 1 of 5 categories (BI-RADS 1-5). It demonstrates that a clinical tool can still be of practical use despite lacking scientific rigor.

An interesting derivative of the BI-RADS system is that of mammographic breast composition, otherwise known as (mammographic) breast density [41]. High breast density is associated with increased breast cancer morbidity [41-43], and was initially categorized into the 4 following levels: mostly fatty tissue, having scattered fibroglandular tissue, being heterogeneously dense, or as extremely dense [41]. Though the emphasis now is to better quantify breast density from image analysis of mammograms [43-44].

An initial study in [45], suggest that there is no statistically significant link between breast tissue stiffness and BI-RADS mammography features (like calcifications, size and shape). There is however a trend of average stiffness increasing with BI-RADS density. This may seem as expected, but it is crucial to remember that density and stiffness are entirely different properties of matter. Soft tissues can be dense, stiffer tissue can be made of lighter materials; it all depends on their internal structure. Elastography combined with breast density may provide complementary information;

creating a more complete picture of tumours and their interaction with surrounding tissue.

2.2.5 Therapeutic Monitoring of Cancer

Neoadjuvant therapy by definition is given prior to the main treatment option (usually surgical excision of the tumour) in order to help improve its success rate [46]. Typically this consists of chemotherapy given to reduce the size of the tumour; decreasing its chances of metastasis (or its return after surgery) and potentially reducing the need for a total mastectomy. Many factors are considered when physicians decide on a course of therapy, including but not exclusive to a patient's age, family history and overall fitness.

Many advances in cancer research has lead to chemotherapy drugs which are targeted i.e. they inhibit the specific causes of a particular cancer growth [47]. A prime example; women whose cancers are said to be HER2 positive (**h**uman **e**pidermal growth factor **r**eceptor) have an abnormally high concentration these receptors on their cells causing them to over express the growth factor hormone and consequently divide and multiply uncontrollably [48]. Unlike most standard chemotherapy drugs which inhibit mitosis across all cells in the body, hormonal therapies like *Herceptin* (generic: trastuzumab) blocks the HER2 receptor sites, preventing the naturally occurring HE hormone from taking effect [49-50]. However, given to a patient without these specific biomarkers, this drug will have little to no effect. Moreover, it is expensive; the cost for a patient on *Herceptin* is currently around £20000/year. In addition to this, women need to be tested for the right biomarkers prior to therapy which not only takes time (which can delay their treatment) but can also potentially prove erroneous if biopsies do not contain a sufficient density of cancer cells to test on or other lab related errors occur.

It is for these reasons that research in the monitoring of tumour response to chemotherapy has shifted to the forefront.

Current State of Art in Imaging Tumour Response

Two promising techniques in monitoring tumours and predicting complete pathological response are DCE-MRI and FDG-PET. The basic principle behind both methods is to measure the uptake of a particular contrast agent injected into the patient just prior to scanning. It is based on the fact that tumours create their own blood supply (a process called *neoangiogenesis*) which is often haphazard and tends to leak. The uptake and escape/leakage of contrast agent can be used to characterize this process (this is linked to a branch of science called *pharmacokenetics*)

DCE-MRI

The uptake of the contrast agent dimeglumine gadopentetate was shown to drop significantly in patients showing a response to their chemotherapy [51]. By establishing a threshold for these values, several groups were able to achieve between 83%-97% accuracy in predicting complete pathological response in studies consisting of 17-30 patients with a wide range of tumour types [52-53]. Typical scan durations lasted approximately 30 minutes, not including preparation time for administering the contrast agent, and were conducted prior to, early into and post chemotherapy. It is interesting to note that the threshold for the pharmacokenetic parameters was established retrospectively from the ROC (receiver operator curve) to achieve these success rates on a relatively small number of patients. It is also worth noting that dimeglumine gadopentetate is known to cause neurotoxicity in high doses [54-55] and, like any medication, can cause allergic reactions and mild to severe side effects.

FDG-PET

Comparable to DCE-MRI, FDG-PET methods measure the uptake of ^{18}F Flourodeoxyglugose (a radioactive isotope latched to a sugar molecule). FDG uptake was also shown to drop significantly in patient responders and remained stagnant in those showing no response to their chemotherapy. In studies consisting of 47 patients, up to 87% accuracy in predicting the pathological response was reported [56]. However, thresholds were once again established retrospectively, the setting of which needs further justification as it would have a significant impact on the sensitivity and specificity of the test [57]. Typical scan durations were on the order of 10 minutes. In addition to having an injection of a radioactive substance (necessary for all PET imaging), patients could also be asked to fast up to 24 hours prior to the scan to help establish a consistent baseline for blood sugar levels [58-59].

Both these imaging methods provide in depth views of tumour metabolism and are invaluable research tools. Initial reported results would suggest that they can detect chemotherapy response at a very early stage. What still needs to be established is how to formulate a robust threshold for the pharmacokenitc parameters that would work well in a much larger, general population. Moreover, these scans are somewhat invasive for patients (though perhaps no more invasive and discomforting as the chemotherapy they are already taking). Additionally, MRI and PET scanners are expensive pieces of equipment (on the order of £1 million) and given the toxicity of the contrast agents used, frequent repetitive scanning would pose a prohibitive health risk. Nonetheless, the reported figures from these studies highly encourage the continued use of these techniques for cancer monitoring.

Thus, there is strong incentive to develop alternative chemotherapy monitoring tools. This thesis (Chapter 7 in particular) concerns itself with the role of ultrasound elastography and how can it be applied to this end. The basic motivation behind the use of elastography is as follows.

The stromal environment of a tumour contains an abundant variety of cells including endothelial, fat, fibroblasts, inflammatory and immune cells in addition to a host of molecules found in the extra cellular matrix (ECM). In Figure 2.4, the process of tumour formation and stromal reaction is depicted. It has been identified that significant interaction takes place between tumour and stroma through all stages of tumour growth; this complex relationship is an ongoing topic of research [60-64].

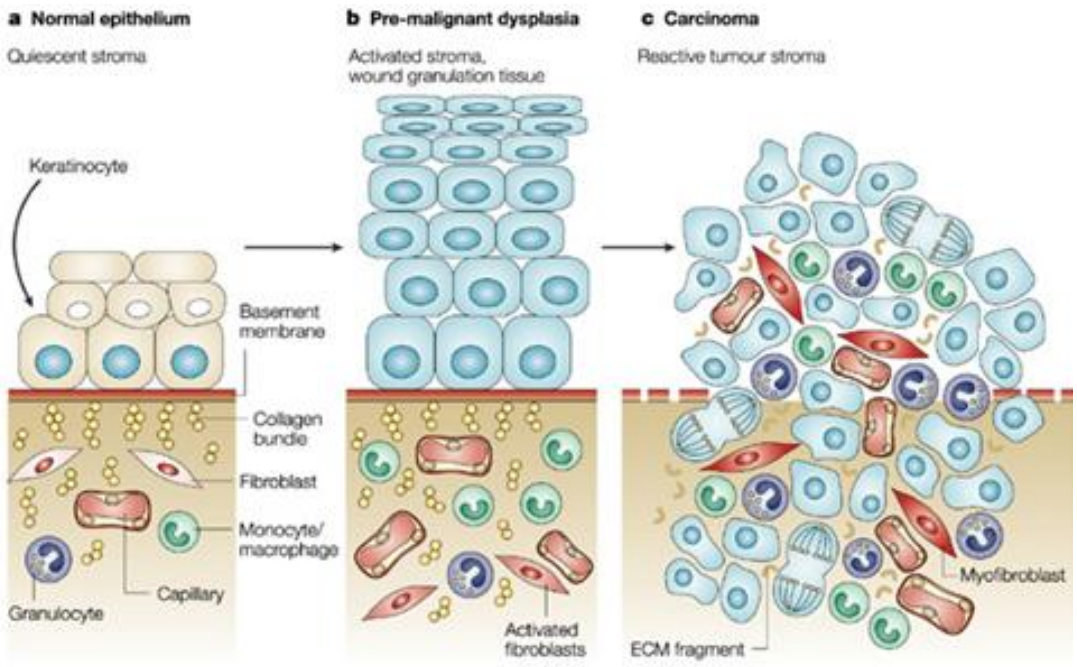


Figure 2.4-Tumour stages and stromal activation [63]

The interest from an elastography perspective is the effect that stromal and tumour reactions have on their mechanical properties. Fibrotic changes occur during tumour

growth and are also a quintessential process of healing. Indeed, fibrosis is a common after effect to chemotherapy in many forms of cancer [64-66]. Figure 2.4 shows before and after pathology slides from a patient having underwent chemotherapy and been successfully treated. What predominantly remains are necrotic cancer cells along with fibroblasts and their associated connective tissue.

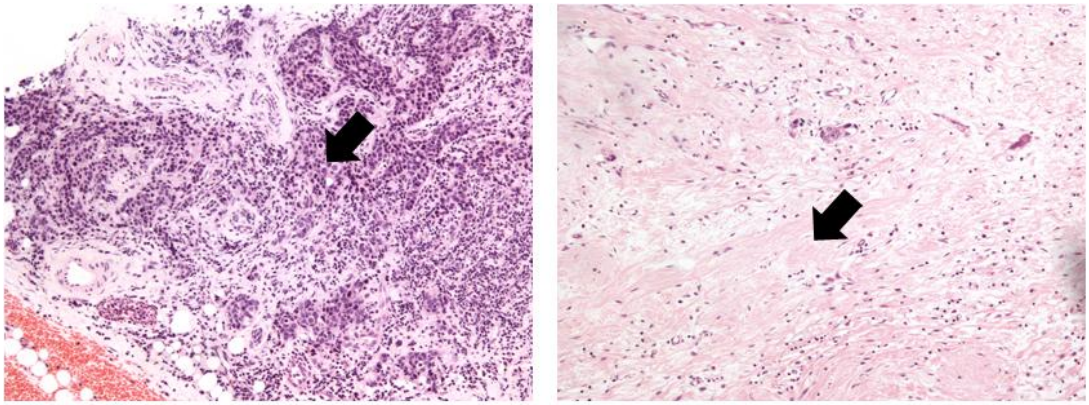


Figure 2.5- (a) Before Treatment: Tumour cells are everywhere, their nuclei are coloured purple. (b) After treatment: Fibrosis (pink) dominates what is left of the necrotic tumour cells. These samples were taken from Patient #3 of a neoadjuvant chemotherapy study presented in Chapter 7.

Fibrosis, necrosis and inflammation may all contribute to a measurable response in elastography/strain imaging [11-12,67-68]. It is these changes to the tissue composition and ECM that we attempt to measure over a course of a patient's treatment to assess their response to chemo/hormonal therapy.

It is a suggestion of this thesis that ultrasound elastography can provide a safer, cheaper, less invasive option to DCE-MRI and FDG-PET, which may perhaps be as effective for all intents and purposes given that the primary concern in clinic is to ascertain whether a chemo regimen should be continued or a new drug tried. Ultrasound has the advantage

of being able to scan a patient as frequently as necessary without risk of ionising radiation or toxicity. At present, there are no reports of ultrasound elastography performing in the same capacity or with the same accuracy as DCE-MRI and FDG-PET, however extensive studies have yet to be performed to establish its potential role. At the very least, it would be expected to provide useful complementary information to either DCE-MRI and/or FDG-PET, thereby improving the overall accuracy of the combined tests.

2.3 Tissue Modelling and Imaging for Elastography

2.3.1 Strain and the Elastic Model

Physics of Strain and Biomechanics

When a medium is compressed or stretched by an external force the resulting deformation creates internal stresses within the material. The measure of how this deformation varies locally is called *strain*. In general, stresses will not only be the result of the final load and deformation but of the history and rate at which it was applied. Moreover, the medium may not return to its original shape after the load is removed, a phenomenon called hysteresis [69]. The following describes the main concepts behind stress and strain and presents the simplification steps taken to derive the strain equations used in elastography, more specifically quasi-static elastography. A good reference for all of the information presented in this section can be found in [70].

Stress and Strain

Consider an element of tissue as depicted in Figure 2.6 in which stress, $\boldsymbol{\sigma}$ and strain, $\boldsymbol{\varepsilon}$ are also defined.

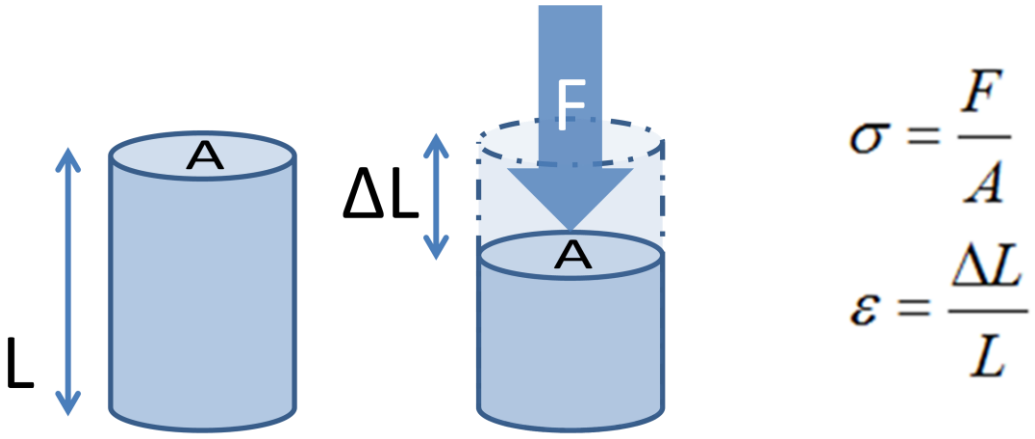


Figure 2.6- Stress and Strain and their relationship to force F, applied over area A. Stress is a measure of force per unit area (N/m^2 or Pascals) and strain measures the relative displacement and is unit-less.

The distribution of internal stresses and strains within any material can be quite complex. Stress at a point can be described by taking an infinitesimal element over which forces can be taken as uniform (Figure 2.7).

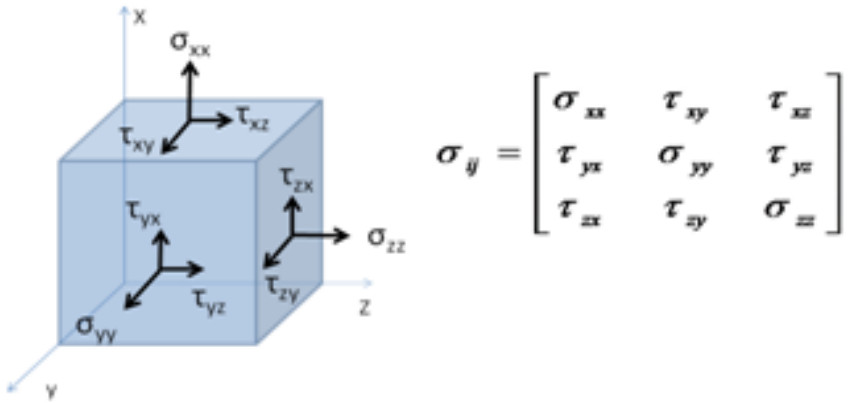


Figure 2.7- Internal shear and axial stresses on an infinitesimal cube; the general model for stress/strain theory. Note a total of 9 stresses (3 planes x 3 directions) are needed to completely describe the system (the remaining 3 faces of the cube have equal and opposite stresses associated with them). Also, often τ_{ij} is written simply as σ_{ij}.

Strain ε_{kl}, can be measured from observed displacements such that a displacement field $\boldsymbol{d}(x,y,z)$ is related to strain as follows

$$\boldsymbol{d}(x,y,z) = \begin{pmatrix} u(x,y,z) \\ v(x,y,z) \\ w(x,y,z) \end{pmatrix}, \quad \nabla \boldsymbol{d} = \begin{bmatrix} u_x & u_y & u_z \\ v_x & v_y & v_z \\ w_x & w_y & w_z \end{bmatrix}, \quad \nabla \rightarrow Jacobian\ Operator$$

$$\varepsilon_{kl} = \frac{\nabla \boldsymbol{d} + \nabla \boldsymbol{d}^T}{2} = \begin{bmatrix} \varepsilon_{xx} & \varepsilon_{xy} & \varepsilon_{xz} \\ \varepsilon_{yx} & \varepsilon_{yy} & \varepsilon_{yz} \\ \varepsilon_{zx} & \varepsilon_{zy} & \varepsilon_{zz} \end{bmatrix}, \tag{2.1}$$

The components of displacement, *u*,*v* and *w* are independant functions of poisition.

Generalized Hooke's Law

Elasticity is based on the assumption that the stress is solely a function of the deformation (strain) and that the body will return to its original shape when the load is removed. If it is further assumed that the stress-strain relationship is *linear*, the relationship can be expressed by the generalized Hooke's Law.

$$\sigma_{ij} = C_{ijkl}\varepsilon_{kl} \tag{2.2}$$

C is a matrix of elasticity coefficients, *j*,*l* indicate direction of force/strain and *i*,*k* denote the plane on which it is acting. To account for 3 directions of deformation in 3 planes, C_{ijkl} is a 9x9 matrix with 81 elastic constants i.e. elasticity at a point requires 81 values to describe it completely.

It is important to understand what effects the linearity assumption will have on elastographic imaging; it is a particular issue when the external loading stress is applied freehand and the amount of deformation is not easily controlled. Several groups [38,71-72], have investigated non-linearity in tissues.

Going back to Figure 2.3, it was demonstrated that fat (a predominant tissue type typically found in breasts) has unvarying stiffness behaviour over a large range of externally induced strain. Conversely, cancers show increased stiffness at greater strain, sometimes referred to as *strain hardening*. These results are further emphasized in Figure 2.8.

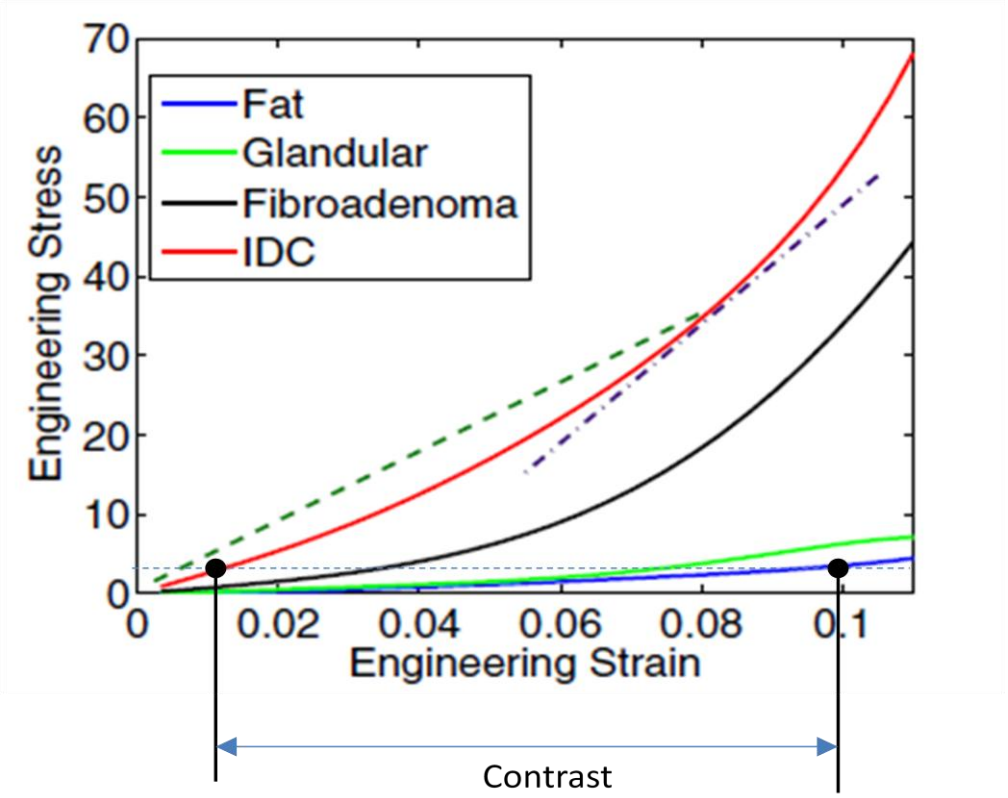


Figure 2.8- Stress vs Strain curves for different tissue types found in the breast. Contrast in an elastogram is associated with the difference between strain values at a given applied load (as depicted), Figure was adapted from [71-72]

Contrast in an elastogram is associated with the difference between strain values at a given applied load (as depicted). Because of non-linear effects, this may actually increase at higher stresses providing improved image contrast and better qualitative imaging as a consequence.

Quantitatively, this effect is disastrous on the dependable recovery of a consistent elastic modulus. However, non-linear affects for carcinomas have been found to be

marginal even at 10% strain. Possibly as high as 15% strain is required to observe non-linearity in lesions [71]; well within the realm of freehand quasi-static imaging.

Poisson's Ratio

Compressibility measures how well a material can maintain its initial volume when an external force is applied to it. For example, rubber is often regarded as virtually incompressible. Consequently, stretching a rubber band along its length will cause it to narrow in width in order to maintain its volume. *Poisson's Ratio* denoted by υ, provides a measure for this phenomenon (Figure 2.9)

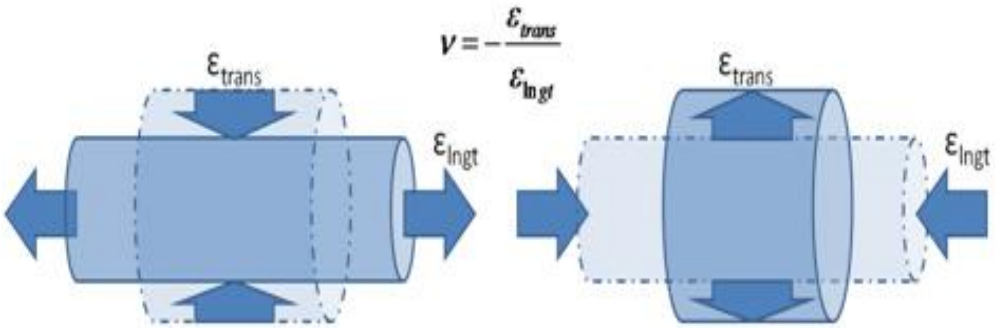


Figure 2.9- The Poisson Effect with positive *ν* for tensile (left) and compression (right) strains. Strain in one direction, ε_{lngt}, can induce strain in the transverse direction, ε_{trans}. The ratio of these two strains is Poisson's Ratio and is a characteristic feature of a particular material. For isotropic materials, ν is a scalar constant. For general anisotropic materials, ν is a tensor.

Thus, total measured strain in any particular direction will be the superposition of strain due to stress in that direction plus that induced by the Poisson Effect from transverse stresses (*see Eq(2.4) below*). For most materials, Poisson's Ratio ranges from 0 to 0.5 where 0.5 entails complete incompressibility. Strictly speaking no material is completely incompressible and Poisson's ratio is normally taken at around 0.495 for soft

tissues [73-78]. The incompressibility of tissue can have a profound effect on elastography as demonstrated later in Figure 2.10.

Modelling for Elastography

The model used in elastography uses 3 main assumptions which simplify C_{ijkl} considerably: the system is in *static (or quasi static) equilibrium*, the material is *isotropic* and the stress induced is *uniaxial*.

Static equilibrium implies a balance of forces which result in $\sigma_{ij}=\sigma_{ji}$ and $\varepsilon_{ij}=\varepsilon_{ji}$. For *isotropic* materials, a common elasticity coefficient E (known as Young's Modulus) can be factored out of C_{ijkl}. The net result is a relationship between stress and strain described entirely by E and υ.

$$\begin{Bmatrix} \varepsilon_{xx} \\ \varepsilon_{yy} \\ \varepsilon_{zz} \\ \varepsilon_{yz} \\ \varepsilon_{zy} \\ \varepsilon_{xy} \end{Bmatrix} = \frac{1}{E} \begin{bmatrix} 1 & -\nu & -\nu & 0 & 0 & 0 \\ -\nu & 1 & -\nu & 0 & 0 & 0 \\ -\nu & -\nu & 1 & 0 & 0 & 0 \\ 0 & 0 & 0 & (1+\nu) & 0 & 0 \\ 0 & 0 & 0 & 0 & (1+\nu) & 0 \\ 0 & 0 & 0 & 0 & 0 & (1+\nu) \end{bmatrix} \begin{Bmatrix} \sigma_{xx} \\ \sigma_{yy} \\ \sigma_{zz} \\ \sigma_{yz} \\ \sigma_{zy} \\ \sigma_{xy} \end{Bmatrix} \tag{2.3}$$

Note: the stress and strain matrices have been rearranged into column vector form, and the inverse relationship is being shown. Under the same assumptions, Bulk Modulus K, and Shear Modulus G can be inferred as well:

$$K = \frac{E}{3(1-2\upsilon)}, \qquad G = \frac{E}{2(1+\upsilon)}$$

Two useful equations taken from *Eq(2.3)* describe stress and strain in the z-direction as

$$\epsilon_{zz} = \frac{1}{E}\left[\sigma_{zz} - \nu(\sigma_{xx} + \sigma_{yy})\right] \tag{2.4}$$

$$\sigma_{zz} = \frac{E}{(1+\nu)(1-2\nu)}\left[\nu\epsilon_{xx} + \nu\epsilon_{yy} + (1-\nu)\epsilon_{zz}\right] \tag{2.5}$$

If it is now assumed that a *uniaxial* force in the z-direction is applied, *Eq(2.3)* and *Eq(2.4)* reduce to

$$\sigma_{zz} = E\epsilon_{zz} \tag{2.6}$$

This equation forms the foundation for quasi-static elastography which is the main work in Chapter 3. If it is assumed the force applied is equally distributed through the medium, σ_{zz} (though unknown) can be treated as constant and *E* can be inferred from the measured strain, ϵ_{zz}. This is the basis for *Strain Imaging (often used synonymously with elastography). Eq(2.6)* is only true for an unconstrained system i.e. σ_{xx} and σ_{yy} can be set to zero because the material is free to expand according to the Poisson Effect. However, the heterogeneous characteristic of human tissues results in boundary conditions between neighbouring tissues which affect the spread of the applied force as well as the strain distribution. Assuming the tissue is constrained to move in the transverse direction, i.e. ε_{xx} and $\varepsilon_{yy} = 0$, *Eq(2.5)* gives

$$\frac{\sigma_{zz}}{\epsilon_{zz}} = E_{app} = \frac{E\ (1-\nu)}{(1+\nu)(1-2\nu)} \tag{2.7}$$

If one were to try and infer elasticity directly from strain in this case, the apparent Young's Modulus $\boldsymbol{E_{app}}$ (also known as the constrained modulus) would be subject to the compressibility of the material and related to the actual Young's modulus as per Figure 2.10.

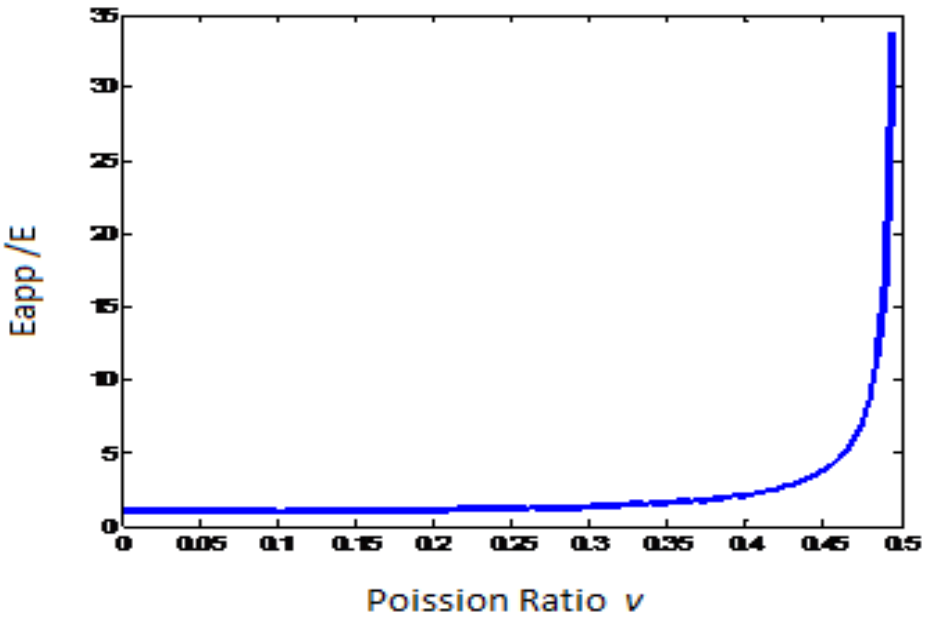


Figure 2.10- Plot of multiplicative factor affecting the ratio of E/E_{app} as a function of Poisson Ratio

Thus with an assumption of near incompressibility, accurate estimate of Young's Modulus for soft tissues using *Eq(2.6)* is only valid if the tissue is unconstrained. Alternatively, *E* can be estimated regardless of constraint conditions provided accurate measurements of transverse strains ε_{xx} and ε_{yy} can be obtained; in this case *Eq(2.5)* can be applied.

With these constraints in mind, it becomes clear that quantitative measurement of tissue mechanical properties has significant sources of error. In practice, strain images are used as pseudo-stiffness measures and provide qualitative data for clinicians to interpret; finding the correct interpretation is the challenge faced by researchers.

2.3.2 Ultrasound Imaging

The basics of ultrasound B-mode (***B***rightness Mode) image generation are summarized in Figure 2.11. The backscattered signal from a transmitted pulse undergoes Time Gain Compensation (TGC) which corrects for depth dependant attenuation. At this stage,

note that the raw channel data bears little resemblance to any anatomical features. The next step is to filter this image spatially, through a process known as *beamforming* or *dynamic receive focusing*. The most common form of beamforming (also the simplest) is known as the Delay and Sum (DAS) method [79-81]. Beamforming is heavily dependent on the physical configuration of the probe i.e. the number and spacing of the transducer's piezo-electric elements, as well as the processing power of the machine.

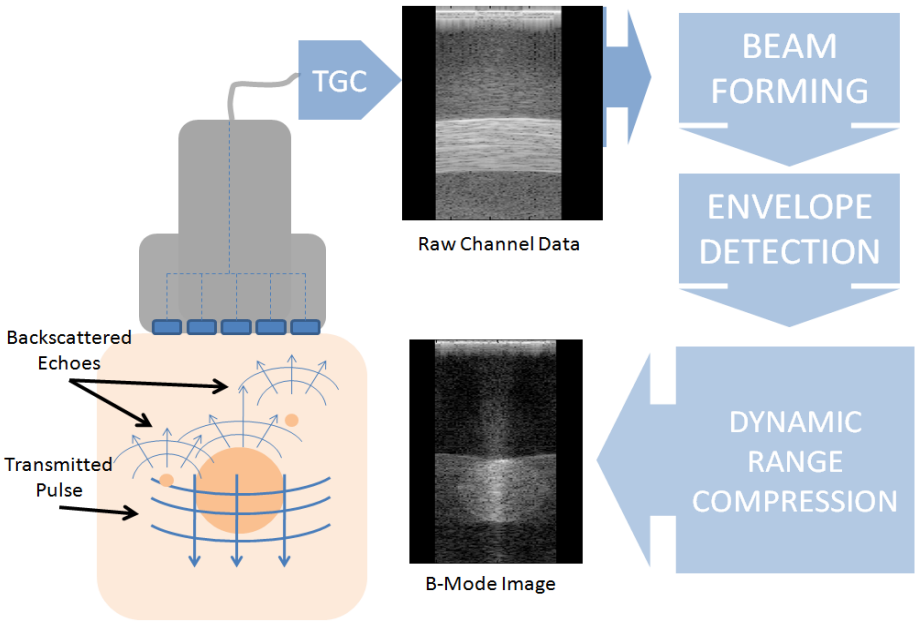


Figure 2.11- B-mode Image Generation

IQ Demodulation and Envelope Detection

After the beamforming stage, each axial line (A-line) in the image can be represented by a radio frequency (RF) signal, *x(t)*, which is then demodulated to remove its carrier frequency component using envelope detection or (in the case of the US machine used in this project) by producing an IQ demodulated signal.

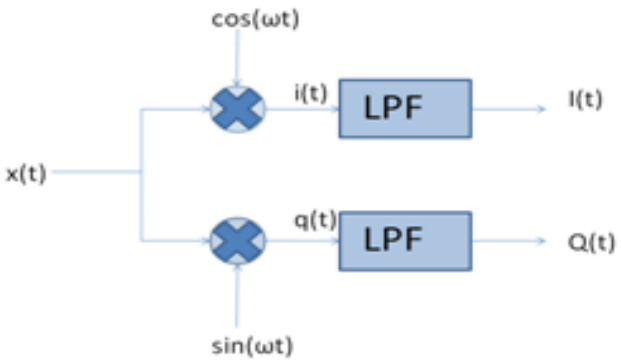


Figure 2.12- IQ Demodulation-Signal Block Diagram

IQ stands for the **i**n-phase (I) and **q**uadrature (Q) decomposition of a signal. Figure 2.12 depicts the process: Let *x(t)* represent the received signal (after beamforming) which can be represented by a generalized frequency and amplitude modulated signal:

$$x(t) = A(t)\cos(\omega t + \phi(t)), \quad \omega = 2\pi f_c \qquad (2.8)a$$

Here, f_c equals the probe centre frequency. Tracing the signal's path through Figure 2.12 and using trigonometric double angle formulas we arrive at

$$i(t) = \frac{A(t)}{2}\left(\cos(2\omega t + \phi(t)) + \cos(\phi(t))\right), \qquad (2.8)b$$

$$q(t) = \frac{A(t)}{2}\left(\sin(2\omega t + \phi(t)) - \sin(\phi(t))\right) \qquad (2.8)c$$

After low pass filtering (LPF) to remove the 2ω frequency component we have

$$I(t) = \frac{A(t)}{2}\cos(\phi(t)), \quad Q(t) = \frac{-A(t)}{2}\sin(\phi(t)) \qquad (2.8)d, e$$

Both I(t) and Q(t) are baseband signal that can be downsampled and processed at significantly lower data rates. Interestingly, if we create a complex signal *S(t)* such that *S(t)=I(t)+iQ(t)*. We find that

$$\|S(t)\| = \frac{|A(t)|}{2}, \quad \arg\{S(t)\} = -\phi(t) \qquad (2.8)f, g$$

Thus the *envelope* and *phase* information in the original signal *x(t)* is preserved in the IQ demodulated signal. An alternative approach to demodulation is to directly take the Hilbert Transform of the signal *x(t)*, denoted by $\hat{x}(t)$, which has the effect of inducing a 90 degree phase shift in all its components i.e. it transforms cosines into sines. The complex analytic signal $x_a(t)$ can then be formed by

$$x_a(t) = x(t) + i\,\hat{x}(t) = A(t)e^{i(\omega t + \phi(t))} \qquad (2.9)$$

By multiplying $x_a(t)$ by $e^{-i\omega t}$, we once again arrive at our IQ signal. In this thesis, all signals are acquired and processed in IQ demodulated form.

The final B-mode image is produced after logarithmic compression to tackle the large dynamic range of the received signal. Methods such as time and frequency compounding are often used to produce images with different speckle characteristics, specifically suited to a particular imaging application. However, the raw IQ signals used in this thesis work were extracted at a stage prior to these machine/manufacturer dependant operations thus mitigating their unwanted effects.

The Linear System Model

All of the above processes would suggest that the final image produced is dependent on the specific ultrasound machine. Indeed, the frequency response of the piezo-electric transducers, transducer aperture, beamforming and transmitted pulse waveform can all be lumped into the point spread function (PSF) of the imaging system. In simplest terms, the PSF describes the resulting image from a single point scatterer due to the

blurring effects of the factors mentioned above. With this model in mind and the assumption of a linear system, the backscattered signal can be modelled as:

$$x(t) = PSF(t) * h(t) \qquad (2.10)$$

where * denotes convolution and *h(t)* is the distribution of scatterer strengths. Figure 2.13 shows their relationship in both time and frequency domains.

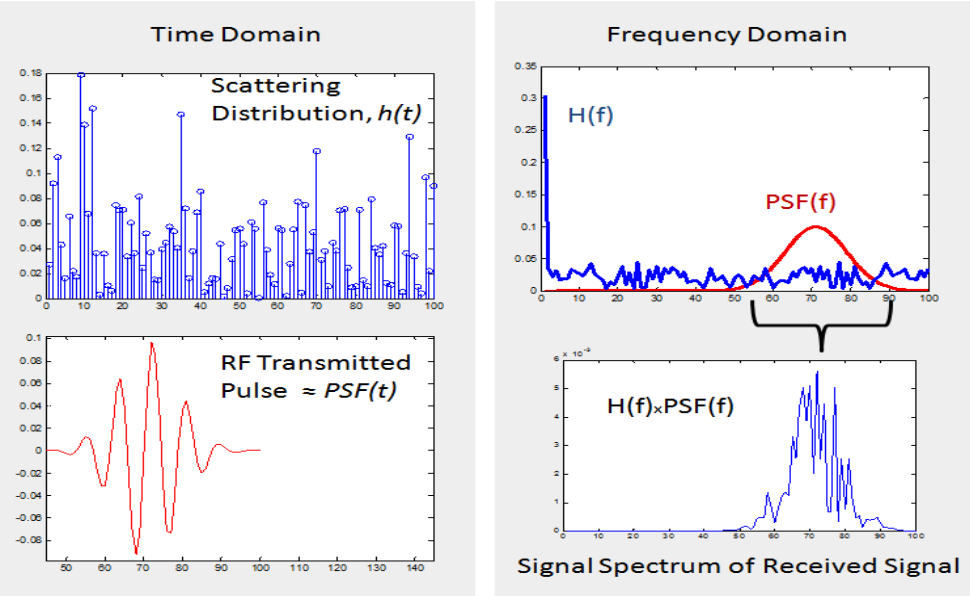


Figure 2.13- Time and Frequency Domain depictions of the scatterer distribution and PSF

Speckle

Speckle is commonly found in systems which make use of coherent sources of sound or light (i.e. an ultrasound pulse or laser beam) [82-83]. It is caused by the diffuse reflections or scattering of the sound/light, generating an interference pattern which produces so called speckle in the final image. Speckle is often modelled as Rayleigh distributed noise which generally obscures anatomical features in ultrasound images, however other distributions have been used to model its statistics [84]. However, speckle is not totally random. It is in fact an interference pattern caused by the

underlying layers of tissue and is characteristic of that region, thus speckle may be regarded as deterministic. In fact, it can be shown that any particular image can be generated from an infinite set of possible scattering distributions, with only one reflecting the true underlying process [82].

Consequently, correlative speckle tracking can be used in ultrasound imaging to follow tissue movement as in the heart or other muscles [85]. The unique PSF of a particular imaging system is of little consequence to elastography since it relies on *comparing* images taken from the same machine and aims to measure tissue characteristics, not the acoustical properties such as attenuation and dispersion which can vary from one ultrasound machine to another.

2.4 Related Work in Elastography

2.4.1 ARFI and Shear Wave Imaging

A discussion of elastography would not be complete without mention of the latest technology to emerge from ultrasound, *acoustic radiation force impulse* (ARFI) imaging. A great deal of literature can be found on the subject and excellent reviews can be found in [39,86-87].

ARFI imaging has been developed into many forms but can roughly be categorized into quantitative and non-quantitative imaging (though both in fact can be derived from a given data set). These can be further segregated into shear wave (steady state) and pulsed (transient) techniques.

All of the above techniques rely on two things:

1. Using the ultrasound probe itself to generate a series of pulses to 'push' tissue so as to create a transient or steady state transverse wave (also called a shear wave)

through tissue. This can be achieved with most standard ultrasound probes subject to a software overhaul of its firing sequence. (see Figure 2.14)

2. Having a very high (>1000-10000 Hz) diagnostic ultrasound frame rate required to capture the propagation of the wave. For real-time imaging, this requires processing power and memory not currently found in all typical US equipment, i.e. specialized equipment is needed.

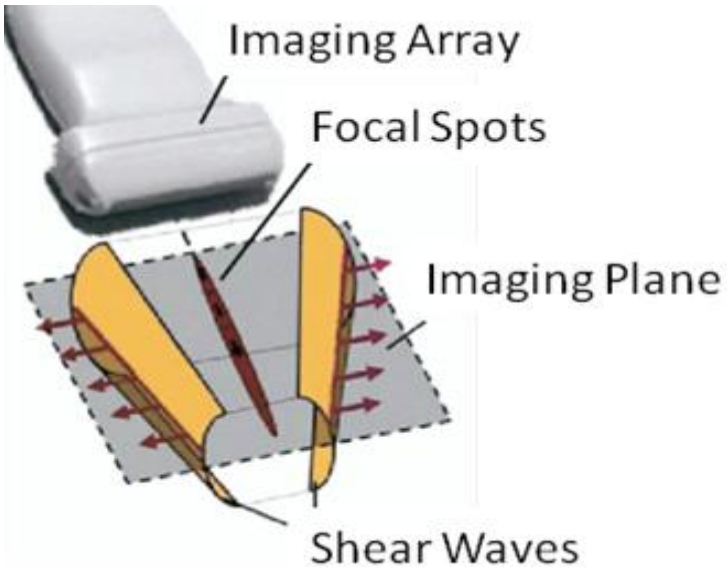


Figure 2.14- Adapted from [88], depiction of shear wave generation. A series of compression pulses are focused along strategic points axially. The resulting 'push' on the tissue creates a transverse (shear) wave that propagates near laterally.

This field of research is laden with acronyms that are not always used consistently. It is more accurate to say that ARFI encompasses the entirety of methods, however it is sometimes associated with just the sub-category of qualitative transient imaging [86]. Shear wave elasticity imaging (SWEI) includes Super Sonic Imaging (SSI), and SMURF [89-90] (Shear Modulus Imaging by Spatially Modulated Ultrasound Radiation Force) which often employ TOF (time of flight) methods that are associated with quantitative imaging and recovery of the elastic modulus.

Another interesting variant of this field of research is *vibroacoustography* and *harmonic motion imaging* (HMI). These involve focusing a pair of waves of different frequencies at a specific spatial location to produce a tissue response at the beat frequency which can be monitored by hydrophone (vibroacoustography) or from ultrasound speckle tracking (HMI) where amplitude and phase can then be used to assess tissue characteristics and give relative stiffness information. The waves can then be effectively rasterized across an imaging plane to interrogate any point.

Qualitative Imaging

Qualitative properties at any particular spatial point in the tissue under examination can be derived from measuring the maximum displacement incurred from the pulse, (or peak to peak displacement in the case of steady state shear waves), and/or the *time to recovery* after the max displacement (which is associated with viscoelasticity). Displacement estimation is typically measured through correlative block matching methods (which also form the basis for most quasi-static methods discussed later in this chapter). Strain, along with max displacement is inversely related to tissue stiffness; another consistency with the quasi-statics elastic model and assumptions.

Quantitative Imaging

The true unique selling point of ARFI is its claim to provide accurate quantitative reconstruction of tissue stiffness. Recovery of the shear modulus, μ, is achieved through measuring the speed of the transient pulse/wave, c_T.

$$c_T = \sqrt{\frac{\mu}{\rho}} \qquad (2.11)$$

The density, ρ is taken as constant throughout the tissue. Wave speed can be measured in several ways. The pulse arrival times measured at two or more known locations (usually in a line normal to the wave front) can be used to estimate wave speed. Alternatively, the arrival times of two (or more) wave fronts whose sources are spatially offset from each other can be measured at a single point to the same effect (this forms the basis for SMURF). In the case of shear waves, TOF methods can also be used to recover the spatial frequency, *(1/λ)* (*Eq(2.12)*). The temporal wave frequency, *f*, of the shear wave is known as it is determined by the *pulse repetition frequency* (PRF) of the prescribed 'push' pulse sequence.

$$\mu = \rho \cdot f^2 \cdot \lambda^2 \qquad (2.12)$$

ARFI Assumptions

There are several significant assumptions being made in ARFI. First and most importantly, the assumption that all tissue has the same density. Breast tissue such as fat and connective tissue have been found to have densities varying from 0.92 g/ml (fat) to 1.3 g/ml (collagen) [91-93]; a 36% difference. Results from [93] and the afore mentioned BI-RADS study in [45] would suggest a more complex relationship between stiffness, wave speed and density underlies the true nature of tissue.

As with quasi-static elastography, ARFI imaging also assumes a linear, isotropic tissue model. However, visco-elastic effects (that static methods avoid) can affect wave speed estimation in tissues that exhibit significant viscosity resulting in an underestimate of tissue stiffness [94].

TOF methods rely upon assumed wave front shape and direction, both of which will be affected by attenuation, reflections and refraction which are generally neglected. In

effect, ARFI assumes a homogeneous model of soft tissue; a model inconsistent with other practices like the BI-RADS density scale and the fact that many complex boundaries and structures are prevalent in real clinical data [10,94-95].

It is also generally assumed that the generated 'push' pulses can be focused with high precision at depth, irrespective of the tissue above that point and the afore mentioned effects. Thus, focal points may in reality deviate from their intended locations. Moreover, ARFI pulses are limited to intensities low enough to avoid excessive tissue heating and cavitation. Consequently, only small displacements can be produced resulting in generally noisy displacement data.

Lastly, shear wave speed is also subject to dispersion in soft tissue and exhibits a temperature dependence [96-98]. On the one hand, from a strictly scientific view point, this can provide even greater insight into tissue behaviour. Conversely, from a practical and clinical view point, selecting a set of imaging parameters to suit any particular patient could prove difficult to manage and certainly detrimental to any reliable and consistent quantitative measurement of stiffness.

Clinical results [39,88,99-100] so far have not distinguished ARFI from similar studies using standard freehand quasi-static ultrasound with both sensitivity and specificity figures around the 85-90% mark. This is expected given both methods effectively measure the same thing but in different ways. Quasi-static methods have an advantage from a research perspective because they can be implemented easily on existing ultrasound systems whereas ARFI requires specialized commercial equipment which many hospitals have yet to invest in.

Unfortunately, all elastography methods suffer from the fact that they are hard to validate; synthetic phantoms provide a ground truth but are often too simplistic with respects to real clinical data. Moreover, there is no ground truth available for clinical data as surgical excision obliterates the in-vivo behaviour observed in a scan. Consequently, establishing elastography and gaining the confidence of clinicians is a slow, ongoing process.

However, despite the limitations and complexities of ARFI perhaps its greatest advantage is its lack of inter-operator dependency (though there are many parameters to set up). Moreover, ARFI has been used in the liver, blood vessels and prostate (areas where direct freehand mechanical manipulation of the tissue would be problematic) in addition to monitoring HIFU therapy [39,139-143], .

2.4.2 MR Elastography

MR elastography is also an emerging medical imaging technique which bears a great resemblance to shear wave imaging described in the ARFI section. In the case of MR, an external vibrator provides the source of shear waves at a given frequency. The propagation of shear waves through tissue is monitored through a modified phase contrast gradient echo sequence and the shear modulus is recovered from *Eq(2.12)*.

Experiments carried out in [96] were able to establish a 2.3 to 6.8 ratio of tumour stiffness to adjacent tissue in breast tissue using a scanning protocol taking up to 40 seconds for each acquisition, suggesting its possible role in breast cancer care. MR elastography has also found a niche in detecting liver cancer and fibrosis [97]. As with ARFI, MR elastography has all the same issues with dispersion and temperature dependency and assumptions about tissue density [98].

In summary, ARFI and MR elastography are undoubtedly sophisticated state of the art methods that can provide promising results. Moreover, they are capable of imaging tissues and organs that would prove impractical if not impossible for standard freehand quasi-static ultrasound elastography. But as mentioned earlier, their focus has been on diagnosis based on quantitative measurement of tissue stiffness which has been shown to be a fundamentally flawed endeavour. These are complex systems with many parameters to set, many significant assumptions to make, and lack availability compared to standard ultrasound elastography. It is remarkable and most pertinent to underscore that overall, in the case of breast cancers, they do not appreciably outperform quasi-static methods; the focus of this thesis work.

2.4.3 Quasi-Static Methods for Displacement and Strain Estimation

It is clear from the tissue model presented in Section 2.3 that elastography is essentially a 1D measurement of tissue deformation due to a 1D axial force. We know from the Poisson effect, however, that tissue motion will contain lateral and elevational components (even from a purely axial force). Thus the emergence of 2D and 3D algorithms; their role has been to provide an extension of the 1D case, by compensating for non axial motion and ensuring a more accurate comparison of signal content between images. Basically, they aim to improve the quality of the 1D measurement.

Regardless of their dimensionality, elastography algorithms can be broken down into two basic steps: Displacement Estimation (or motion compensation) followed by a calculation of strain. It is in the former that most variation is found amongst the many proposed methods to date. Ultrasound image sequences used in elastographic analysis can be noisy. Tissue motion can move out of the imaging plane of a 2D probe, meaning

that information is lost and noise is introduced. The goal of most researchers has been to find the right balance or trade-off between methods which are robust, computationally efficient, accurate and precise.

Displacement Estimation

The most fundamental technique for displacement estimation is that of block matching. In Figure 2.15, a windowed portion of signal in a post-compression image is matched to a similar portion in the pre-compression image according to some similarity metric. The most commonly used metrics are sum of absolute difference (SAD), sum of squared difference (SSD) and normalized cross correlation (NCC); all of which have been shown to perform similarly in ultrasound signals. [101-102].

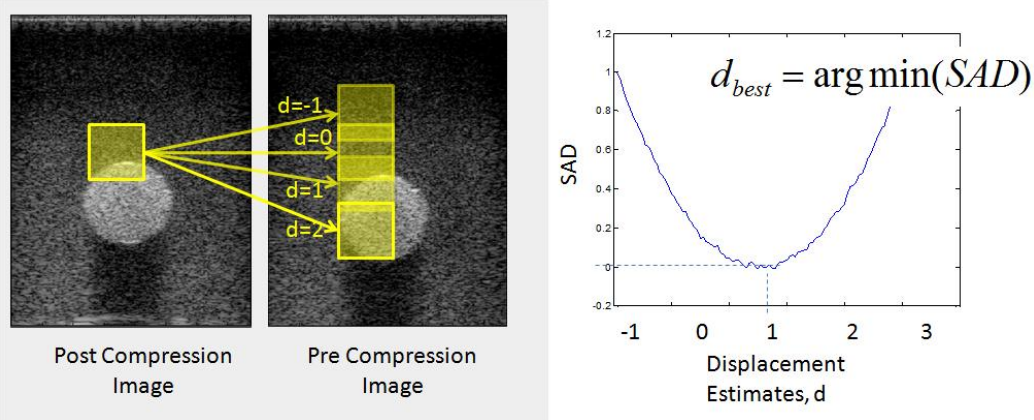


Figure 2.15- Illustration of Block Matching Algorithm and the resulting similarity metric scores from the search. In the case of SAD, the *minimum* score corresponds to the 'best' estimate for *d*

Window size and overlap play an important role in block matching precision, accuracy and the resolution of the output displacement field (these concepts will be explored further in Chapter 3).

A number of improvements to the basic algorithm have been proposed. In [103], a coarse to fine approach was used to help narrow the search range and speed up

computation where the monotonic nature of the displacement field is exploited. Rather than perform an exhaustive search for each window, initial displacement estimates are used to seed the starting point of subsequent searches. Unfortunately, there is potential for any single estimate error to propagate, leading to so called 'drop-out' errors. The authors attempted to solve this problem by introducing a quantitative measure of confidence or quality in the estimate (an important concept which will be discussed in Chapter 4), making sure that only estimates with a high probability of accuracy were used to guide the algorithm searches.

Precision in the displacement estimation is important in many elastography methods for subsequent analysis of strain. The most straightforward approach to obtain a high resolution output is to simply up-sample and interpolate the ultrasound signal in the axial dimension and perform any variant of block matching. Alternatively, in [104] cubic splines were fit to the displacement field providing a set of analytic functions which could then be differentiated as in *Eq(2.1)* to obtain a continuously smooth function for strain.

Probably the most popular technique which is used in commercial systems such as Siemens and Hitachi [105], exploit the angular phase information present in the ultrasound RF signal to provide fast sub sample interpolation of displacement estimates. Variations of these methods can be found in [106-107]. The model assumes pre and post compression signals are related by a simple time delay. The RF signals can be represented as

$$x_{pre}(t) = A(t)e^{-j(2\pi f_o t+\varphi)} \qquad (2.13a)$$

$$x_{post}(t) = A(t-\tau)e^{-j(2\pi f_o (t-\tau)+\varphi)} \qquad (2.13b)$$

where f_o is the pulse centre frequency and *A(t)* is the signal envelope. The IQ signals *s(t)* are then obtained through demodulation.

$$s_{pre}(t) = A(t)e^{-j(\varphi)} \qquad (2.14a)$$

$$s_{post}(t) = A(t-\tau)e^{-j(\varphi-2\pi f_o\tau)} \qquad (2.14b)$$

The goal is thus to measure the time shift τ. Because τ will vary spatially, the pre-compression signal is windowed and the corresponding window W in the post-compression signal is found through complex cross correlation

$$R(v) = \int_{t-\frac{W}{2}}^{t+\frac{W}{2}} s_{pre}(t) \cdot s^*_{post}(t+v)dt$$

$$= e^{-j2\pi f_o\tau} \int_{t-W/2}^{t+W/2} A(t) \cdot A^*(t-\tau+v)dt \qquad (2.15)$$

Note the summation term is the autocorrelation function of the signal envelope. Thus $|R(v)|$ will have a maximum when $v = \tau$. In practice these signals are digitized thus v can only approach τ to within a sample length i.e. $v \rightarrow v' = n/f_s$, where n is the number of samples separating the windows in the digital signal sampled at f_s. The unwrapped phase angle at this point can be used to refine the estimate for τ by detecting its subsample portion, $\Delta\tau$

$$\theta_{R(v')} = tan^{-1}\left(\frac{Im\{R(v')\}}{Real\{R(v')\}}\right) = -2\pi f_o\Delta\tau, \qquad -\frac{\pi}{2} < \theta_{R(v')} < \frac{\pi}{2} \qquad (2.16)$$

$$\Delta\tau = -\frac{\theta_{R(v')}}{2\pi f_o}$$

Assuming a constant speed of sound c the final displacement estimate can be calculated as

$$d = \frac{c}{2}\tau = \frac{c}{2}(v' + \Delta\tau) = \frac{c}{2}\left(\frac{n}{f_s} - \frac{\theta_{R(v')}}{2\pi f_o}\right) \qquad (2.17)$$

One limitation of this method is that its model hold only for small strains (<~1%), thus only small displacements allowed and consequently data will be noisy.

Other Methods for Motion Tracking

Another innovative scheme for displacement estimation uses a dynamic programming method [6,108]. In a purely 1D version of this algorithm, a cost function is derived from the SAD between pixels and a regularization term to control smoothness. The only assumption made is that a displacement estimate at any depth cannot differ by more than 1 sample from the previous estimate; an assumption which holds quite well in reality. Each possible state (represented by nodes in Figure 2.16) for each pixel will have an associated cost.

Because of the recursive nature of dynamic programming methods, the lowest cost path can be found at minimal computational expense. A balance of smoothing parameter needs to be found so that displacement field is not over regulated.

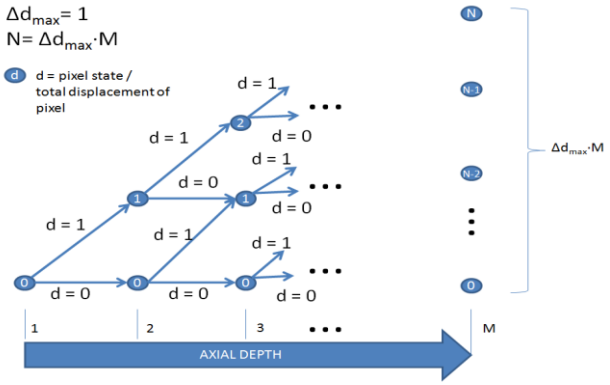


Figure 2.16-Dynamic Programming Method for displacement estimation. *M* is the sample(pixel) depth of the signal

Strain Estimation

As explained in *Eq(2.1)*, strain is defined as the gradient of the displacement field. In signal processing the gradient operator has the unfortunate side effect of amplifying high frequency noise. As a consequence, the predominant method for gradient estimation is that of Least Squares Gradient Estimation (LSGE). The tangent line to any point along the displacement field is approximated using a liner curve fit. The more data points included in the regression, the smoother the output.

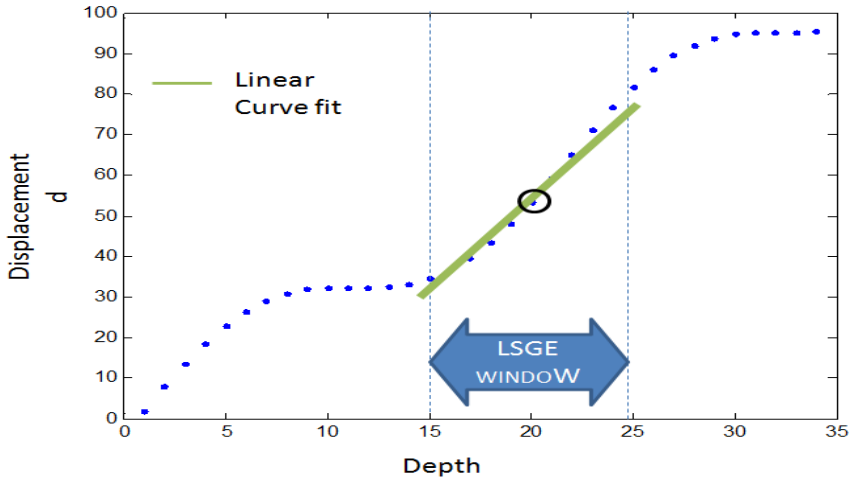


Figure 2.17- Least Square Gradient Estimation (LSGE) from a displacement field

The accuracy of the LSGE strain estimates are also highly dependent on the precision of the displacement field itself, hence the previous work on obtaining precise, high resolution displacement estimates. Moreover, any inaccuracies will also propagate through into the gradient and resulting strain field.

There exist other non gradient based approaches to calculating strain. Consider the model for an ultrasound signal under pre and post compression conditions,

$$x_{post}(t) = x_{pre}(\alpha t + d) \qquad (2.18)$$

where d is the bulk axial displacement (what displacement estimators aim to find) and α is a compression factor, which can be related to strain by $\varepsilon = (1-1/\alpha)$. Temporal stretching methods such as in [4,109-110], apply a range of d, and α until a correlation match of 1 (or very near 1) is obtained. Strain and displacement are thus obtained simultaneously. Results have shown that this method is robust however this time domain approach does suffer from high computational cost and does not presume to become a real time option, with computations times exceeding 1 hour for a single 3D volume [111].

2.5 Conclusion

A number of important conclusions can be drawn from the information presented in this chapter.

Firstly, the motivation for non invasive imaging of breast cancer in therapy has been established. There is currently a strong need for a cost effective method to monitor the efficacy of chemotherapy drugs as well as help determine the true size and extent of a tumour. Moreover, to be of any clinical use this method needs to produce robust and rapid results to cope with the number and the range of patients being treated.

Elastography has been used extensively in various medical applications and using various imaging modalities (ARFI, MRI elastography and freehand quasi-static). Results to date indicate, though not sufficient alone for diagnosis, elastographic measurements provide insight into cancers and could potentially play a role in monitoring tumour response. Moreover, the use of quasi-static US elastography can be a viable solution benefiting from low cost and simple implementation on existing hardware in hospitals. If it can be shown to be sensitive enough (a subject explored by this thesis) it would enjoy great benefits over invasive MR and PET scans.

From the derivation of the elastographic strain equations and the overview of ultrasound imaging and ARFI, it is clear that absolute *quantitative* elastic measurements are prone to a great number of sources of error. Consequently, true tissue stiffness is extremely difficult to quantify reliably. The use of US elastography must therefore lie in strain alone as a pseudo-stiffness measure and the qualitative properties of strain images.

A number of existing strain estimators have been presented in this chapter, each with their own strengths and weakness. None provide a particularly optimal solution to the type of imaging criteria being discussed. Consequently, new algorithms and techniques should be explored. Perhaps a superior solution can be found by combining some of the better aspects of existing techniques.

These conclusions have helped define the scope, set the limitations and steered the design and implementation of this thesis project as the proceeding chapters will indicate.

Chapter 3
Efficient Strain Estimation and Displacement Tracking

3.1 Introduction

This chapter describes a new algorithm for strain imaging. The algorithm is a compromise between fast gradient based methods and slower but more robust adaptive temporal stretching techniques; it aims to take the best of both worlds. Section 3.2 will review the tissue model and derive the strain equation. The two stages of elastography, *displacement estimation* and *strain calculation*, are described in Sect. 3.3 and Sect. 3.4 respectively. Experimental results from 1D simulations, 2D and 3D phantom data will be presented in Sect. 3.5 along with a discussion and conclusion in Sect. 3.6 and Sect. 3.7 respectively.

3.2 Tissue Model

The signal model used to represent tissue deformation is that used in temporal stretching as described in the previous chapter. For completeness, it is presented again here for 3D data. Tissue deformation is modelled as a translation combined with a compression in the axial direction. Thus, for *RF* pre and post compression volumes V_1 and V_2

$$V_2(x, y, z) = V_1(x + \Delta x, \alpha y + \Delta y, z + \Delta z) \tag{3.1}$$

where Δx, Δz model lateral and elevational motion respectively, Δy models the accumulated axial displacement or signal delay due to strain of the surrounding tissue and α is a compression factor related to axial strain, ε by

$$\varepsilon = 1 - \frac{1}{\alpha} \quad , \alpha \geq 1 \tag{3.2}$$

The role of displacement estimation is to obtain values for Δx, Δy and Δz; effectively pairing regions of V_1 and V_2 by related signal content and consequently reducing the problem of calculating $\boldsymbol{\alpha}$ to a simple 1D analysis in the axial direction. Recovering $\boldsymbol{\alpha}$ is the task of the strain estimator described in Section 3.4

3.3 Displacement Estimation

Block matching provides a simple and brute force approach to displacement estimation; take a small window of samples centred about a point in the reference signal, say V_2 and search for the 'best' match, according to some similarity metric, in V_1. Once complete, repeat the process with a new window until the entire region of interest is covered; higher resolution can be achieved by overlapping these windows. As previously mentioned in Chapter 2, variations of block matching techniques form the basis for many quasi-static elastography algorithms. The following method is the absolute equivalent to the aforementioned in terms of output but it eliminates the redundant calculations associated with window overlap, providing maximum resolution at minimal cost. To accomplish this, the concept of integral images is employed.

3.3.1 Integral Images

The integral of a digital signal, image or volume is simply the accumulated discrete summation of signal values, pixels or voxels. A contribution of this thesis is adapting

this simple process to incorporate similarity metrics used in motion/displacement tracking. To serve as an introductory illustration and to provide the reader with the correct mindset before delving into 3D data, consider the following 1D example:

Let the following sequence of numbers represent some signal content:

1 3 5 7 3 3 0 6 ... *-signal*

Its accumulated sum (i.e. its integral) is:

1 4 9 16 19 22 22 28 ... *-integral signal*

Consider the sum of a particular subsequence (or window) of consecutive numbers of the signal e.g. 3+5+7 or 1+3 or 7+3+3+0+6 or 5. It can be calculated via the integral signal by noting the following:

e.g.

7+3+3+0+6 = (1+3+5+7+3+3+0+6) - (1+3+5)

= (28) - (9) ← already pre-computed from integral signal

= 19

Because of this property, the sum of any window of subsequent data values in the original signal can be found through a lookup and subtraction of a pair of corresponding values in the integral signal. This method can easily be scaled up to accommodate any dimension as will be presented next.

2D Integral Images

Consider an image G(x,y) and its integral image $I_G(x,y)$. They are related by the following equation [112]. (Note: here 1 is used as a start index for the first pixel locations to be consistent with MATLAB (*The MathWorks, Inc)*)

$$I_G(x,y) = \sum_{m=1}^{x}\sum_{n=1}^{y} G(m,n) \qquad (3.3)$$

To recover the sum of any rectangular window of pixels of G(x,y), only a lookup and summation of 4 pixel values of I_G are required (see Figure 3.1 below)

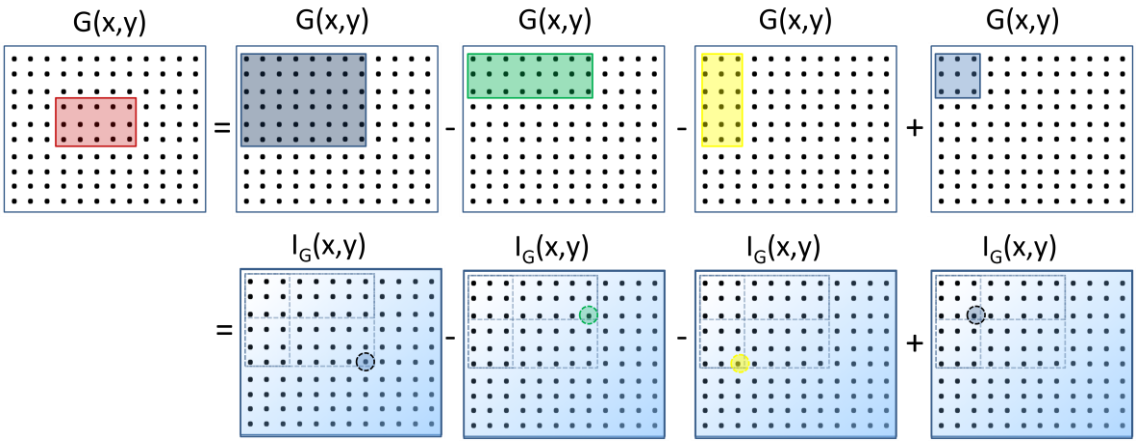


Figure 3.1- The task is to find the sum of pixels of G in the rectangular window indicated in red. The red window can be decomposed into 4 separate windows whose sums can be found easily through a lookup of 4 values of I_G (highlighted and circled)

The sum of any window of G can be found efficiently because I_G has stored within it the pre-computed sums of all possible windows; this is the main feature and motivation for using integral images.

3D Integral Volumes

Given a volume *G(x,y,z)*, its integral volume I_G is defined as

$$I_G(x,y,z) = \sum_{k=1}^{z}\sum_{n=1}^{y}\sum_{m=1}^{x} G(m,n,k) \qquad (3.4)$$

Note the similarity to *Eq(3.3)*. The recursive nature of the calculation is such that I_G ,$\forall\, x, y, z$ can be obtained from a single raster scan of G . Figure 3.2 provides a visual interpretation of *Eq(3.4)*.

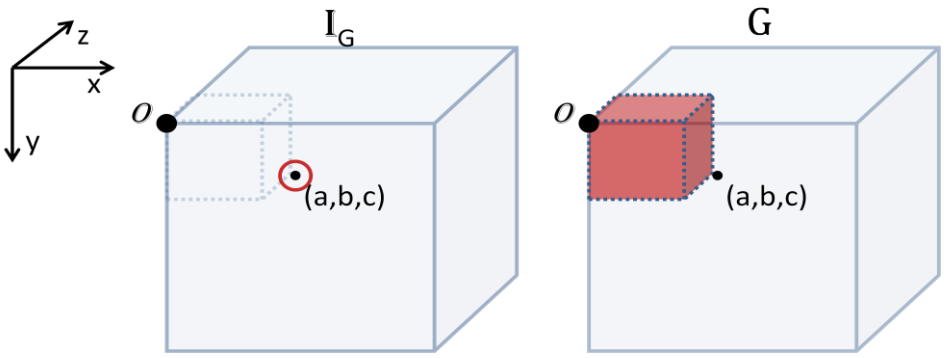


Figure 3.2- Volume G and its integral signal I_G. The value of I_G(a,b,c) is equal to the sum of all the voxels of G located within the red shaded cube region. Hence the sum of many values in G are stored in a single value in I_G.

In order to recover the summation of any arbitrary rectangular/cuboid window (i.e. not necessarily containing the origin as a vertex), the same rationale from the 1D and 2D examples are employed. Consider the following.

Given a cuboid window of *G*, of size (w_x,w_y,w_z) and located at point *(x,y,z)* (here (x,y,z) indicates the vertex closest to the origin), the sum *S* of all voxels within that window can then be calculated via a simple lookup of I_G and addition at its eight vertices, $v_1 \rightarrow v_8$, as depicted in Figure 3.3.

$$S_{W_x W_y W_z}(x,y,z) = \sum_{k=z}^{z+Wz-1} \sum_{n=y}^{y+Wy-1} \sum_{m=x}^{x+Wx-1} G(m,n,k) \qquad (3.5)$$

$$= \sum_{i=1}^{8} sign(v_i)\, I_G(v_i)$$

In this case, *sign(v_i)* takes on a value of ±1 as per Figure 3.3 and Table 3.1. The sum S is a function of both window dimension and position, hence the subscript notation used in *Eq(3.5)*. Note that the numbering of the vertices is arbitrary, the visual depiction in Figure 3.3 provides the best reference. As a rule of thumb: the vertex closest to the origin has a negative sign and all adjacent vertices must then take on opposite signs.

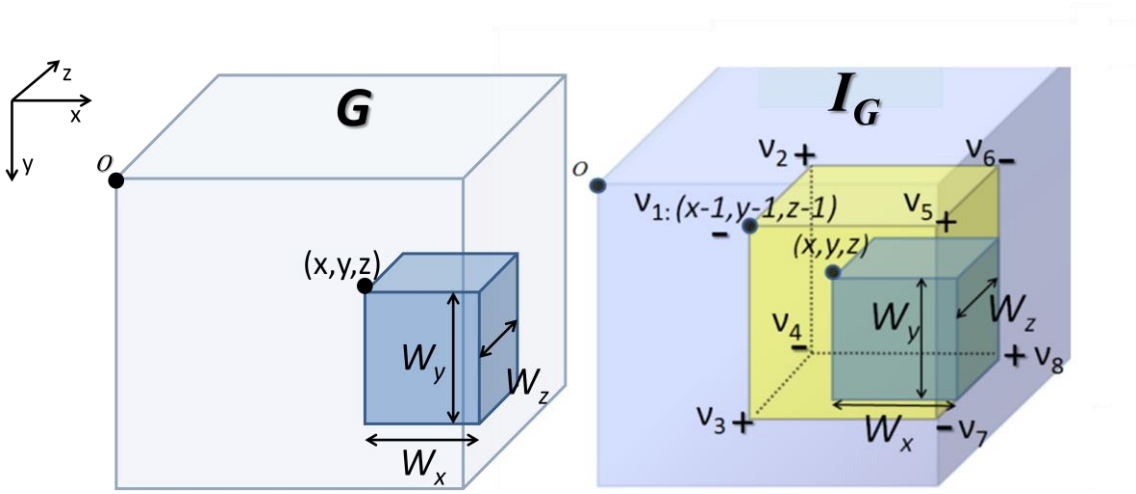


Figure 3.3-Illustration of Integral Volume Methods. The sum of voxels in the cuboid window of G can be recovered from I evaluated at 8 points. Starting with integral volume I_G , take the 8 vertices ($v_1 \rightarrow v_8$) and evaluate *Eq(3.5)* to obtain the sum of all pixels in cuboid window of G located at (x,y,z) with dimensions (*Wx,Wy,Wz*). Use Table 3.1 to keep track of all the vertices and their signs.

Table 3.1- Keeping track of vertices and signs

Vertices	Sign(+/-)
v_1: (x-1,y-1,z-1)	-
v_2: (x-1,y-1,z+W_z)	+
v_3: (x-1,y+W_y,z-1)	+
v_4: (x-1,y+W_y,z+W_z)	-
v_5: (x+W_x,y-1,z-1)	+
v_6: (x+W_x,y-1,z+W_z)	-
v_7: (x+W_x,y+W_y,z-1)	-
v_8: (x+W_x,y+W_y,z+W_z)	+

3.3.2 Similarity Metrics

Thus far, the integral of a 3D volume and the method to recover the sum of voxels within an arbitrary cuboid window using a lookup of values of the integral signal has been described. In the following section, the method will be adapted to incorporate similarity metrics.

As an illustrative example, consider the sum of squared differences (*SSD*) similarity metric. Let G (the same G from *Eq(4.3)*) be the result of the squared difference (*SD*) between a pair of 3D images (i.e. volumes) V_1 and V_2 for a particular displacement $\Delta x,\Delta y,\Delta z$. That is,

$$G(x,y,z) = (V_2(x,y,z) - V_1(x+\Delta x, y+\Delta y, z+\Delta z))^2 \tag{3.6}$$

Then *S* in *Eq(3.5)* will now correspond to the *SSD*; a 3D array of similarity metric scores for *a given trial displacement* $(\Delta x,\Delta y,\Delta z)$. and a particular *fixed window size* (W_x,W_y,W_z). A displacement vector, $\vec{D}(x,y,z)$ for each voxel can then be obtained via

$$\vec{D}(x,y,z) = \underset{\Delta x,\Delta y,\Delta z}{arg\min} S_{W_xW_yW_z}(x,y,z) \tag{3.7}$$

$$\Delta x_{min} \le \Delta x \le \Delta x_{max}\,, \qquad \Delta z_{min} \le \Delta z \le \Delta z_{max}, \qquad 0 \le \Delta y \le \Delta y_{max}$$

Thus a particular displacement estimate is evaluated on the entire volume (all possible windows) first before a new displacement is tried. This rather resembles the brute force block matching technique *in reverse*. The advantage of using the integral volume method is that window overlap simply does not factor into the calculation; each value of D(x,y,z) will generally be unique and thus will be equivalent in output to standard block matching using *maximum* window overlap. Each voxel in V_1 will be compared (e.g.

subtracted and squared) to a voxel in V_2 only once with the sum stored in the integral signal allowing for analysis for any size window at any level of overlap without these operations needing to be repeated. Thus, all redundancy associated with window overlap is removed or rather reduced to a lookup and addition/subtraction of 8 vertices.

Constraints on the trial displacement range (Δx_{min}, Δx_{max}, Δz_{min}, Δz_{max}, Δy_{max}) are set to appropriate values given the application. Both $D(x,y,z)$ and $S_W(x,y,z)$ are updated/overwritten upon each trial, making an efficient use of memory. In practice, the displacement estimates are subsequently reallocated such that they correspond to the centre point of the chosen search window. As tissues closer to the probe face will tend to displace less axially relative to tissues at greater depths, further computational and memory savings can be made by subdividing the volume into horizontal slices, each set with a different Δy_{max}, effectively adjusting the axial search range with depth.

By altering *Eq(3.6)*, the method can also be adapted to accommodate other similarity metrics. The Sum of Absolute Differences (SAD) can be handled simply by substituting *Eq(3.8)* for *Eq(3.6)*. Normalized Cross Correlation (NCC) is slightly more complicated due to the need for normalization. Consider the equations *Eq(3.9a,b,c)*; additional integral images are computed to account for the required normalization factor. However, G_2 is only necessary if a correlation value of 1 is desired; S_2 has no bearing on corresponding displacement estimates, D_{NCC} (*Eq(3.10)*) since it corresponds to an unchanging reference signal.

$$G(x,y,z) = |V_2(x,y,z) - V_1(x+\Delta x, y+\Delta y, z+\Delta z)| \tag{3.8}$$

$$G_1(x,y,z) = (\, V_2(x,y,z) \cdot V_1^*(x+\Delta x, y+\Delta y, z+\Delta z) \tag{3.9a}$$

$$G_2(x,y,z) = (\, V_2(x,y,z) \cdot V_2^*(x,y,z)) = \|V_2\|^2 \tag{3.9b}$$

$$G_3(x,y,z) = (V_1(x,y,z) \cdot V_1^*(x,y,z)) = \|V_1\|^2 \qquad (3.9c)$$

$$\vec{D}_{NCC}(x,y,z) = \underset{\Delta x,\Delta y,\Delta z}{argmax}\left(\frac{S_1(x,y,z)}{\sqrt{S_2(x,y,z)} \cdot \sqrt{S_3(x+\Delta x, y+\Delta y, z+\Delta z)}}\right) \qquad (3.10)$$

$$= \underset{\Delta x,\Delta y,\Delta z}{argmax}\left(\frac{S_1(x,y,z)}{\sqrt{S_3(x+\Delta x, y+\Delta y, z+\Delta z)}}\right), \qquad S_i \rightarrow defined\ as\ per\ Eq3.4$$

3.4 Strain Calculation

After motion tracking, related signal content from each volume can be paired off. The goal is to now recover α from *Eq(3.1)* and *Eq(3.2)*. The following section describes how this can be accomplished using a *spectral shift* technique. The centre axial RF lines of each window pair from V_1 and V_2 are subjected to Fourier analysis. Let $x_1(t)$ and $x_2(t)$ represent respectively a pre and post compression axial RF line pair, then their spectra $X_1(k)$ and $X_2(k)$ can be described by

$$\mathcal{F}\{x_2(t) = x_1(\alpha t)\} \quad \rightarrow \quad X_2(k) = \frac{1}{\alpha} X_1\left({}^{k}/_{\alpha}\right) \qquad (3.11)$$

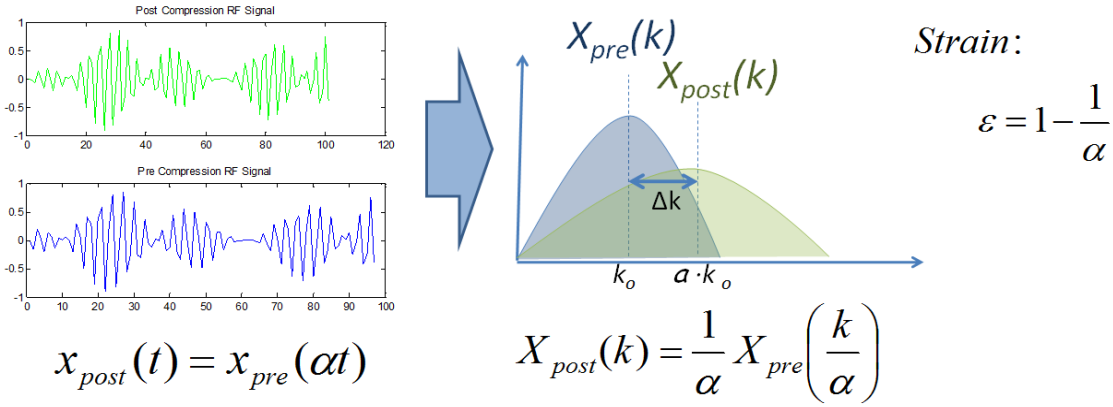


Figure 3.4-Theoretical Spectra of pre and post compression signals $x_1(t)$ and $x_2(t)$. Note: IQ demodulation preserves this relationship of the original RF signal

In [113-114], the author goes into in-depth analysis of multiple techniques of measuring strain through the spectral shift phenomenon. The simplest way is to simply locate the peak in each spectrum and measure the distance from peak to peak. However this method was found to be the least reliable due to the max peak's susceptibility to noise. The stretching of the spectrums in Figure 3.4 due to α can be treated as a simple translation (for small strains this is a reasonable assumption) which can be computed using shift estimation via similarity metrics like the now familiar SAD, SSD and NCC. NCC was found to provide the best results but because of their lower computational cost and comparable performance, SSD and SAD were considered as good compromises.

Given a large 3D volume, 2 FFTs and 1 cross correlation (or related operations for SSD and SAD) per voxel amounts to a significant computational load. Unfortunately, there would be no benefit in using the proposed displacement estimator. The method described in Sect 3.3 only has computational advantage when overlap in the reference signal window is used; this situation does not apply for the spectral shift estimates.

In actual fact, this thesis will demonstrate that using very elementary signal processing techniques, NCC can be made to be the fastest, most computational efficient method of the three options. Making use of the cross correlation (CC) theorem (used in reverse in this case), *CC* can be carried out simply by:

$$X_2 \otimes X_1 = \mathcal{F}^{-1}\{x_2 x_1^*\} \tag{3.12}$$

where * denotes the complex conjugate and X_1 and X_2 are the Fourier Transforms of time valued signals x_1 and x_2 respectively. This is also commonly known as the Phase Correlation Method. This reduces the computation to a single FFT and element-wise vector multiplication per voxel. Note also that the correlation is circular; normally a

concern in signal frequency analysis. However, in this case the frequency wrapping is precisely what is required for accurate shift estimate; it is a desirable side effect.

The shift Δk, can be found effectively via the maximum of the CC of the spectrums (see Figure 3.4) .

$$\Delta k = \underset{\Delta k}{arg\max}\{X_2(k) \otimes X_1(k)\} \tag{3.13}$$

Also from Figure 3.4 and making use of ε=1-1/α, Δk is directly related to strain by

$$\varepsilon = \frac{\Delta k}{\Delta k + k_o} \ , \quad k_o = \frac{f_o}{f_s} \cdot (N_{FFT} - 1) \tag{3.14}$$

Here f_o is the probe centre frequency, f_s is the axial sample rate of the signal and N_{FFT} is the size of the FFT used. FFT size is directly related to the number of strain 'bins' available and consequently the precision of the strain output. Let the precision or resolution of the strain output $\Delta\varepsilon_{MIN}$ be defined as the strain resulting from the smallest shift detectable i.e. $\Delta k=1$.

$$\Delta\varepsilon_{MIN} = 1/(1+k_o) \tag{3.15}$$

Figure 3.5 depicts the effects of the signal sample rate f_s and FFT size, $N_{FFT,}$ on $\Delta\varepsilon_{MIN.}$

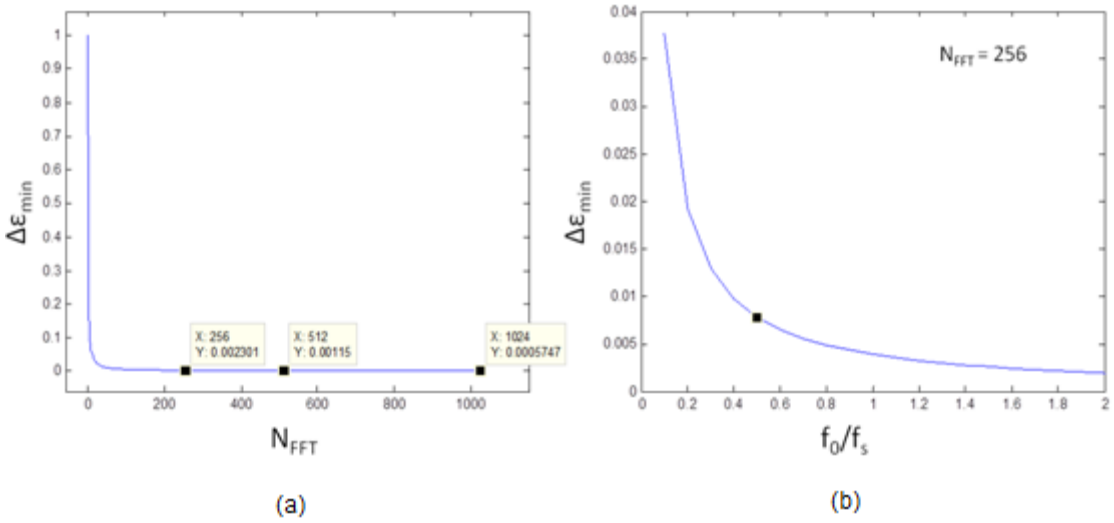


Figure 3.5- (a) Effects of FFT size on strain output precision with fo/fs set at 1. Precision increases with N_{FFT} and decreases with sample rate. (b) Effects of Sample rate on Strain calculation precision.

Figure 3.5 reveals some insight into the proposed strain estimator performance which has helped in the selection of parameters used in subsequent imaging. Figure 3.5(b) shows that precision in the strain estimate actually improves with lower sample rates (keeping N_{FFT} fixed). This is due to the fact that the same number of FFT 'bins' cover a smaller range of frequencies at lower sample rates.

The centre frequency of the probe f_0 is typically on the order of several MHz. It is important to keep in mind that because of IQ demodulation, the sample rate *fs* need only meet the Nyquist sampling criteria for the signal's bandwidth. Ultrasound signal bandwidth is related to the machine's PSF and also on the material being imaged (Chapter2: Figure 2.13). Consequently, finding the lower limits on *fs* are better left to empirical methods. In Sect 3.5.2, the effects of downsampling this signal in the axial direction will be examined.

Figure 3.5(a) demonstrates that a higher N_{FFT} gives better strain estimate precision. The precision increases approximately linearly with N_{FFT} above a certain threshold, however the complexity of the FFT is N_{FFT} log(N_{FFT}). For the experiments that follow, an N_{FFT} of 256 was chosen as a compromise between precision and computational speed resulting in a $\Delta\varepsilon_{MIN}$ of ~0.2% strain.

3.5 Experiments

The validation of the proposed algorithm will be presented in 3 main subsections; 1D, 2D and 3D experiments. The rationale and steps behind this validating stage are as follows:

In Sect 3.5.1, given the model being used synthesize a signal based purely on it and verify that the algorithm actually works i.e. check that spectral shift is in fact detectable in this ideal case. It has been noted that the choice of window size used in block matching/displacement estimation has significant effect on the accuracy and precision of the displacement field. It is important to examine how the resulting strain estimates are affected by this. A comparison with the LSGE algorithm, the popular gradient based method, will help illustrate the strengths of the spectral shift method.

The next section (Sect.3.5.2), proceeds on to real 2D ultrasound data from gelatine phantoms (phantoms can be made with some control over their acoustic and elastic properties). These experiments aim to evaluate the proposed algorithm performance on real ultrasound data under controlled conditions. Specifically, it will be compared to the LSGE method and the effects of parameters like window size and sample rate will be examined.

Lastly,Sect.3.5.3 investigates the performance of the 3D algorithm on phantom and real clinical datasets.

3.5.1 1D Simulations

In order to demonstrate the robustness of the frequency domain approach, 1D pre and post compression RF signals were simulated in MATLAB. Consistent with simulated data found in the literature [107,115], the signals were created using 10^4 randomly distributed scatterers over a depth of 50mm, with a sample rate of 30MHz and assuming a speed of sound of 1540m/s. Convolution with a theoretical PSF (Gaussian modulated sinusoid with centred frequency of 7.5MHz) produced the RF signal. The theoretical displacement and strain profiles are displayed in Figure 3.6. The simulation depicts an ideal case with no out-of-plane or lateral motion and shows the effect of the chosen window length on displacement estimation accuracy and precision.

The strain profile was chosen to simulate a small hard inclusion of ~5mm that is around 3-4 times stiffer than its surroundings. This case approaches the minimum expected strain contrast ratio for useful elastographic imaging; meaning a tough case for the algorithms to perform on.

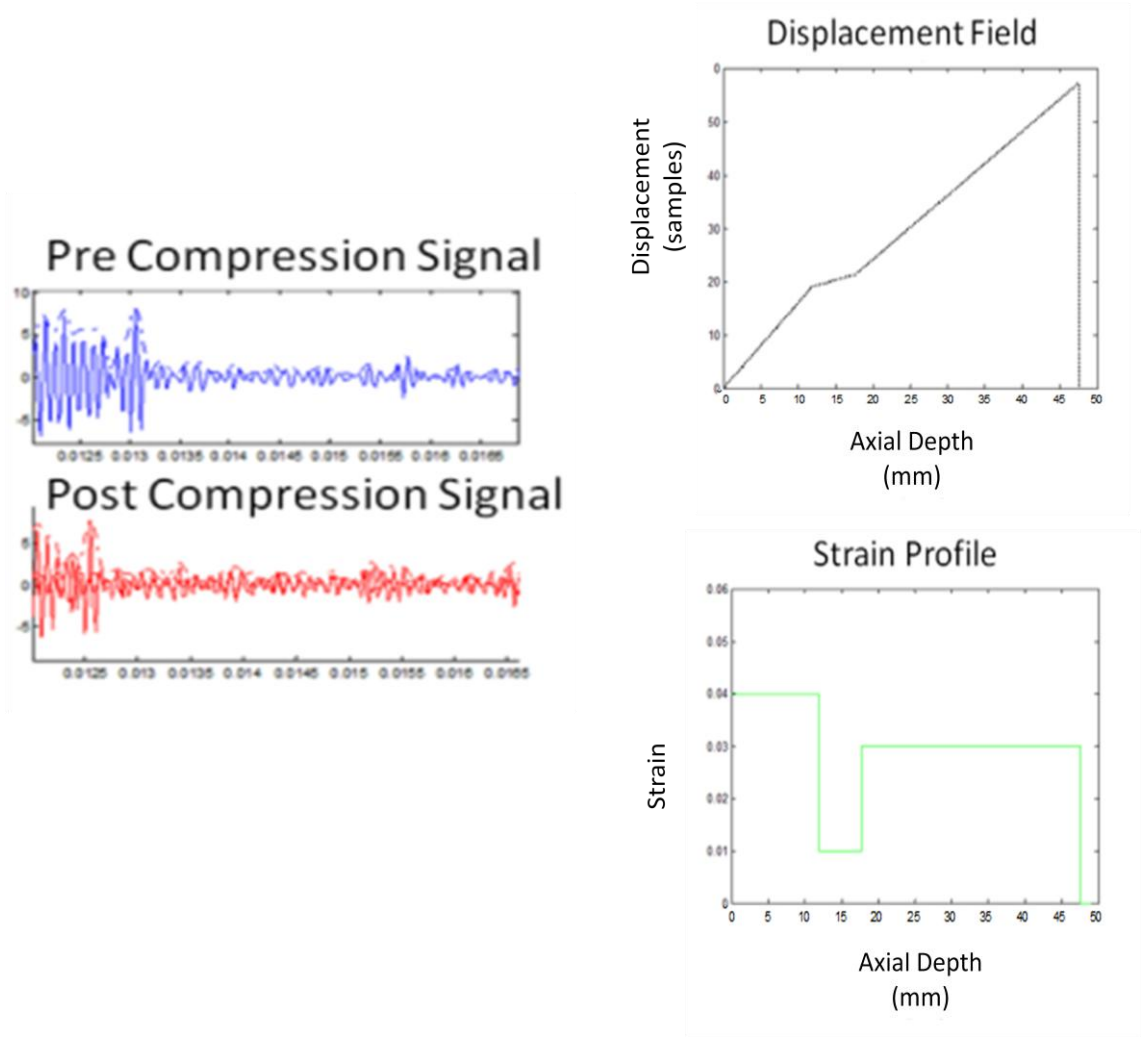


Figure 3.6- (a) Simulated Pre and Post Compression Signals, (b) Theoretical Displacement and (c) Strain Profile.

An optimal window size could be obtained for this case by selecting a range of test window sizes and evaluating the minimum mean squared error (MMSE) between theoretical and estimated displacements (Figure 3.7). In this case, windows between 1-3mm showed relatively consistent and low MSE.

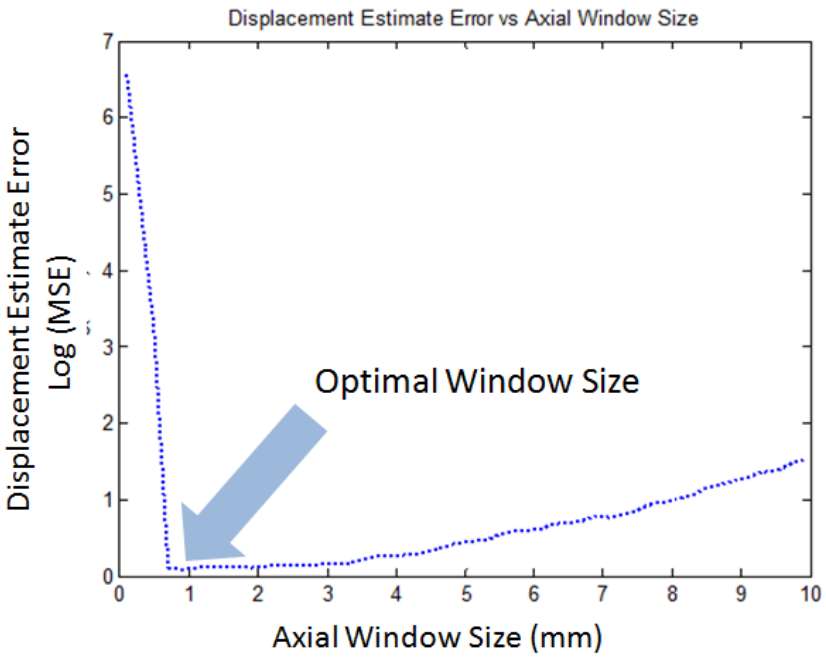


Figure 3.7-The effect of window size on displacement estimation error; log(MSE) between estimated and theoretical displacement fields for window sizes [0.1mm-10mm]. Optimal window size corresponds to the MMSE

Results of the proposed strain estimation method compared to a standard gradient based approach using Least Squares Gradient Estimation (LSGE) are shown in Figure 3.8.

The spectral shift method is inherently bound by [0 1] which is appropriate given the physical interpretation of strain values. The LSGE method on the other hand is not bounded. In Figure 3.8 at both 0.5mm and 8mm the LSGE estimate shoots off outside the displayed range of strain values due to noisy curve fits resulting in strains well above 100% and below 0% (as LSGE can potentially give negative strains as well).

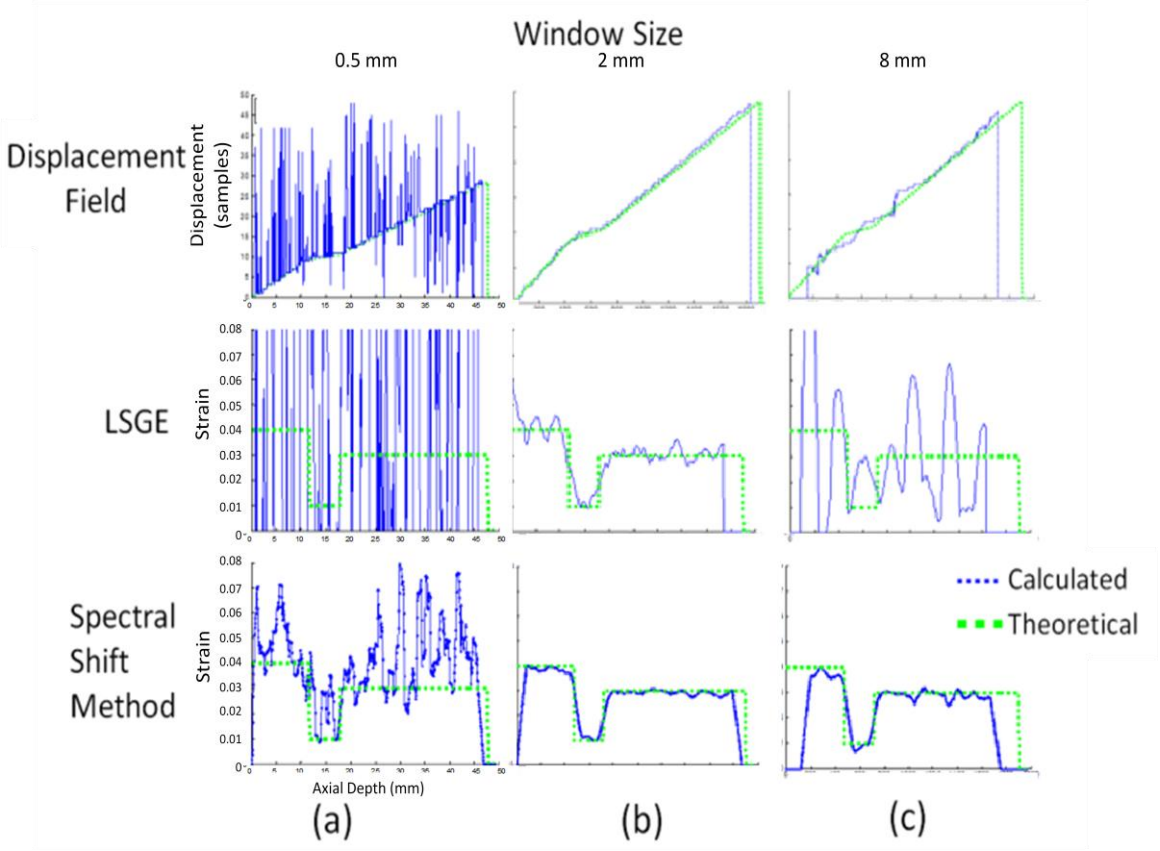


Figure 3.8- (Top to Bottom) Displacement Estimate, Strain output from LSGE, Strain output from Spectral Shift method using window sizes of (a) 0.5mm, (b) 2mm, (c) 8mm for displacement estimation. Both the LSGE and Spectral Shift were calculated on a 2mm segment of signal located at the centre of each search window.

Next, a range of window sizes from [0.1mm-10mm] was used to generate displacement fields which were subsequently fed into the strain estimators. The mean squared error (MSE) between theoretical and estimated strain was used as a performance measure and is displayed in Figure 3.9. Note, the Spectral Shift method exhibits a flatter curve over a wider range of window sizes and is lower overall when compared to the LSGE method.

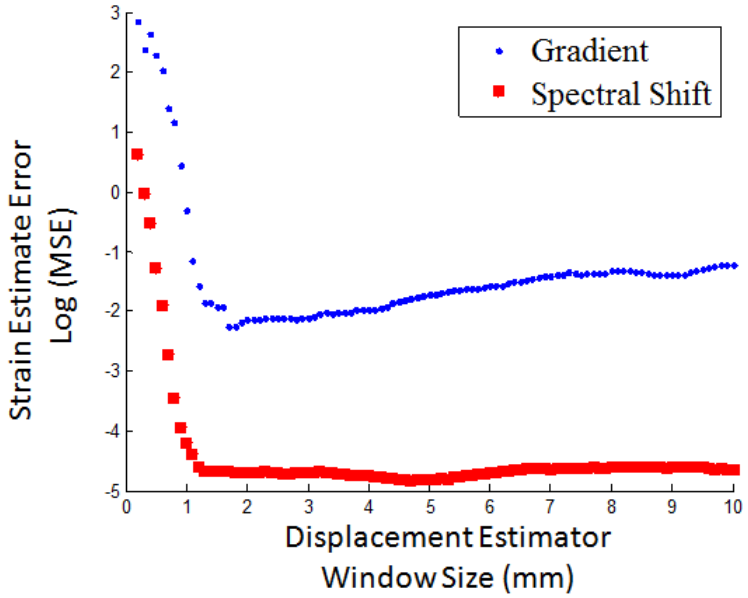


Figure 3.9- log(MSE) between calculated and theoretical strain profile. Displacement fields generated using window lengths (0.1mm - 10mm) were inputted into the strain estimators. Spectral Shift and LSGE were calculated using a 2mm kernel.

3.5.2 2D Experiments

A number of gelatine phantoms were constructed using a phantom making recipe found in [116-118]. Using this recipe, it was possible to control the stiffness of the phantoms as well as adjust the contrast observed in B-mode.

Experimental setup 2D

All scans were performed using freehand compressions using a Zonare z.one system and L10-5 probe (8.5 MHz with a footprint of 38.4mm and axial depth set depending on the application and target being scanned (usually 40.0 or 50.0mm)). Zonare (ZONARE Medical Systems, Inc., Mountain View CA, USA) has a research package (RP) that gives access to raw RF data demodulated into IQ format. A diagram of the hardware setup is shown in Figure 3.10. The US machine was controlled through a serial port connection by a PC laptop using a purpose built MATLAB graphical user interface

(GUI) which allowed for simple I/O control over experiments, input of relevant data and frame selection. Approximately 6 seconds worth of frames (at 15-25 Hz frame rate) could be stored in the z.one's cine memory buffer. After pressing the 'freeze frame' button on the machine (or through a command from the PC) a selection of contiguous frames could then be transferred onto a USB memory stick. An additional command could then transfer these frames from the USB stick directly to the PC via an FTP connection with a crossover Ethernet cable. Theoretically, the system could allow for real time processing to be conducted on the PC. In practice, data was transferred in large sets of contiguous frames (~20-30) at a time for post processing later and did not provide a practical means to review the data while subjects were still being scanned.

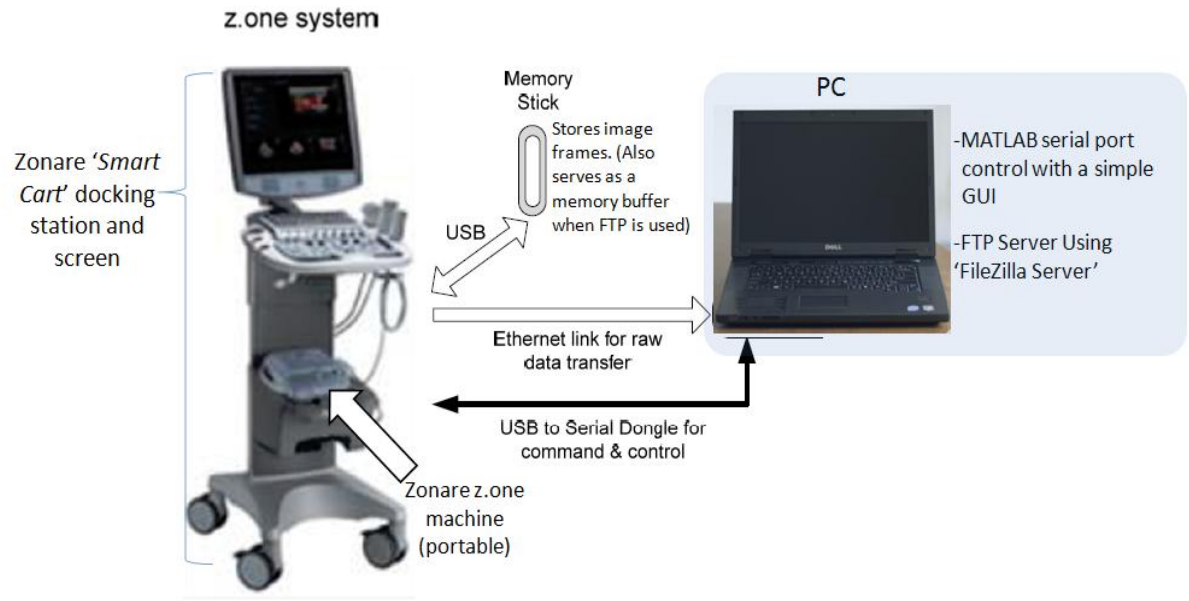


Figure 3.10- Hardware Setup Diagram for Zonare RP

A pair of pre and post compression images were selected empirically through visual observation of the frame sequence play back and noting that large deformation gives good strain contrast in images provided the incurred motion can be tracked. Signal

correlation (and motion tracking accuracy) diminishes with large deformation. Hence, a balance needed to be achieved. This is why in Chapter 4, a method to assess the quality of the displacement and strain data is presented.

The default *'jet'* colour mapping in MATLAB was used to display strain images, making low strain appear as red and high strain tending towards blue. This was a colour scheme preferred by clinicians in this project and unless otherwise indicated, the default for all images presented in this thesis.

Strain Ratios

In Figure 3.11 we see the displacement fields (axial and lateral) and strain image for a gelatine phantom. The circular inclusion was constructed to have a strain ratio of approximately 3:1 relative to its surroundings. After manual segmentation, average strain inside the circular occlusion was measured to be 0.0076 (0.76%). Outside, it was measured to be 0.0236 (2.36%) for a ratio of 3.1:1.

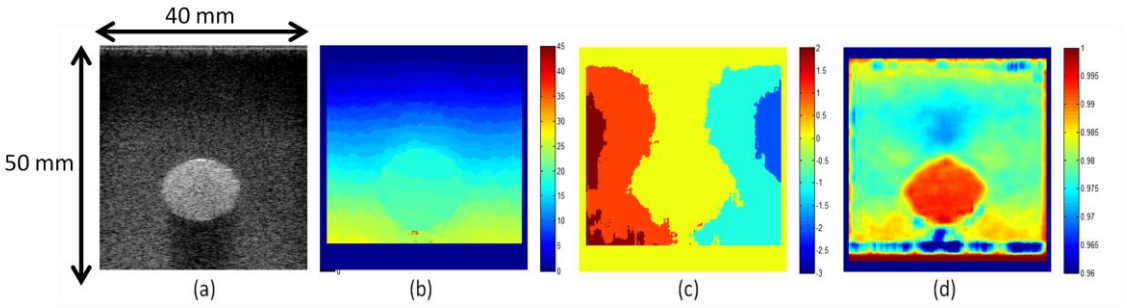


Figure 3.11-(a) Bmode Image, (b) Axial Displacement Field, (c) Lateral Displacement Field, (d) A pseudo Strain Image (1-Strain) of a gelatine phantom facilitates the colour mapping scheme. Circular inclusion has a stiffness approximately 3x greater than its surroundings

Figure 3.11 highlights the effects of real world freehand compression and how it relates to the elastography model. The Poisson effect is clearly apparent in Figure 3.11(c) as an axial compression causes lateral expansion of the gelatine. In Figure 3.11(d) it can be observed that the applied external stress does not distribute itself evenly throughout the image plane. This can be seen in the area of low strain directly above the circular inclusion; the gelatine stiffness should be approximately uniform. This emphasises the difference between strain imaging and true elastic modulus reconstruction.

The scan was repeated several more times. Using a freehand approach to scanning meant that slight variations in applied pressure and resulting deformation occurred causing the strain image to change accordingly. Nonetheless, the overall ratio remained at approximately 3:1 in all cases.

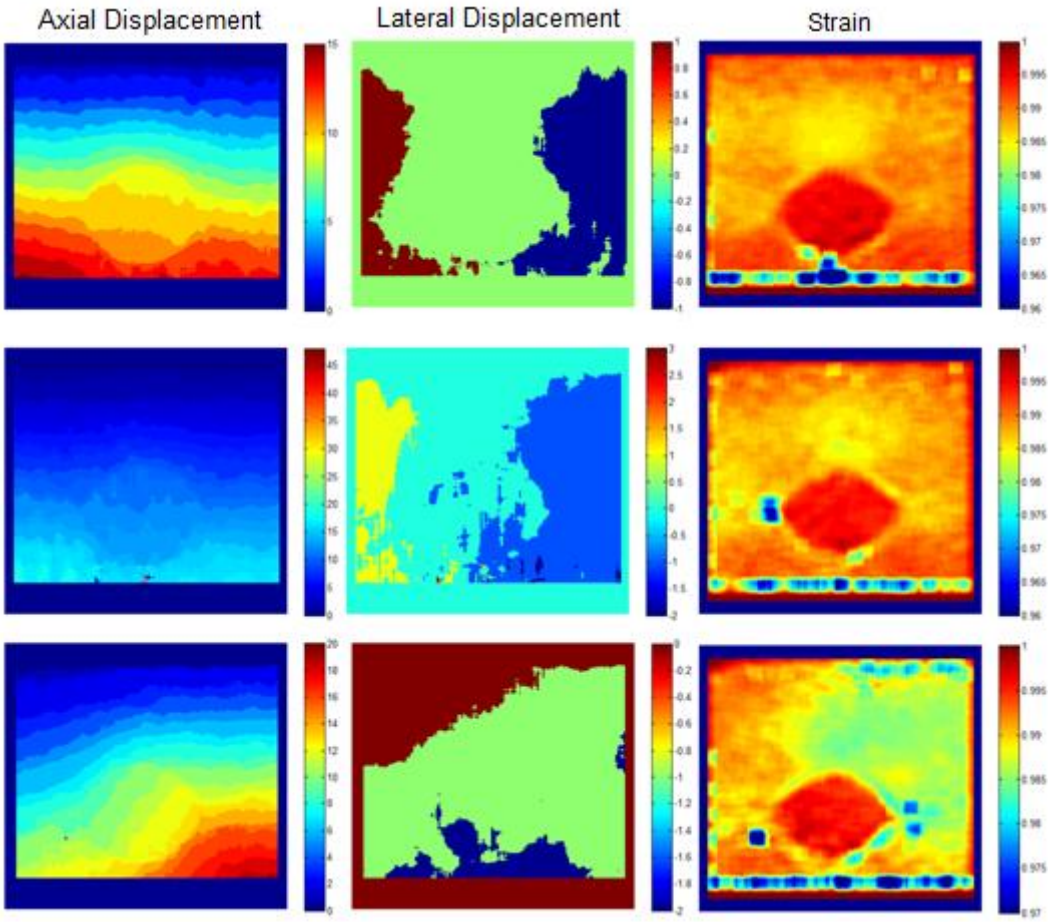


Figure 3.12 - Phantom experiment repeated 3 more times (top to bottom)

All of the strain images in Figure 3.12 are displayed with the same dynamic range limits despite the fact that the externally applied stress will have varied due to freehand inconsistencies. Consequently, the images appear to display very different qualitative information despite having an agreed strain ratio of 3:1. The need for an image normalisation technique is evident; Chapter 4 will present a method to deal with this problem. Also due to freehand scanning are variations in the overall tissue motion; in some cases it was as much lateral as axial (e.g. bottom row of Figure 3.12). A few artefacts (dark blue spots to the left and right of the inclusion) are also present in the second and third row of strain images of Figure 3.12. This can be attributed to loss of signal correlation at these points from possible slip/out-of-plane motion. Freehand acquisition is thus a significant source of noise in quasi static elastography but meaningful data can still be obtained from these images.

Effects of Window Size

Having been suggested by preliminary 1D results, the choice of window size should have negligible effects on the resulting strain image produced by the spectral shift technique. In this experiment, the axial window size used for displacement estimation was altered, producing a range of displacement fields with varying noise and bias. The effects on the corresponding strain images were observed. The strain images show little variation (compared to the same results from the LSGE) despite a significant loss of precision in the displacement field.

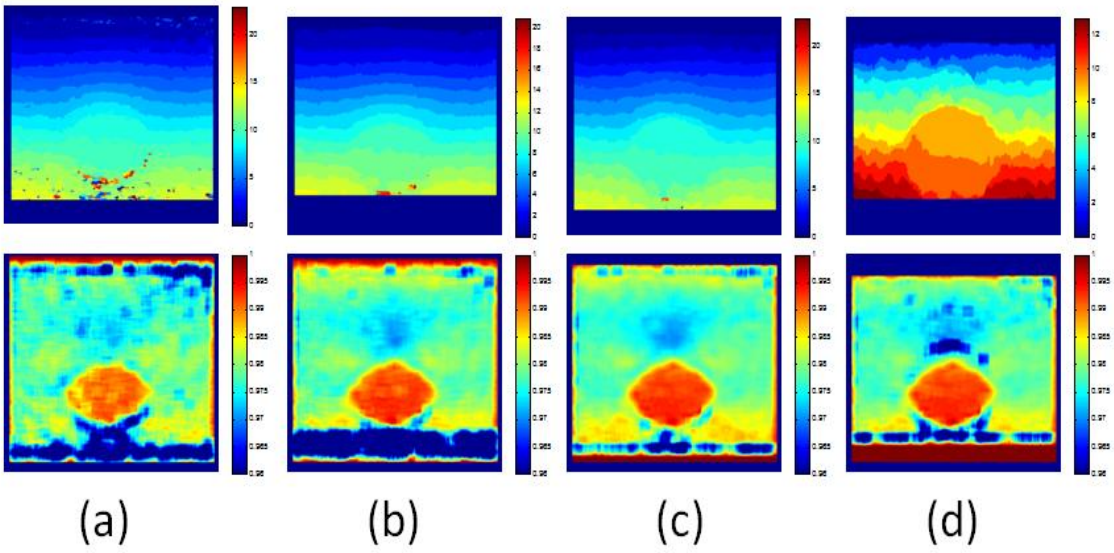


Figure 3.13-(top) Axial Displacement Fields, (bottom) Strain Images using a axial window size of (a)1mm,(b)2mm,(c)5mm and (d)10mm. Lateral window size was fixed to 1.5mm

For a comparison the same experiment was conducted using the LSGE method. In Figure 3.14 the top row of images were produced using a 3mm kernel size for the LSGE (consistent with the kernel size used in determining the spectral shift in Figure 3.13). A 10mm kernel was also employed to see if smoothing the LSGE results could provide a discernible improvement to the images (Figure 3.14; bottom row). All the images fail to provide good shape definition and consistent strain values.

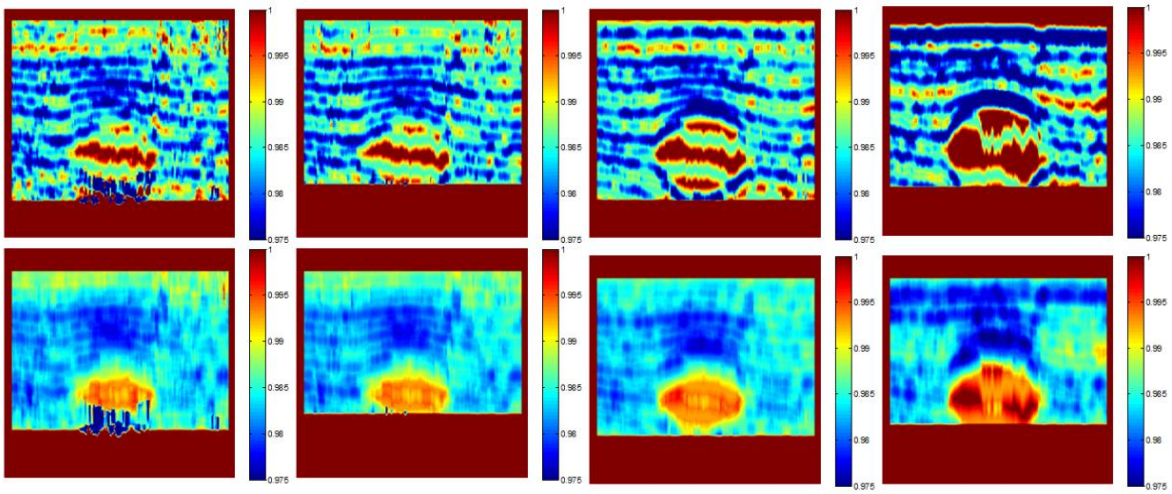


Figure 3.14- Using a small window of 3mm resulted in noisy data. A larger window of 10mm was produced overly smooth results which distorted the shape and size of the lesion.

Effects of Down Sampling

Ultrasound signals are often oversampled to reduce signal to quantization noise and facilitate hardware filter design. In addition, from Figure 3.5 we know that the precision in the strain estimates actually improves as the sample rate is reduced (provided the Nyquist sampling criteria still holds). Lower sample rates also result in smaller file sizes, memory use and computation time. An algorithm that can function at low sample frequencies is of great benefit.

This experiment examines the effects of changing the axial sample rate on the strain output. For comparison, the LSGE was also computed using the same set of resulting displacement fields (Figure 3.16).

Zonare IQ data was obtained at a default sample rate of 16 MHz. For image dimensions of 1040x241 corresponding to an actual size of 50.0mmx38.4mm (assuming speed of sound, c=1540m/s) this equates to 20.8 samples/mm (axial) and 6.28 samples/mm (lateral).

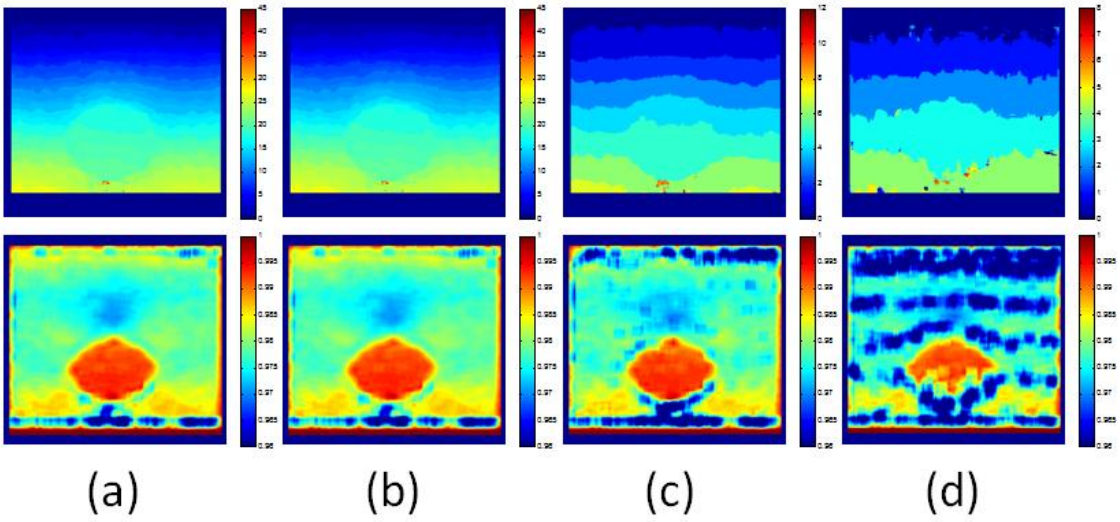


Figure 3. 15- (top) Axial Displacement Fields (bottom) Strain Images for down sampling factors, dsf, of (a)1 (no down sampling), (b)3,(c)4 and (d) 6. Displacement Estimate Window was fixed at 5 mm. with 3mm strain kernel

The algorithm is able to clearly delineate the circular inclusion down to a sample rate of 4 MHz (Figure 3.15(c)). At ~2.67 MHz (Figure 3.15(d)) the data is not completely unintelligible but is generally poor. The same analysis using a gradient operator (LSGE) performs much worse even at higher sample rates (Figure 3.16)

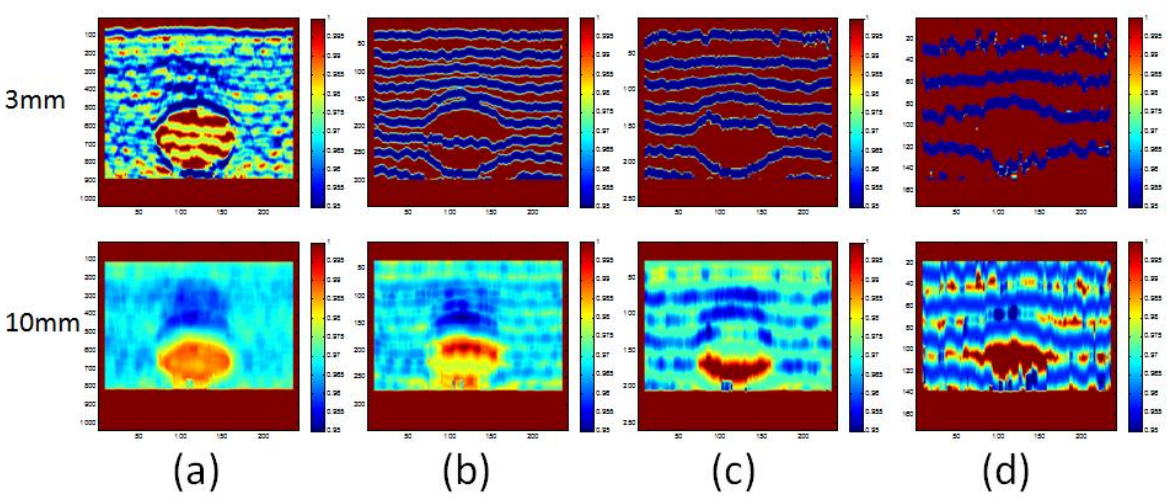


Figure 3.16--(top) Using a 3mm LSGE kernel (bottom) Using a 10mm LSGE kernel, Strain Images for dsf, of (a)1 (no down sampling), (b)3,(c)4 and (d) 6. Displacement Estimate Window was fixed at 5 mm.

2.5.3 3D Experiments

A freehand scan of a CIRS breast phantom [Computerized Imaging Reference Systems, Incorporated , *Norfolk, Virginia, USA*] was performed. The phantom consists of randomly distributed spherical inclusions which are at least 2 times stiffer than their surroundings according to the manufacturer. The inclusions range in size from 3,4,6,8 and 10 mm. The background has a stiffness of 20kPa±5kPa (a rather large 25% margin for error). The phantom is also isoechoic, meaning that the inclusions themselves cannot be seen in regular B-mode imaging. This made scanning for them problematic. Regions were randomly selected and scanned with no visual cues from the US machine's monitors for guidance. However, there are several advantages in using such a phantom over a 'home-made' gelatine one. The shape and surface curvature are more comparable to a real breast and consequently produce more realistic boundary conditions. Also, the CIRS phantom has an indefinite shelf life (unlike gelatine which eventually dries out or putrefies)

Data was acquired using a Zonare C8-3 3D probe, with centre frequency set to 6 MHz. Signals were extracted in their demodualted *i*n-phase and *q*uadrature (*IQ*) components. The C8-3 is a curved array sector probe which pivots its 2D transducer array about an axis spanning up to a 75 degree field of view in the elevational direction.



Figure 3.17-The C8-3 3D probe from Zonare

An important note on 3D data acquisition: though the C8-3 probe was capable off scanning a 3D volume in approximately 1 sec, only 1 volume could be extracted off the Zonare machine at a time (the memory buffer would not allow 2 volumes to be stored simultaneously). This left a minimum of 20-30 seconds between volume acquisitions for an effective frame rate of 0.05 Hz at best. For many patients in clinic, holding ones breath and remaining still for 30 seconds is exceedingly difficult. This only exacerbated the effects of freehand manipulation of the probe. In addition, the probe had relatively low spatial resolution brought on by the probe's PSF.

Consequently, an assisted freehand approach need to be adopted to conduct these experiments. The setup is depicted in (Figure 3.18); a light press downward on the clamp arm created a near axial movement of the probe into the phantom. The post

compression image was then scanned and acquired. While the above mentioned processing was taking place to extract the data, pressure on the clamp was released allowing the CIRS phantom to rebound and push the probe back up. Because the probe was clamped in place, the second volume (pre compression) could be acquired as soon as the first extraction was complete (~20 seconds later). This mitigated the lateral and elevational movement of the probe and thus mitigated decorrelation noise between the pre and post compression volumes. The round face of C8-3 and the curved surface of the CIRS phantom meant that the experiment was unlikely to achieve perfect axial compression/decompression motion.

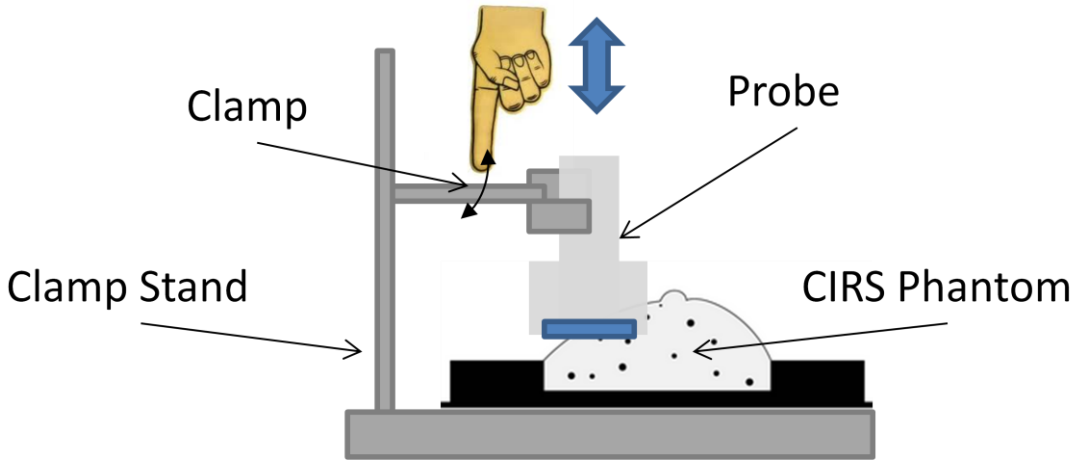


Figure 3.18- Experimental Setup for 3D phantom studies

Acquired volumes were first remapped to a Cartesian grid using tri-linear interpolation before applying the strain algorithm. The exact dimensions of the probe were provided by Zonare to allow for a reliable reconstruction of Cartesian data from sectorial coordinates.

The results of the scan are displayed in Figure 3.19. The image dimensions are 320x144x100 (axial x lateral x elevational) samples covering an actual volume of approximately 60mm x 40mm x 40 mm. The window used for displacement estimation

was 5mm x 3.5mm x 3.5mm and spectral analysis was carried out using 3mm length kernel with an FFT size of 128. The FFT size should be chosen to be at least the size of the sampled window to avoid signal truncation. Other parameters: Δy_{max} was set to allow for up to 6% average axial strain to be considered and $\Delta z_{min} = \Delta x_{min} = -2$, $\Delta z_{max} = \Delta x_{max} = 2$.

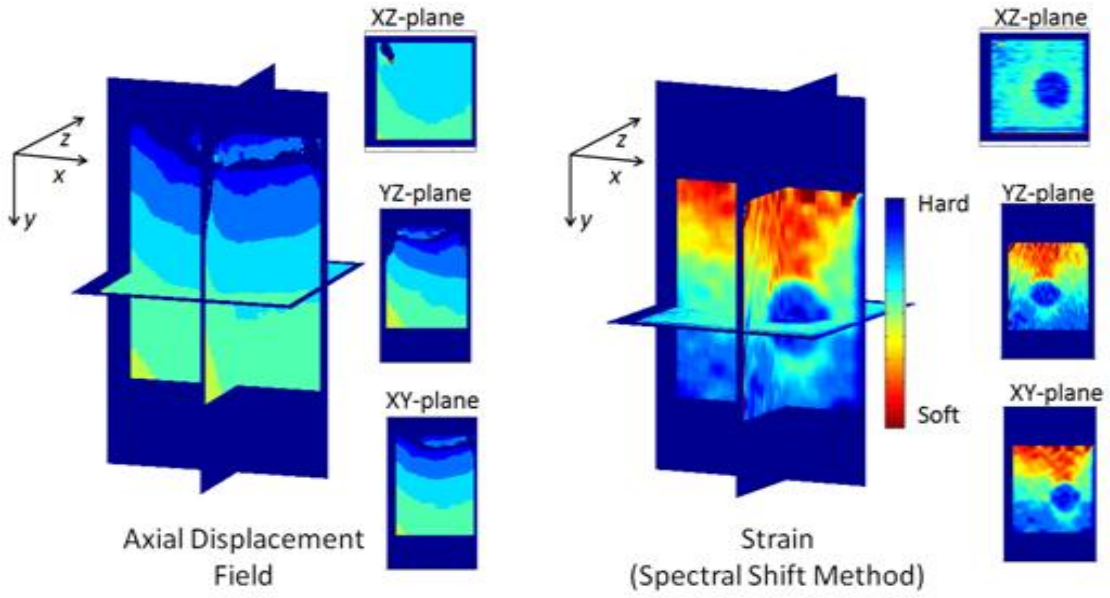


Figure 3.19-3D Displacement Field and Strain image from the CIRS Breast mimicking phantom.

The experiment was repeated several more times; under different probe settings and imaging different inclusions in the phantom.

In the first case, the scan was simply repeated using the same region of interest and the same probe settings and as those for Figure 3.19. The result in depicted in Figure 3.20(a).

Next, the probe frequency settings were altered. The harmonic imaging feature of the Zonare z.one machine was put to use. Harmonic imaging effectively doubles the *axial* resolution of imaging system. The result is shown in Figure 3.20(b).

As the scans were effectively preformed independently, slight variations due to probe motion have manifested itself into the resulting displacement fields. However, the spherical hard inclusion is ever present and discernible. Moreover, the average maximum diameter of the inclusion in the 3 cases was measured as 9.6 mm (a 4% error assuming an actual 10mm inclusion) with a maximum absolute deviation of 0.3 mm (which is on the order of ultrasound resolution). The average stiffness ratio between inclusion and surroundings was measured at approximately 5.1:1 with an absolute deviation of 0.1, from the 3 scans.

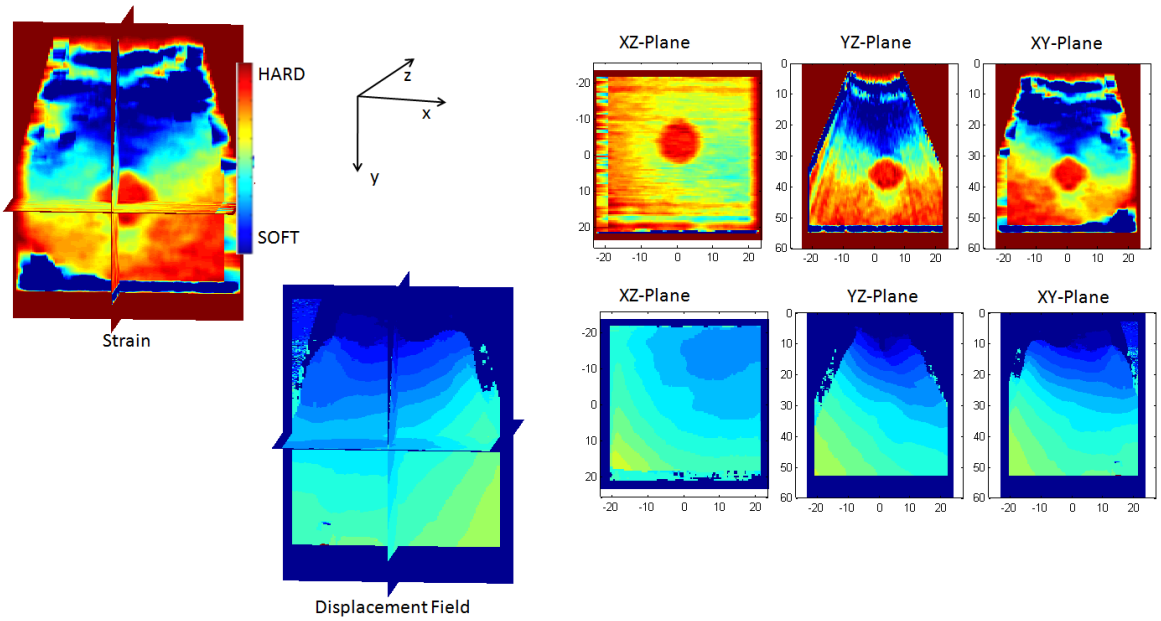


Figure 3.20(a)- (top row) Strain images and (bottom row) corresponding axial displacement fields

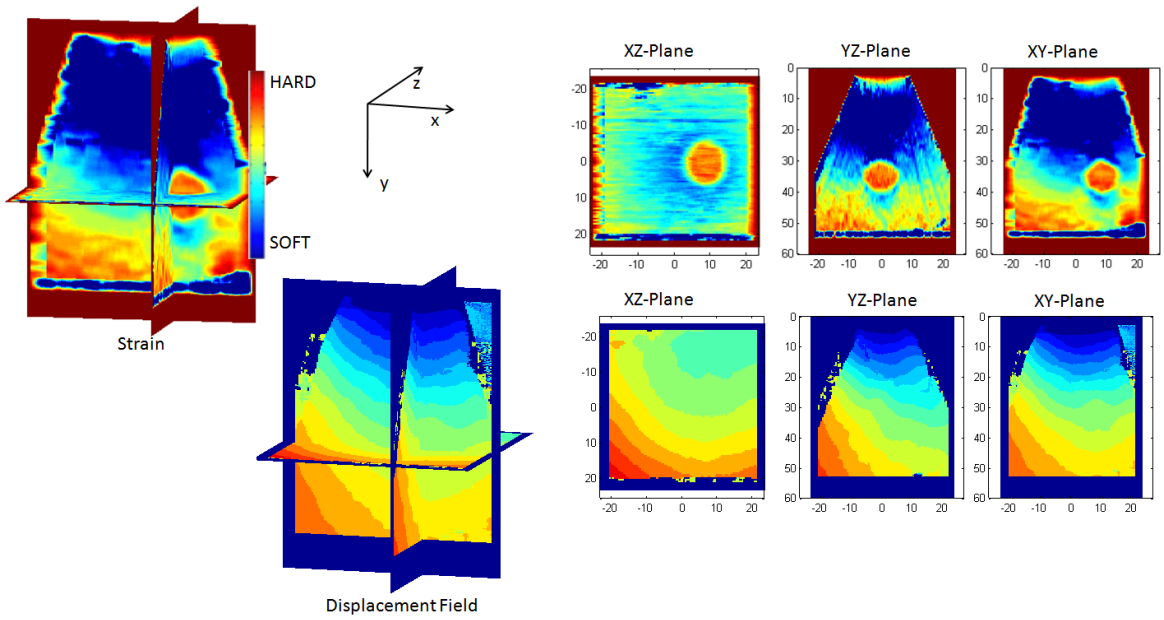
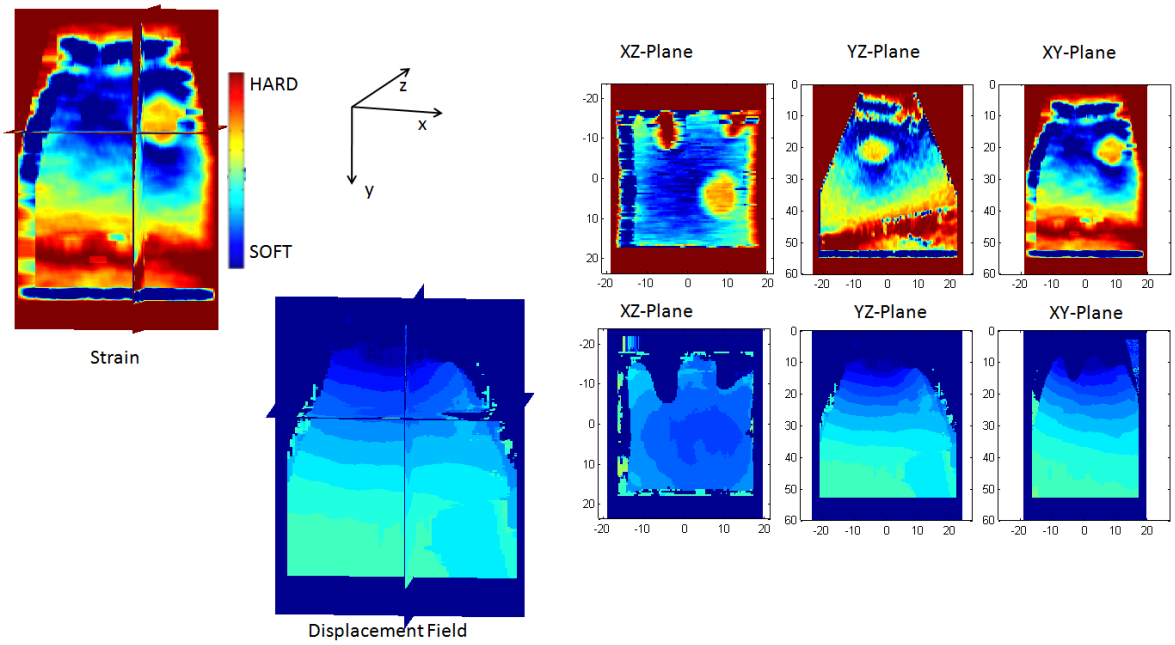


Figure 3.20(b)- Similar to the scan presented in Figure 3.19, the probe settings in this case makes use of the Harmonic Imaging Feature of the Zonare z.one machine.

A second hard inclusion in the CIRS Breast phantom was located and scanned twice using the original probe settings. Only very subtle differences in the strain and displacement fields can be observed.



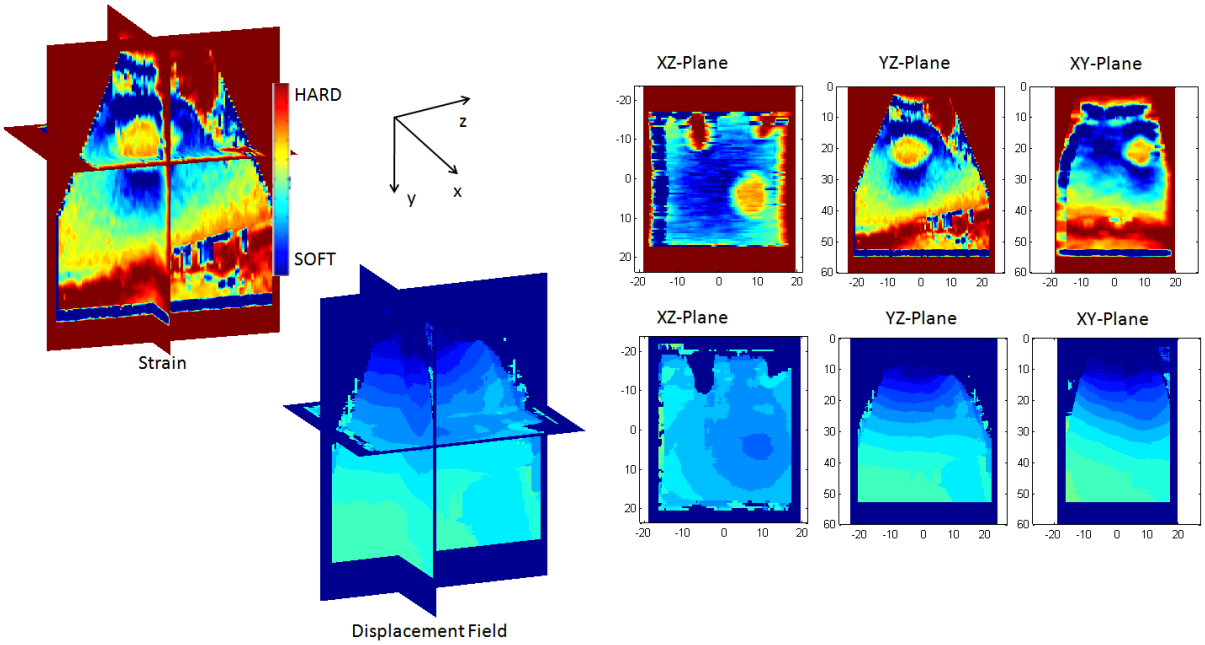


Figure 3.20(c,d)-Two scans of the same inclusion of the CIRS breast phantom under the same imaging setting

In this instance, the inclusion measures 5mm in diameter which was in agreement to both scan results. The stiffness ratio was estimated at 6:1.

The CIRS specifications does not provide exact stiffness values for its inclusions, moreover it rates the surrounding tissue as having a stiffness of 20kPa±5kP. However, the agreement from several scans and the near integer ratio values is reassuring and provides some confidence in the 3D technique in terms of its repeatability.

All the above examples are the result of good signal correlation between pre and post compression volumes and provide the same consistent result. This can be inferred by the smooth, monotonic axial displacement fields as well as the quality strain images. The displacement fields also show that the deformation is not strictly uniform over the entire volume, it is in fact more consistent with using the curvilinear C8-3 3D probe in

an assisted freehand compression/de-compression motion and using the curved probe face as the compression plate (Figure 3.17). This is a major source of variance in the results.

Clinical Data

From 35 clinical datasets, only 1 had enough signal correlation to accurately track tissue motion and obtain a reasonable strain image. In these 35 cases, no clamp was available to use and the probe was operated entirely freehand by the clinician.

A side by side comparison between the C8-3 3D probe and the 2D L10-5 probe is shown in Figure 3.21. The 2D probe has clearly better contrast and definition of the tumour boundaries.

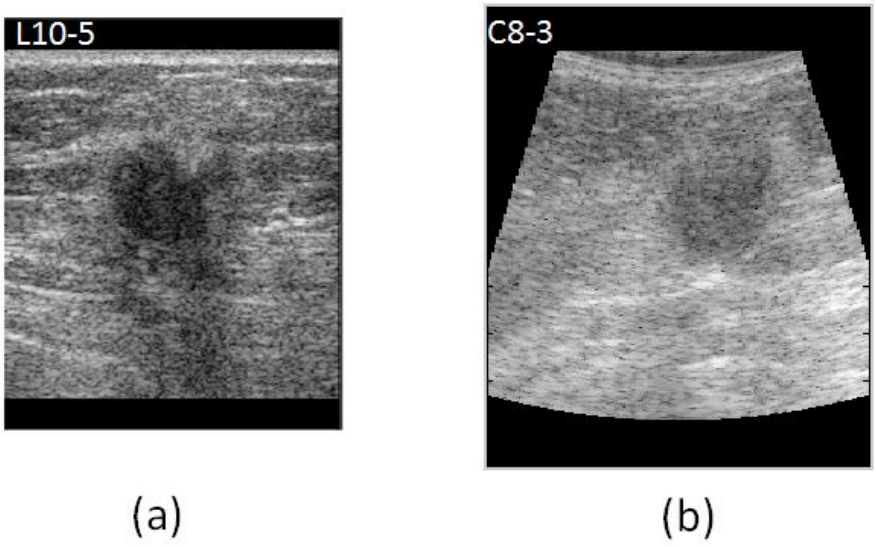


Figure 3.21-(a) tumour imaged with a 2D L10-5 probe and (b) 3D C8-3 probe from Zonare

The results from the strain algorithm are shown in Figure 3.22. The axial displacement field indicates very non-uniform deformation. The dark blue colour actually represents 0 or no displacement.

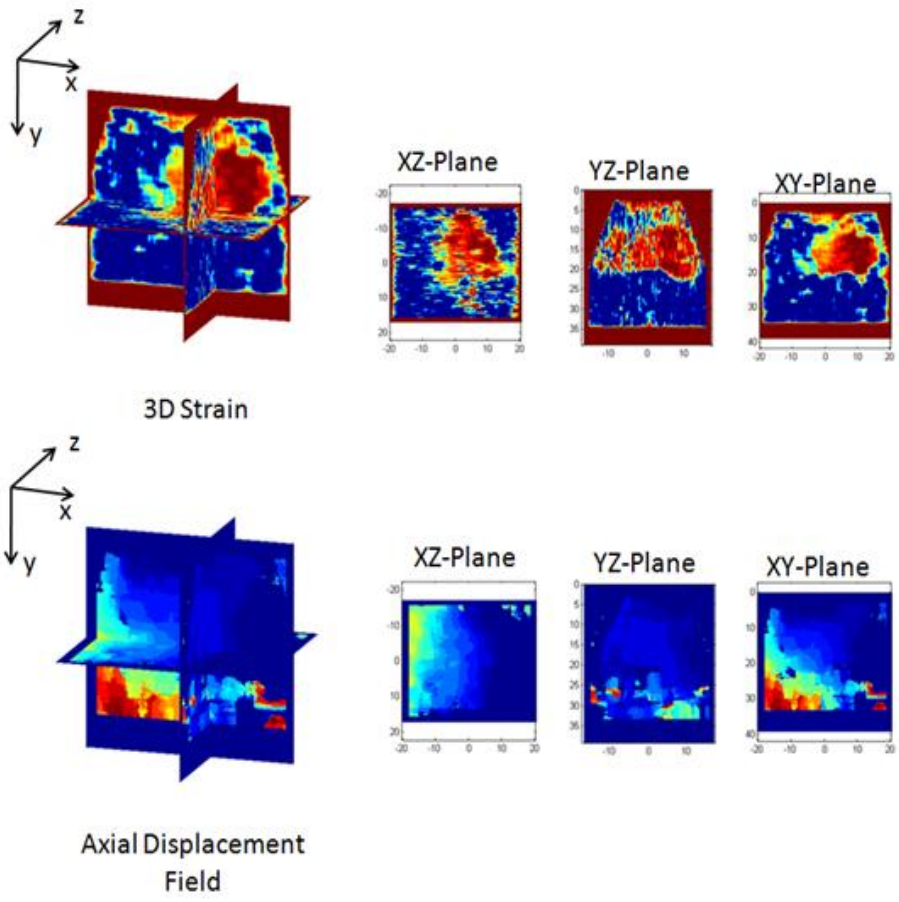


Figure 3.22-3D strain and Axial Displacement Field of a tumour

In Figure 3.23 the elastography results from the 3D data is compared to that from a 2D scan. Both shows comparable sized regions of low strain.

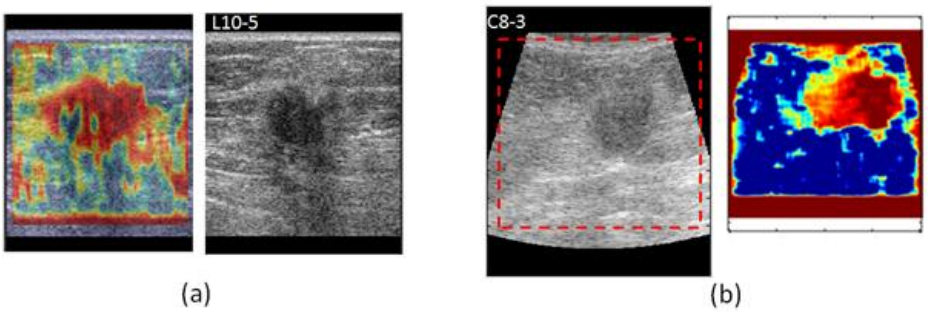


Figure 3.23-(a) Strain Image and B-mode from the L10-5 probe. (b) Strain and B-mode images from the C8-3 probe

Computation Times

The time required to produce these images was dependant on the search range parameters (Δx_{max},Δy_{max},Δz_{max}) as well as the dimensions (2D or 3D), sample rate (applied down sample factor) and image depth.

For the images of Figures 3.11-3.15, with $\Delta x=2$, Δy set for 5% average strain, $N_{FFT}=128$, and a down sample factor of 3, the average computation time in MATLAB was 2.15 seconds (0.15sec. for displacement estimation, 2sec. for the spectral shift measurement).

The computation time to generate the 3D image in Figure 3.19 was less than 3 minutes on a PC (2.83 GHz, Pentium Dual Core). The increase in dimension (from 2D to 3D) has a significant effect on computation time due to the increase in pixels/voxels in addition to a greater search range.

3.6 Discussion

3.6.1 1D Simulations

Figures 3.6-3.8 clearly demonstrate the trade-off between precision and accuracy when tracking motion. A large window produces overly smooth results with a small variance

whereas the smaller window, though very precise, produces an output error with much higher variance. There clearly exists an optimum window size based on the signal content and features. How strain estimation methods deal with this fact is crucial to their success in practical medical applications where such a priori knowledge may be limited and the optimal window size unknown.

Figure 3.9 provides encouraging motivation for direct frequency based methods. The response of the spectral based method indicates that larger windows can be used to track tissue motion without detriment to the strain estimate. The explanation is straightforward when considering that the method measures strain directly, so errors in the displacement estimates do not propagate as they would in taking the gradient. Moreover, slight imprecision in motion tracking has negligible effects on the resulting signal spectra. Consequently, the complicated methods presented in Chapter 2 for displacement estimate error correction and interpolation can be avoided; by choosing a larger window for block matching (e.g.~5mm) accurate results can be obtained more consistently without worry over significant loss in precision in the strain estimates.

3.6.2 2D and 3D Experiments

Results from Figure 3.11-3.15 further support the conclusion that good strain estimation can be obtained while maintaining insensitivity to displacement tracking precision error. Furthermore, Figure 3.15 and Figure 3.16 demonstrate the spectral shift method far outperforms gradient techniques when signals are down sampled.

Figure 3.19 and the other 3D data sets demonstrate the algorithm's ability to function in 3 dimensions. This is not surprising since 2D and 3D algorithms, as stated earlier in Chapter 2, are simply extension of a simple 1D technique.

In both 2D and 3D experiments, the difficulty of freehand scanning is apparent. The probe face and the inevitable variation in applied stress creates tissue motion that is difficult to reproduce with fidelity. Nonetheless, hard inclusions are still readily visible and the contrast (ratio of strain between inclusion and its surroundings) remains consistent over many scans; meaning that image anomalies and noise may be mitigated by interpreting or averaging results over several acquisitions.

Overall, the 3D probe setup for freehand scanning in clinic was not capable of creating reliable 3D data acquisitions. Moreover, the probe's resolution made it difficult for clinicians to even locate tumours that were initially imaged clearly using the 2D probe in B-mode. Future development of this technique will require a more robust assisted freehand scanning protocol, like that used in the 3D phantom experiments, and ideally a built for purpose 3D probe.

3.7 Conclusion

An efficient block matching scheme was derived making use of integral images\volumes to obtain maximum window overlap with minimum computational redundancy. In combination with an efficient implementation of spectral shift estimation, the result is a robust system for strain estimation.

With maximum window overlap, strain estimation resolution was limited only by FFT window size and of course the ultrasound resolution of the probe (PSF).

Moreover, results were obtained using fixed parameters (e.g. window size, FFT size) for all cases thus demonstrating little need for tuning the algorithm. The algorithm also easily lends itself to parallel processing and could (in the 2D case at least) be made to run in real time.

Though variation in freehand results is inevitable, the relative ratio of strain between inclusion and its surrounding was consistent. This leads to another aspect of breast cancer imaging which is every bit as important as strain and displacement estimation algorithms; the consistency in the image output display. Colour mapping, dynamic range and contrast are all topics which will be examined in the next chapter.

Chapter 4
Data Quality Assessment and Display

4.1 Introduction

This chapter concerns itself with two tasks; assessing the quality of the strain estimate (Sect. 4.2) and producing consistency in displayed images with as much contrast as possible (Sect. 4.3). Solutions to these problems are crucial for the data analysis in Chapter 6 and Chapter 7.

Strain estimation error can be due to out-of-plane motion and signal attenuation/ posterior shadowing leading to signal decorrelation. The result is poor displacement estimates which ultimately lead to poor strain estimates. Methods previously mentioned like Dynamic Programming and the LSGE use regularization or spatial smoothing to filter out the noisy output of the displacement field, producing plausible strain estimates despite the signal loss. However, these methods obscure underlying information which may be helpful; work in [7,12,119] for instance has shown that signal decorrelation due to out-of-plane motion or slip can be a useful measure of tissue mobility. Consequently, in this project it was deemed prudent to detect strain error, rather than filter it out or compensate, to allow for subsequent interpretation of its cause.

4.2 Quality Metrics

A simple measure of signal decorrelation is, not surprisingly, evaluating a correlation metric between paired signal content from pre and post compression images [7]. This is something computed during motion tracking/spectral shift calculations, and so comes at

no extra cost in terms of computation. Figure 4.1 shows the scans of an olive phantom (a de-pitted olive embedded in gelatine). The olive was selected because it contains an air pocket in its core producing a noticeable shadow (Figure 4.1(a)). The meat of the olive provides a relatively homogeneous material to mimic a hard inclusion once embedded in gelatine.

Note that an ideal axial displacement field should be monotonically increasing with depth. Thus, it is easy to spot from Figure 4.1(b) and (c) where strain error is likely to have occurred. The shadow region corresponds well with the noisy displacement fields and cross correlation image. These all help explain the apparent high strain region in Figure 4.1(d).

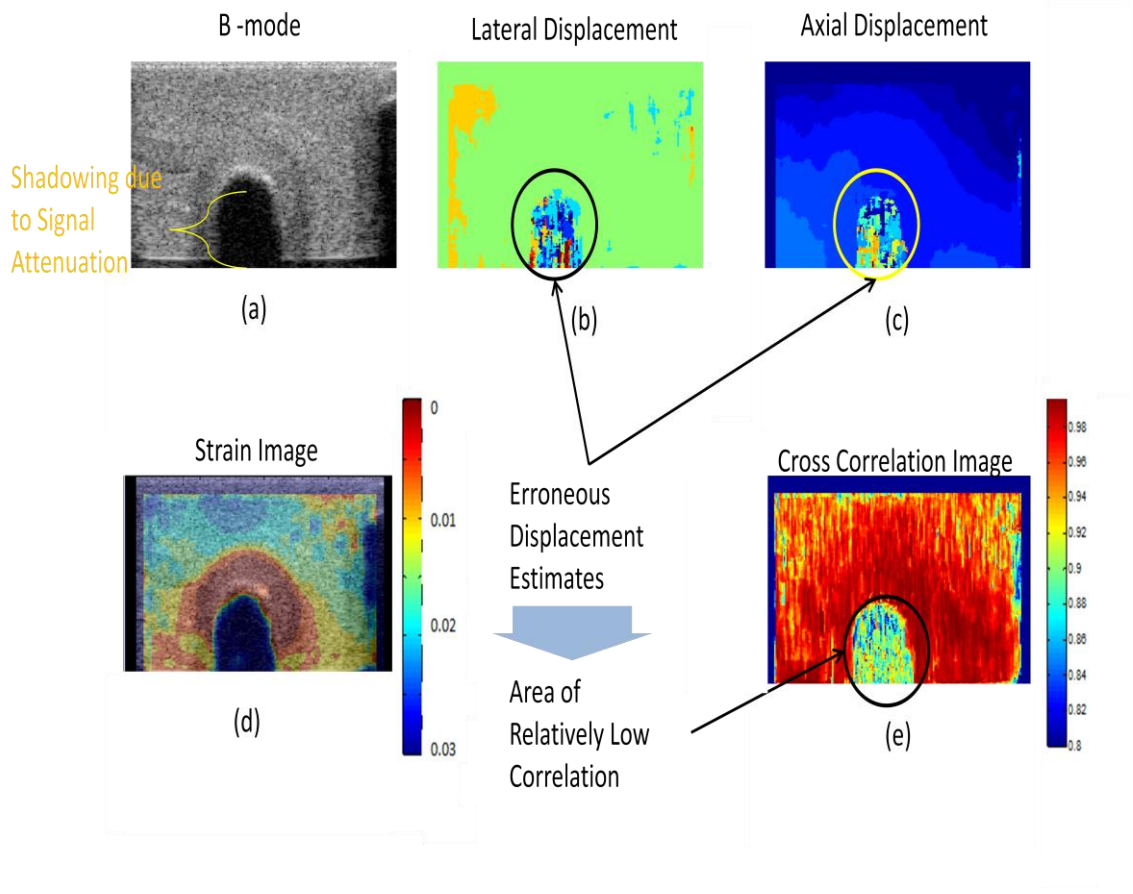


Figure 4.1-The Effects of Posterior Shadowing on Signal Correlation, Strain and Displacement Fields

It is important to note that even under ideal conditions, signal decorrelation will inevitably occur due to tissue deformation. One attempt to model this relationship [120] suggests that the normalised cross correlation, ***r***, between pre and post compression signals can be related to strain, ***ε***, as

$$\varepsilon = 1 - r \tag{4.1}$$

$$or \qquad r = 1 - \varepsilon = -\varepsilon + 1 \qquad (see\ Eq(4.2))$$

This was found to hold only for small strains (<2%) and experiments were done only on simulated data. However, the model does give some insight; namely signal correlation decreases with increasing strain. What happens for larger strains depends highly on the nature of the data (clinical, phantom or simulated). The linearity of tissue in terms of strain has already been discussed in Chapter 2; it was decided that using a linear model here would provide a good compromise between simplicity and accuracy. Nonetheless, a more robust model needed to be devised to help classify and exclude outliers.

In Figure 4.2, a correlation versus strain scatter plot was produced for the olive phantom. A linear curve fit was applied to the data, with the constraint that the point *(ε,r)=(0,1)* should be included.

$$r = m\varepsilon + 1 \tag{4.2}$$

This simple modification of *Eq(4.1)* using the parameter ***m***, allows for the linear model to better adapt to the data at hand by taking into account the dynamic range of the points themselves. In Figure 4.2(a), note that the variance in the points about the trend line, derived from *Eq(4.2)*, increases with strain. This suggests that estimates at higher strain are less trustworthy. At this point it becomes necessary to define what an outlier is. In this research, it was chosen empirically to include all points within +-5% of the trend line. However, to account for the greater uncertainty in the measurement at higher

strains, this threshold was dropped off exponentially. The basic idea is that points closer to the curve fit are deemed more reliable, and at higher strains this constraint needs to take even more precedent. A binary mask was generated based on these points (Figure 4.2(b)); it clearly identifies the region with low signal decorrelation due to the posterior shadowing.

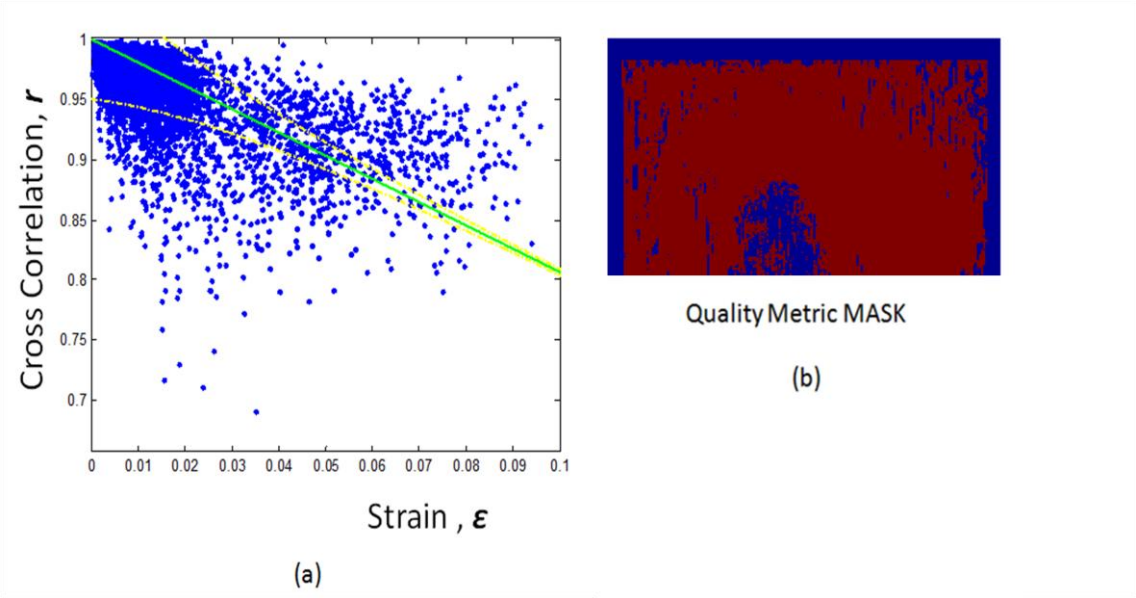


Figure 4.2- Eliminating Outlying Strain Data Points: (a) Strain vs CC scatter plot with curve fit and outlier region boundaries defined. (b) Resulting quality metric mask (red= good data, blue =poor data). Mask corresponds well to regions of attenuation and also where displacement (lateral is highest)

It was of interest to find out what would happen if these parameters were increased/decreased in order to explore the sensitivity of the proposed method. In Figure 4.3 the range of acceptable strain values and the rate at which the threshold was tightened at larger strains was adjusted. As expected, parameters that limited the number of eligible pixels consequently produced more masked pixels (Figure 4.3(a) and (c)). Parameters that were more all-encompassing resulted in less masked out values (Figure 4.3(b) and (d)). In all cases, the hypoechoic attenuated region is masked out. Additional masked out regions tend to correspond to areas of high lateral and/or axial displacement

and higher strain. Moreover, these regions are gradually incorporated (or left out) of the masked region as parameters are adjusted.

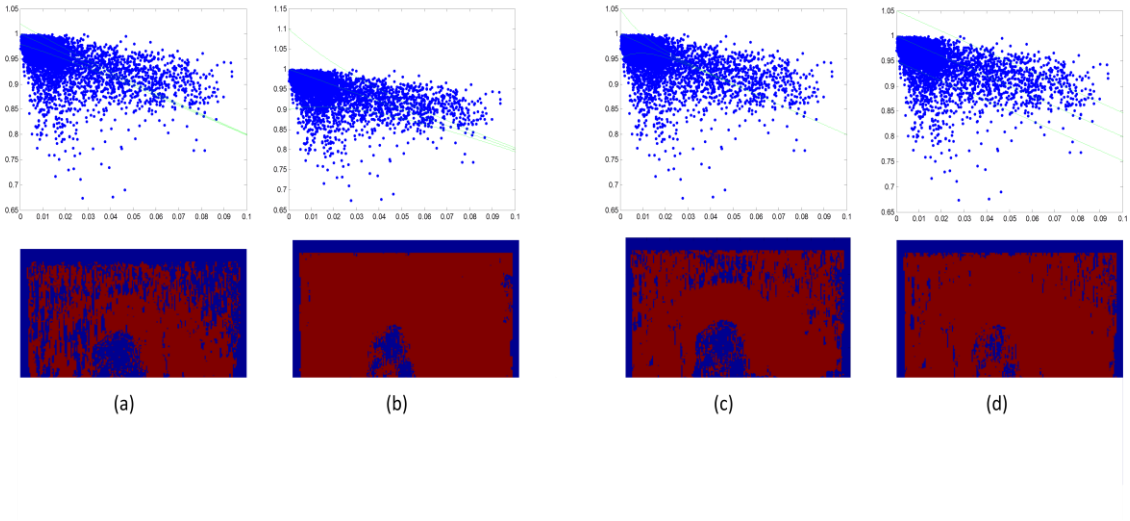


Figure 4.3- (a) and (b) Effects of changing initial range (a)± 2% and (b) ± 10%. Keeping range at ± 5% and adjusting time constant on exponential decay for rapid decay (c) and (d) a larger time constant for a more gradual decay.

Further studies were conducted on other phantoms. In order to simulate an ideal case with no expected strain estimate error, a simple homogeneous phantom was constructed to have a well-behaved displacement field and strain image (Figure 4.4). The ***ε-r*** plot shows most estimates has a high correlation value. Consequently, the mask encompasses the vast majority of the original image.

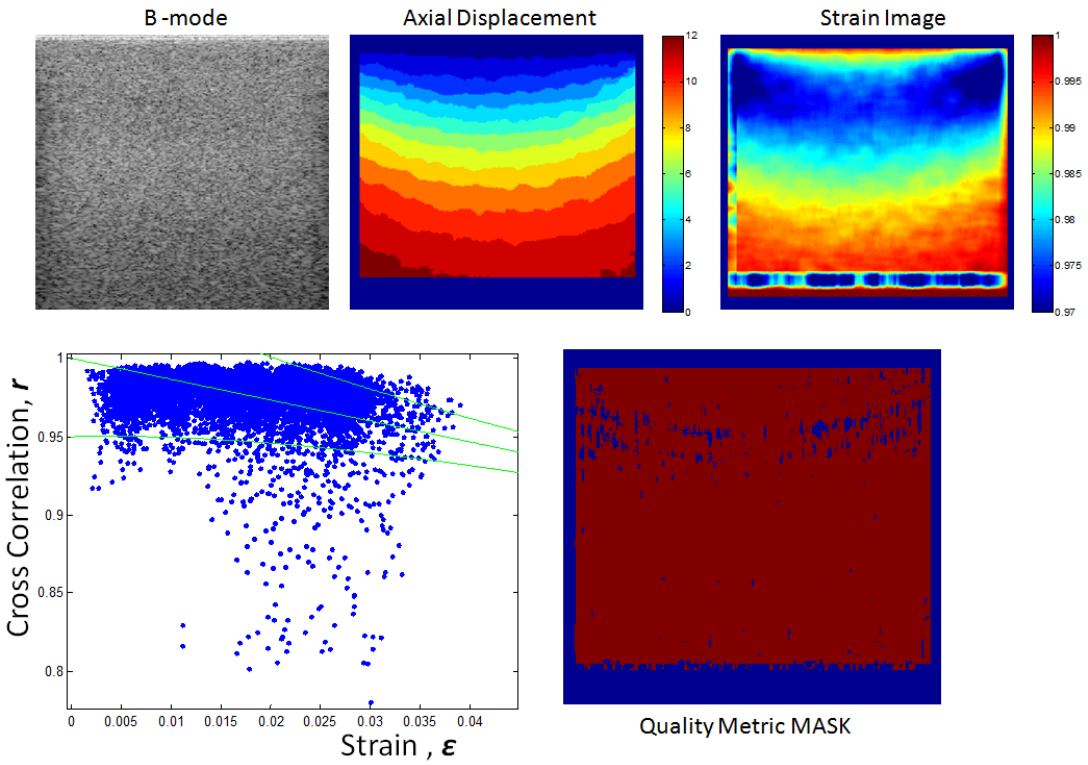


Figure 4.4-The Effects of Signal Decorrelation in an Ideal Homogeneous Phantom

In another example, the same analysis is performed on the phantom from Chapter 3. Two concentrations of points are present in the ***ε-r*** plot in Figure 4.5; a small one at 1% strain and a larger one centred at 3% strain. This is consistent with the fact that the hard circular inclusion was designed to be roughly 3 times stiffer than its surroundings. Moreover, the spread or variance of the points at higher strains is once again greater than at lower strains. Signal decorrelation is greatest directly above the circular inclusion (where strain is at its greatest) and around the boundaries of the inclusion, possibly due to slip at the interface between two different types of gelatine.

Both examples (Figures 4.4 and 4.5) highlight a common artefact with gelatine phantoms; as the gel sets it tends to stratify in horizontal layer. These layers are not fully bonded and can slip laterally under compression leading to signal decorrelation.

These layers are clearly visible in the two phantom image masked produced by the proposed algorithm.

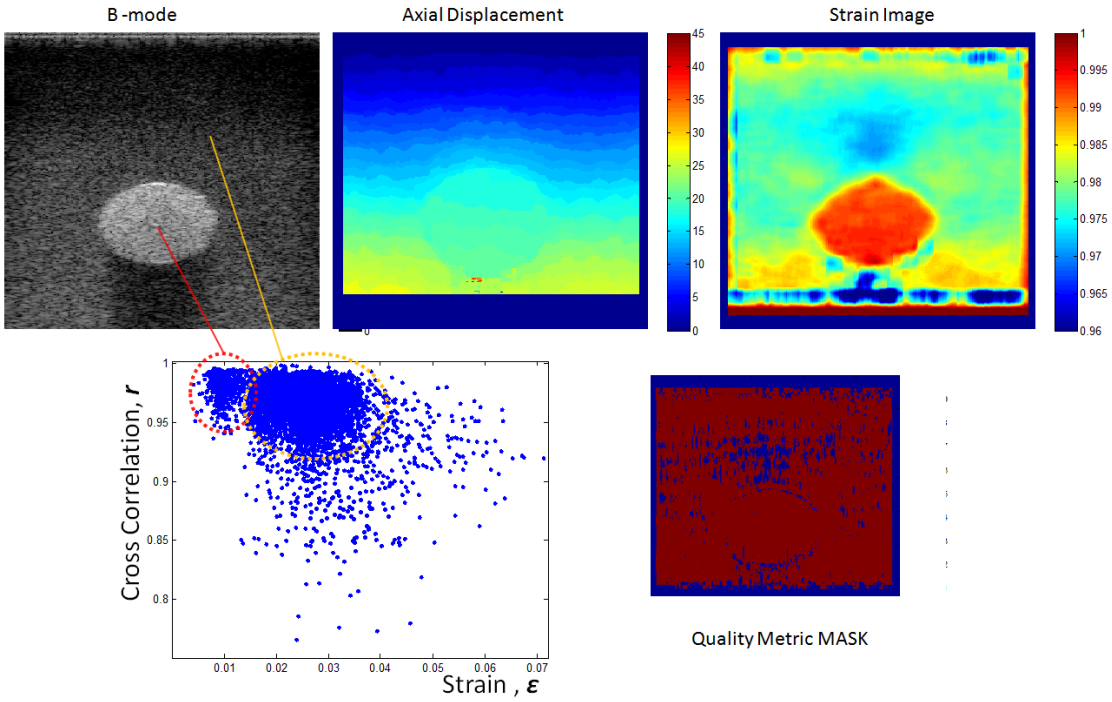


Figure 4.5-Signal Decorrelation due to strain in a phantom with a circular shaped hard inclusion

In most clinical data obtained, the bottom portion of the ultrasound image (as indicated in Figure 4.6) typically exhibited very low signal correlation. The primary cause, aside from being subject to greater signal attenuation and more prone to sources of noise like refraction at greater depths, is small changes in the angle of the probe's orientation relative to the elevational plane during the compression-decompression stage that produces greater out of plane/elevational motion. Indeed, simply holding the probe steady over the ROI produced a speckle pattern which flickered similar to the static observed on a de-tuned analogue television. It was expected that the quality metric algorithm would identify these regions as having poor signal correlation as indicated in the mask produced in Figure 4.6.

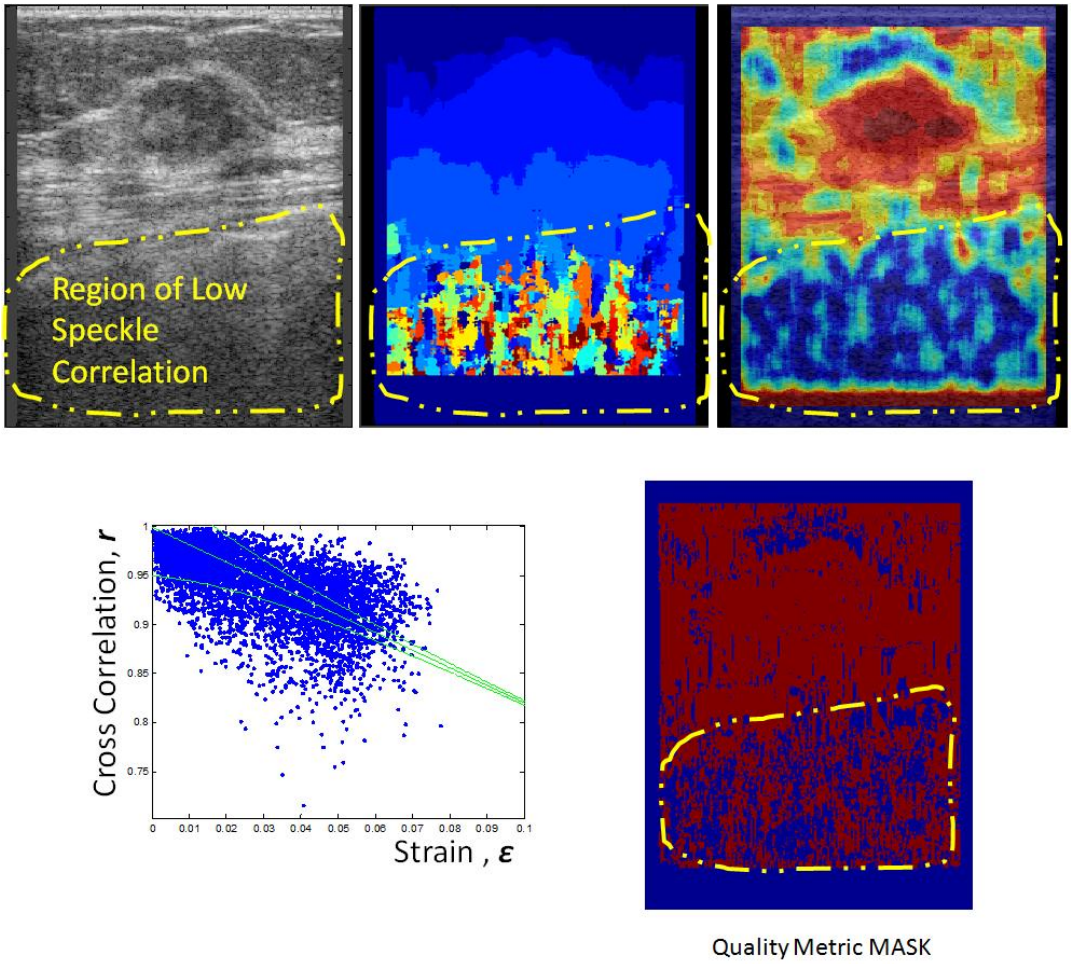


Figure 4.6-Signal Decorrelation due to signal attenuation at greater depths in typical clinical data

4.3 Normalization and Display

A straightforward and accepted way to normalise strain images, taken under different conditions with various strain distributions, is to use the average strain in the image as a normalisation/reference point [7,121]. The previous section proposed a tool for excluding outliers which also helps produce a more accurate average strain calculation.

Controlling the dynamic range of the strain values and producing a consistent colour mapping is another challenge. In Figure 4.7 the strain image for a DCIS is displayed using the MATLAB command 'imagesc' which has the option to set upper and lower

bounds on the dynamic range of a signal. Min and max values are mapped to red and blue respectively, from the 'jet' colourmap. The min value in a strain image can reasonably be set to 0. However the max cannot simply be set to the maximum strain value in the image; a single outlying point could throw off the entire range. Selecting some reasonable max value is one solution. In Figure 4.7, max strain is set to 5,4,3,2 and 1% , displayed from left to right. A serious problem is demonstrated; as the dynamic range changes so too does the tumour's apparent size! Since one goal is to use elastography for tumour segmentation, this is extremely problematic.

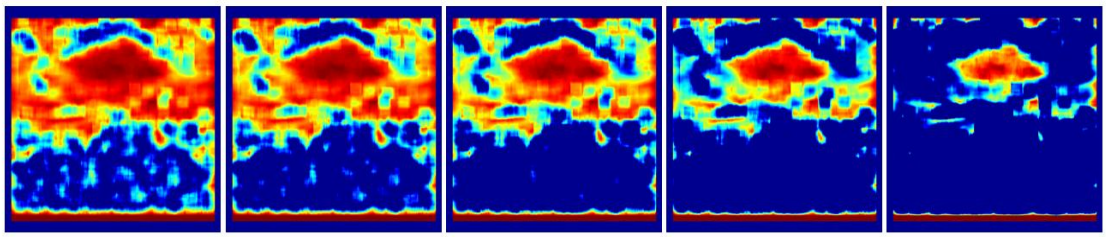


Figure 4.7-The Effects of Dynamic Range on the colour map and display of strain data. Left to right: a tumour's strain images using 5,4,3,2 and 1% max strain cut-off respectively.

A more consistent means of selecting the dynamic range needed to be developed. For this, histogram equalization (HEQ) was employed. HEQ is a very well established image processing technique [122-125]. It works by attempting to redistribute the pixel values of an image evenly across the entire dynamic range. It gives preference to pixels with more frequent intensities, generally increasing local contrast at the expense of reduced contrast for less frequent values. A better understanding can be gained from the HEQ formulae, *Eq(4.3-4.5).*

Assume an image with ***n*** pixels. A cumulative distribution function (***cdf***) is generated by integrating over the proportion of pixels ***p***, with pixel values ***i***. Pixels with high

frequency will produce a large increase in the *cdf*, pixels in a sparse region of the dynamic range will lead to a flattened *cdf*. The final image transformation ***h***, is described by *Eq(4.5)*. Where the slope of the *cdf* is greater than 1, ***h*** will produce an expansion of the data (increase in local contrast). Where the slope is less than1, the data range is compressed and contrast is lost.

The value ***L*** represents the number of pixel values in the colour map. For a grayscale colour map with pixel values ranging from [0 255], *L=256*. The transformation is portrayed graphically in Figure 4.8.

$$cdf(i) = \sum_{j=0}^{i} p(j) \tag{4.3}$$

$$p(i) = \frac{n_i}{n}, \quad 0 \le i < L \tag{4.4}$$

$$h(v) = round\left(\frac{cdf(v) - cdf_{min}}{n - cdf_{mn}} \cdot (L-1)\right) \tag{4.5}$$

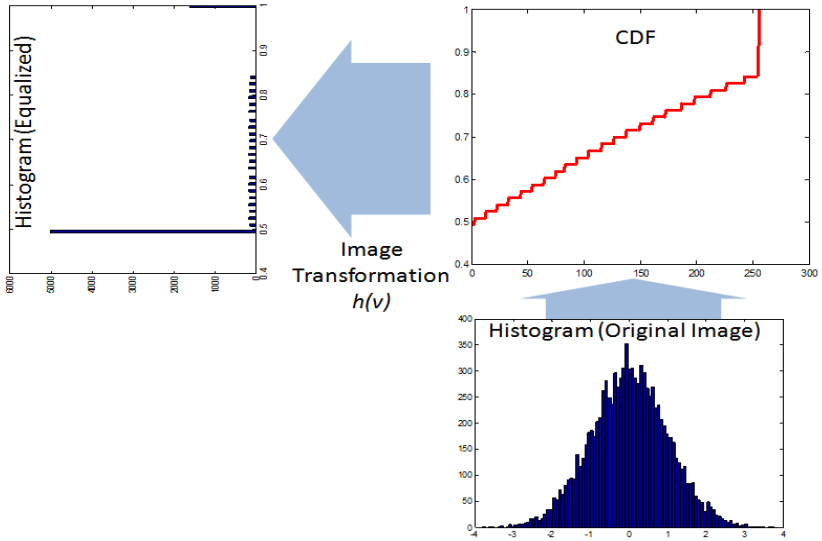


Figure 4.8-Histogram Equalization: A Visual Depicting of the transformation h(v) from Eq.4.5

HEQ has several benefits in displaying strain data:

- One-off outliers will not have serious consequences on image contrast; frequent pixel values get mapped to an expanded range; increasing local contrast. Less frequent outliers get compressed. A particular pixel value needs to be prevalent to have an impact. This provides an elegant solution to the problem of choosing a max value for strain.
- cdf's increase monotonicaly; preserving the relationship between higher and lower strain values.
- Provides good contrast where it is desired; around the tumour and surrounding regions which generally make up the bulk of the image ROI and thus benefit the most from the contrast enhancement.

Figure 4.9 shows the *cdf* of the DCIS already depicted in Figure 4.7. The image was first converted to a pseudo strain image (*1-ε*) and subsequently remapped and quantized to 0-255. We can see from the cdf, the maximum strain was ~9% (corresponding to pixel value 238).

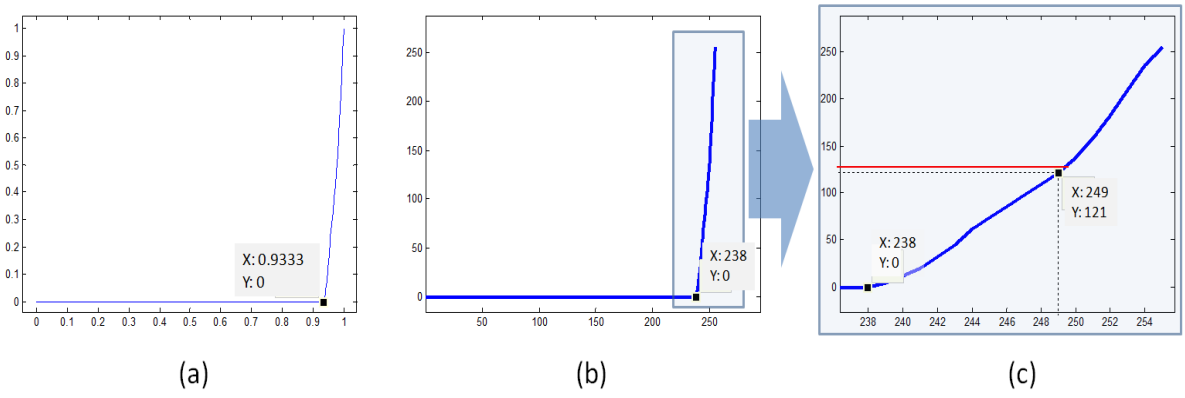


Figure 4.9-The cumulative distribution function (cdf) for an image containing a DCIS. (a) and (b) are the same cdf represented in terms of strain and pixel value respectively. (c) is a zoomed-in image of the shade region shown in (b). Average strain of the image was mapped to an initial pixel value of 249; to be remapped to 121 after the HEQ transformation

The next step is to apply the transformation. Figure 4.10 shows a typical result; an immediate and significant increase in contrast is apparent.

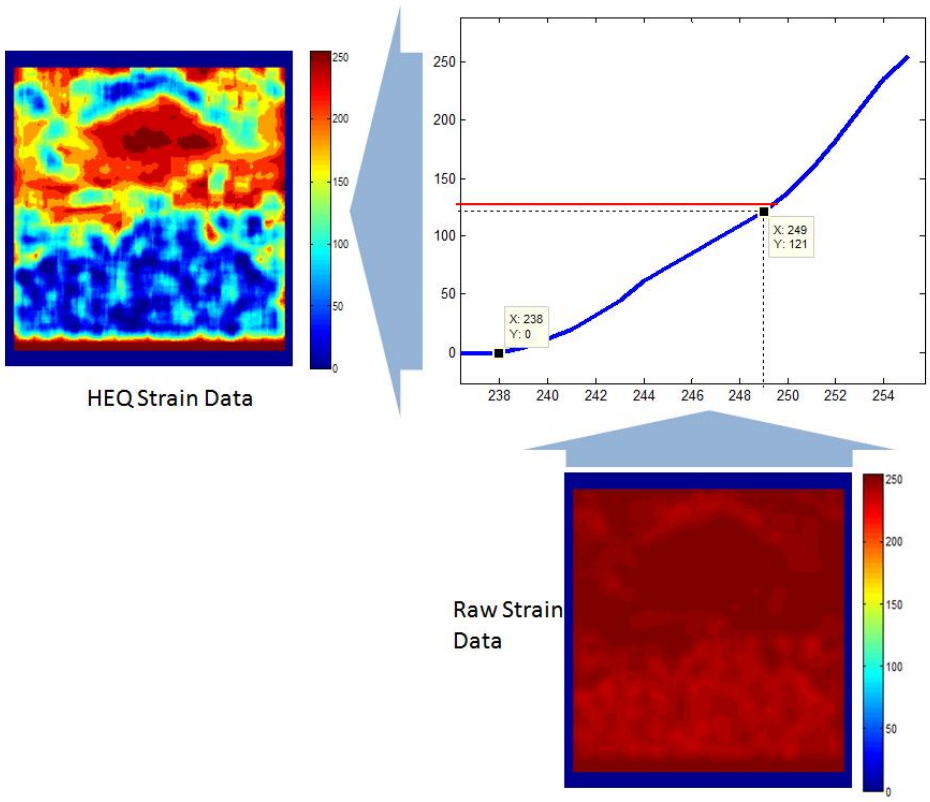


Figure 4.10-HEQ applied to raw strain data. The raw strain data is displayed using min and max strain values set to 0 and 100% respectively resulting in an inefficient use of the colour map.

It was then decided to use the average strain of the image to provide a consistent reference point in the colour mapping. This was done by setting the average strain to a pixel value of 127 (a shade of Green in the 'jet' colourmap) and forcing all pixels of higher value to spread linearly from 127-255, and all those lower values from 0-127. From Figure 4.11, it is evident that this only produces a slight change from the initial

HEQ image; however, it does ensure that the average strain is indeed the same colour across all images produced in this way.

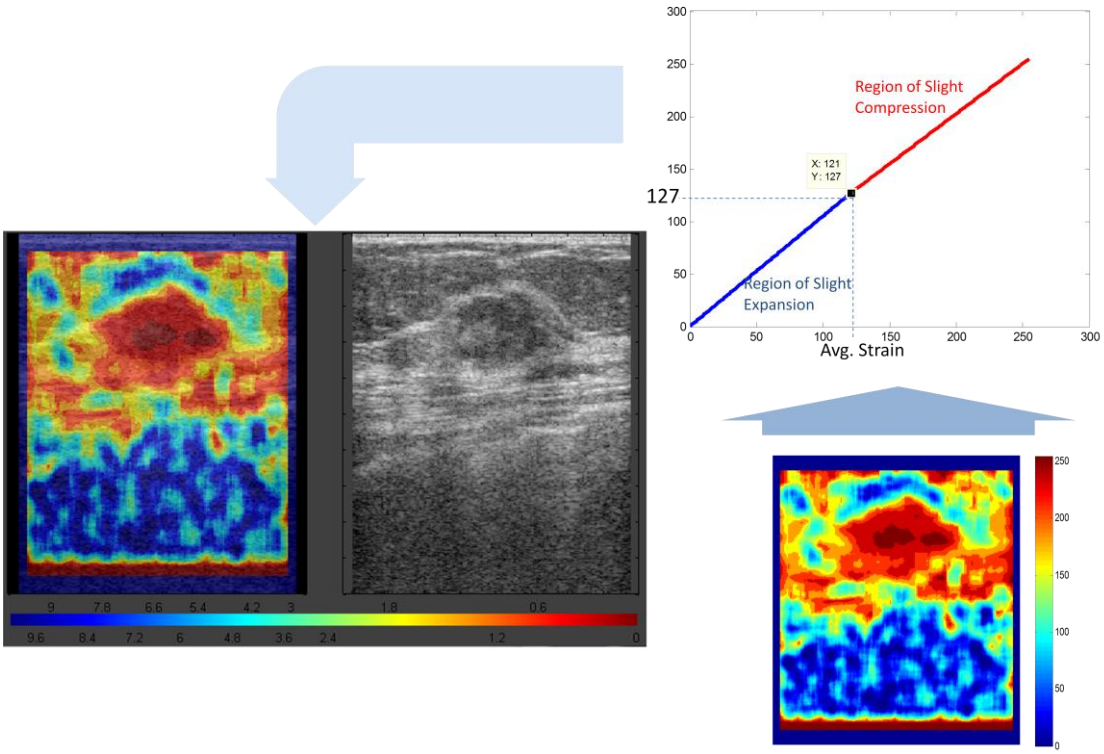


Figure 4.11-Final Stage of Image Colour Mapping: Set the average strain value to pixel values 127 (green)

HEQ works ideally for continuous data; the more discrete the distribution of strain data values, the more discrete the colour mapping. In the case of some phantom data, this has the effect of creating a somewhat blotchy image (Figure 4.12). Fortunately, clinical data contains a widely distributed set of strain values.

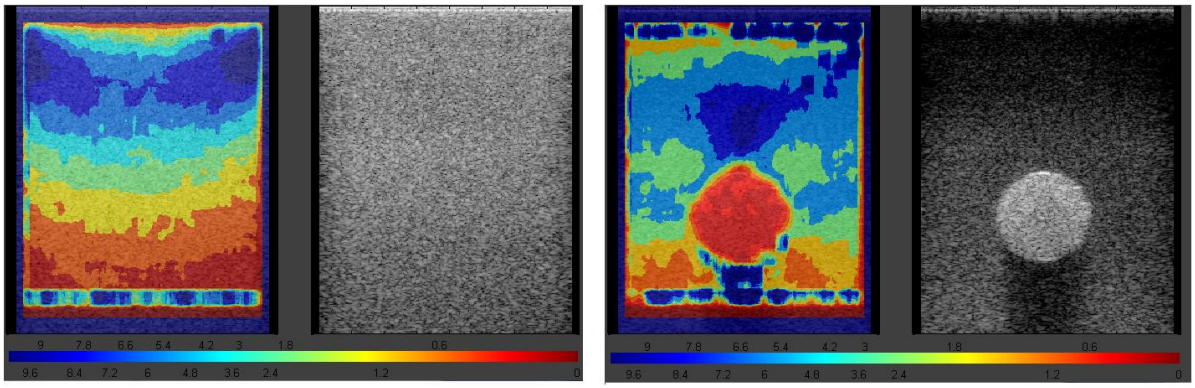


Figure 4.12-Effects of HEQ on Phantom Data: A discrete distribution of strain values can result in a more blotched look to the final colour map

4.4 Conclusion

In this chapter, a method for identifying outlying strain data was presented making use of a standard relationship between strain and signal decorrelation. A simple modification in *Eq(4.2)* allowed for the method to adapt to the individual strain image rather than rely on a gross generalization already used in *Eq(4.1)*. A classic image processing technique, histogram equalization, was also used to find an elegant solution to the problem of setting dynamic ranges on strain data for colour mapping purposes. With the end of this chapter, a now more complete strain imaging system has been presented. With a more consistent colour mapping scheme, elastograms can be used to produce a more reliable measure of tumour size (Chapter 6) and track tumour response to chemotherapy over time (Chapter 7).

In Chapter 5, a method is proposed for measuring the viscoelastic properties of tissue. It makes use of information derived from a series of strain measurements acquired in the space of seconds to obtain additional information about the viscosity of tissue.

Chapter 5
Hybrid Freehand Imaging of Visco-Elasticity (HYFIVE)

5.1 Introduction

This chapter describes a system for *hy*brid *f*reehand *i*maging of *v*isco*e*lasticity (HYFIVE). So far in this thesis, a complete method for quasi-static elastography has been described. Fundamentally, this involved measuring the deformation of tissue by comparing 2 images (pre and post compression). However, the biomechanics of tissue deformation is far more complex than the quasi-static model allows for. Though it will be demonstrated in the next two chapters that simple strain images are indeed sufficient for breast cancer therapy imaging, in this chapter's experiment an investigation into the non linear properties of tissue is carried out.

A distinctive attribute of ultrasound (US) imaging is a high frame rate compared to other medical imaging modalities. Various techniques in ultrasound elastography have been developed to exploit this feature in order to determine parameters which may help differentiate soft tissue types and characterize breast lesions. In [69], cyclical compression was used to map out a spatially varying hysteresis loop; its normalized area was used to generate a parametric image. Another method [126-127] measured the *creep* resistance of tissue; creep is defined by the strain vs. time response of a material to a sudden applied step force. It is this technique which forms the starting point for this chapter's work.

Initial findings suggest that viscosity and a time constant associated with tissue creep may provide additional information which may pertain to fluid diffusion through porous material [126,128]. This has significance in breast cancer imaging as tumours generally exhibit increased angiogenesis, in fact it is crucial for tumour growth and metastasis [60-64]. Because of their uncontrolled development, blood vessel formation in tumours is haphazard and they often leak [129]; see Chapter 2: Dynamic MRI and FDG-PET . Still, other imaging techniques like Diffusion MRI bases itself on the fact that densely packed tumour cells may impede the flow of water and other fluids present in the tissue [130]. Clearly, the type of tumour plays an important role as they appear to have a variety of responses. Based on these facts, it is of particular interest to see what if any distinctive viscoelastic properties can be observed in early breast cancer.

Present ultrasound techniques for creep response measurement require long time sequences of data (up to 2min) and extra hardware to monitor applied stresses [127]. The aim in developing the HYFIVE system was to alleviate the constraints on expensive hardware and demonstrate that only a short time sequence (< 2s in fact) of data is needed for imaging.

Section 5.2 describes the methodology; namely a unique piece of hardware (the probe canister device) used for generating the appropriate external stresses on the tissue under examination. It also provides a full derivation of the model and formulae used to describe the creep response. Results from experimental scans of a phantom and 4 clinical datasets are presented in Sect. 5.3. A discussion of the results and conclusion about the HYFIVE system are presented in Sect. 5.4 and Sect. 5.5 respectively.

5.2 Materials and Methods

5.2.1 Hardware

The probe canister device design is depicted in Figure 5.1. The US probe is secured firmly in the canister by specially designed caps at the top and bottom. A weighted ring or hoop (500g) is free to slide up and down the outside canister wall which has tracks cut into it. Track bolts keep the motion of the ring vertical but still allow the clinician holding the apparatus via the ring to manipulate the probe side to side as well as to rotate it about the vertical axis. Once the probe is in position, the clinician simply lifts/slides the ring up to produce what can be approximated as a unit step-off force. The probe remains set above the region of interest free to acquire images at a pre-selected frame rate thus capturing the creep response of the underlying tissue (see Figure 5.2).

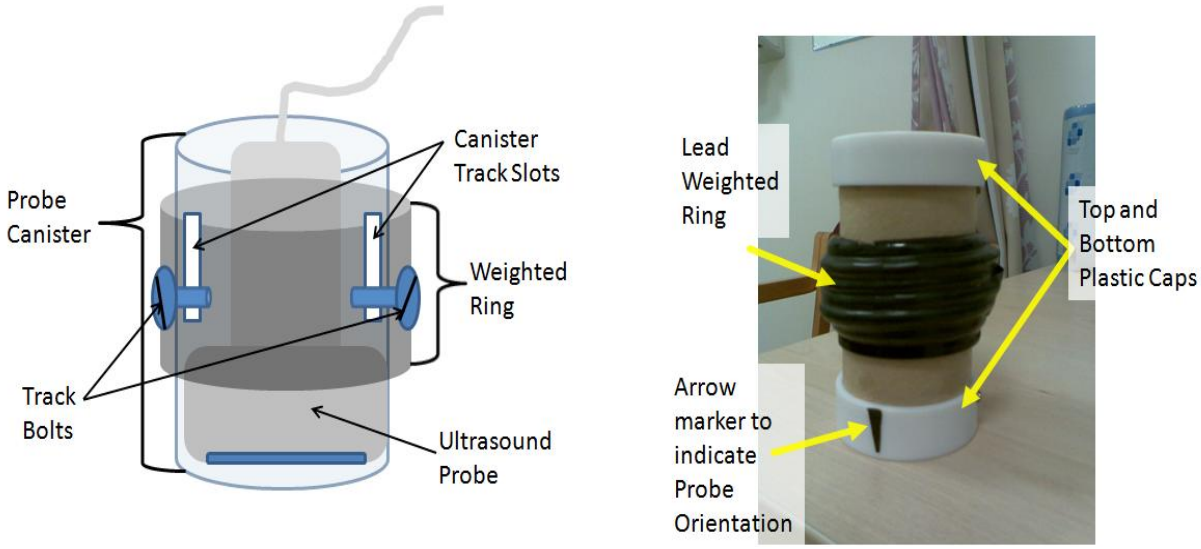


Figure 5.1- Diagram and photo of US probe canister device

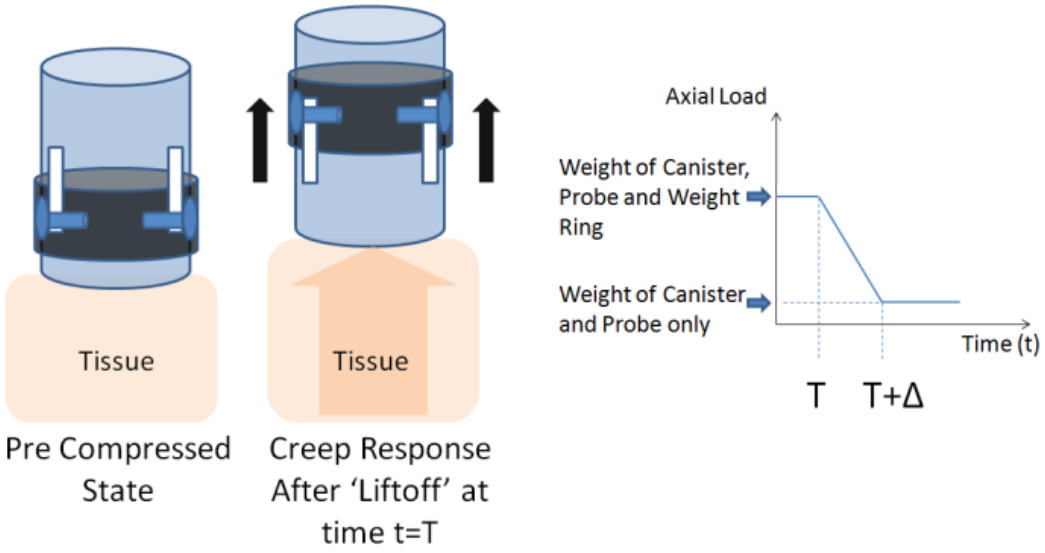


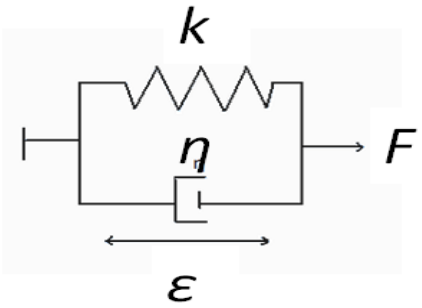
Figure 5.2-Probe Canister in Operation and Resulting Applied Force

Scanning Setup

Scanning of patients was conducted in clinic using the Zonare z.one L10-5 linear probe probe. The probe centre frequency was set to 8.5 MHz at a frame rate of 13 fps. Patients were asked to lie on their backs on an elevated examination table (as in any standard ultrasound scan). The probe was held freehand (unsupported) by the clinician in the manner described in the previous section. The probe canister device relies on gravity to function properly. Therefore, as much as possible, it was attempted to keep the probe as vertical as possible while still keeping it normal to the scanning surface; this was accomplished by asking the patient to rotate slightly on their side (if necessary). Once the region of interest was located in the probes imaging plane, the 'lift-off' of the probe weighted ring would occur and the ultrasound image sequence would be saved. If drastic out-of-plane motion occurred the experiment would be repeated up to 2 more times or until a 'good' (little perceivable out-of-plane motion) set of data was obtained.

5.2.2 Tissue Model, Derivation & Curve Fitting

To represent the tissue response, a simple first order Kelvin-Voigt model was assumed [144-145]. Conventional elastography models tissue as an ideal spring, with spring constant $\boldsymbol{k}$ and strain $\boldsymbol{\varepsilon}$. The addition of the dashpot introduces viscosity $\boldsymbol{\eta}$ into the equation. It has been shown [126] that the time constant $\boldsymbol{\tau=\eta/k}$ can provide a useful tissue characterization parameter as well.



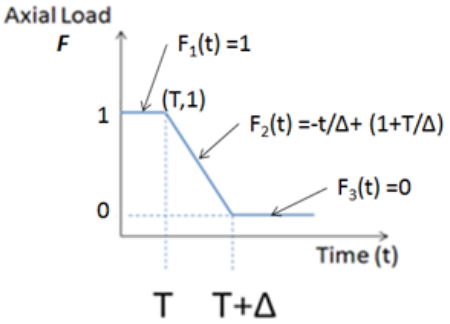
$$F = \eta \dot{\varepsilon} + k\varepsilon$$

Figure 5.3-The Kelvin-Voigt Model and governing equation

Strictly speaking, the applied force should be treated as a ramp function. Given a ramp interval Δ defined in Figure 5.2, it can be shown that for $T>>0$, $t'=t-T$, and taking the overall change in force to be unitary, then for the 1st order Kelvin-Voigt model the resulting strain/creep response can be modeled as

$$\varepsilon(t') = \begin{cases} \frac{1}{k}\left(1 - \frac{t'}{\Delta} + \frac{\tau}{\Delta}\left(1 - e^{-t'/\tau}\right)\right), & 0 \le t' \le \Delta \\ \frac{1}{\eta}\left(\frac{\tau^2}{\Delta} e^{-t'/\tau}\left(e^{\Delta/\tau} - 1\right)\right), & t' > \Delta \end{cases} \tag{5.1}$$

The derivation of *Eq(5.1)* is shown below.



$$F(t) = \begin{cases} F_1(t) = 1, & 0 < t \leq T \\ F_2(t) = \dfrac{-t}{\Delta} + \dfrac{T}{\Delta} + 1, & T < t < T + \Delta \\ F_3(t) = 0, & t > T + \Delta \end{cases}$$

Figure 5.4-Axial load modelled as a ramp function. Probe 'lift-off' occurs at time t=T

The ramp function is controlled by the parameter Δ. Now, recall the Voigt model and consider its Laplace transform.

$$\mathcal{L}\{F(t)\} = \mathcal{L}\{k\varepsilon(t) + \eta\dot{\varepsilon}(t)\}$$

$$F(s) = k\mathrm{E}(s) + \eta s\mathrm{E}(s)$$

$$\mathrm{E}(s) = F(s) \cdot \frac{1}{\eta}\left(\frac{1}{s+\alpha}\right), \quad \alpha = \frac{k}{\eta} \tag{5.2}$$

This gives a representation for strain in the transform domain, E(s). Some useful formulae for this analysis are shown below.

- Some relevant Laplace Transform pairs:

$$\frac{1}{s} \leftrightarrow U(t) \equiv \begin{cases} 0, & t < 0 \\ 1, & t \geq 0 \end{cases}$$

$$\frac{1}{s^2} \leftrightarrow t \cdot U(t)$$

$$\frac{1}{s+\alpha} \leftrightarrow e^{-\alpha t}U(t)$$

$$e^{-sT}F(s) \leftrightarrow f(t-T)\,U(t-T)$$

- Partial fraction expansion (PFE) of common transform expressions leads to Eq(5.3) and Eq(5.4).

$$\frac{1}{s}\cdot\frac{1}{s+\alpha}=\frac{1}{\alpha}\left(\frac{1}{s}-\frac{1}{s+\alpha}\right) \tag{5.3}$$

$$\frac{1}{s^2}\cdot\frac{1}{s+\alpha}=\frac{1}{\alpha}\left(\frac{1}{s}-\frac{1/\alpha}{s}+\frac{1/\alpha}{s+\alpha}\right) \tag{5.4}$$

Since $F_3(s)$=0, we need only consider F_1 and F_2.

$$F_1(s)=\mathcal{L}\{F_1(t)\}=\mathcal{L}\{1\}=\int_0^T e^{-st}dt=\frac{-e^{-st}}{s}\Big|\begin{matrix}T\\0\end{matrix}=\frac{1}{s}-\frac{e^{-sT}}{s} \tag{5.5}$$

$$F_2(s)=\mathcal{L}\{F_2(t)\}=\mathcal{L}\left\{1+\frac{T}{\Delta}-\frac{t}{\Delta}\right\}=\int_T^{T+\Delta}\left(1+\frac{T}{\Delta}-\frac{t}{\Delta}\right)e^{-st}dt=$$

$$\left[1+\frac{T}{\Delta}\right]\left(\frac{-e^{-st}}{s}\right)\Bigg|_{T}^{T+\Delta}-\frac{1}{\Delta}\left(\frac{-te^{-st}}{s}-\frac{e^{-st}}{s^2}\right)\Bigg|_{T}^{T+\Delta}=$$

...after some cancellations

$$F_2(s)=e^{-sT}\left(\frac{1}{s}-\frac{1/\Delta}{s^2}\right)+e^{-s(T+\Delta)}\left(\frac{1/\Delta}{s^2}\right) \tag{5.6}$$

Next, sum the forces (*Eq(5.5)* and *Eq(5.6)*) and using transform pairs, *Eq(5.2)* and the PFEs in *Eq(5.3)* and *Eq(5.4)*, solve for the strain as a function of time.

$$F(s)=F_1(s)+F_2(s)+F_3(s)$$

$$F(s)=\frac{1}{s}+\frac{1}{\Delta}\left(\frac{e^{-s(T+\Delta)}}{s^2}-\frac{e^{-sT}}{s^2}\right)$$

$$\mathrm{E}(s)=F(s)\cdot\frac{1}{\eta}\left(\frac{1}{s+\alpha}\right)$$

$$\mathrm{E}(s)=\frac{1}{\eta}\left[\frac{1}{\alpha}\left(\frac{1}{s}-\frac{1}{s+\alpha}\right)+\frac{1}{\Delta}\cdot\frac{1}{\alpha}\left(e^{-s(T+\Delta)}-e^{-sT}\right)\cdot\left(\frac{1}{s^2}-\frac{1/\alpha}{s}+\frac{1/\alpha}{s+\alpha}\right)\right]$$

Using the transform pairs, the inverse transform can be represented as:

$$\varepsilon(t) = \frac{1}{\eta}\left[\frac{1}{\alpha}(1 - e^{-\alpha t})U(t) + \frac{1}{\alpha\Delta}\left(\frac{1}{\alpha} - (t - T) - \frac{1}{\alpha}e^{-\alpha(t-T)}\right)U(t - T)\right.$$
$$\left. + \frac{1}{\alpha\Delta}\left(t - (T + \Delta) - \frac{1}{\alpha} + \frac{1}{\alpha}e^{-\alpha\left(t-(T+\Delta)\right)}\right)U(t - (T + \Delta))\right]$$

Consider time starting at lift-off, and assume T>>0 i.e. the probe in compression state has reached a steady state having been placed on the patient for a sufficiently long period of time (in practice ~15-30 seconds).

$$let\ t' = t - T, \qquad with\ T \gg 0$$

then

$$\varepsilon(t') = \frac{1}{\eta}\left[\frac{1}{\alpha}\left(1 - e^{-\alpha(t'+T)}\right)U(t' + T) + \frac{1}{\alpha\Delta}\left(\frac{1}{\alpha} - t' - \frac{1}{\alpha}e^{-\alpha t'}\right)U(t')\right.$$
$$+ \frac{1}{\alpha\Delta}\left(t' - \Delta - \frac{1}{\alpha} + \frac{1}{\alpha}e^{-\alpha(t'-\Delta)}\right)U(t'$$
$$\left. - \Delta)\right] \qquad (5.7)$$

The first term of *Eq(5.7)* in brackets will go to constant 1/α. A final representation is shown below:

$$\varepsilon(t') = \begin{cases} \frac{1}{\eta}\left[\frac{1}{\alpha} + \frac{1}{\alpha\Delta}\left(\frac{1}{\alpha} - t' - \frac{1}{\alpha}e^{-\alpha t'}\right)\right], & 0 < t' \le \Delta \\ \frac{1}{\eta}\left[\frac{1}{\alpha^2\Delta}e^{-\alpha t'}(e^{\alpha\Delta} - 1)\right], & t' \ge \Delta \end{cases}$$

and recalling the relationship of α to k and η

$$\varepsilon(t') = \begin{cases} \frac{1}{k}\left[1 - \frac{t'}{\Delta} + \frac{\eta}{k\Delta}\left(1 - e^{-\frac{k}{\eta}t'}\right)\right], & 0 < t' \le \Delta \\ \frac{\eta}{k^2\Delta}\left[e^{-\frac{k}{\eta}t'}\left(e^{\frac{k}{\eta}\Delta} - 1\right)\right], & t' \ge \Delta \end{cases}$$

Finally, define time constant τ =η/k, this results in *Eq(5.1)*.

Using the elastography algorithm of Chapter 3, strain was calculated over sequential pairs of images acquired at 13 fps and accumulated to produce the data points. Consider a time sequence of images [I_1,I_2,...,I_N] with I_1 corresponding the starting point (before the weighted ring is lifted off). First, time reverse the image sequence. Then, let ε_i be the strain image generated by comparing I_i with I_{i+1} and set $\varepsilon_0=0$. The accumulated strain, ε_{ACC} can be computed from

$$\varepsilon_{ACC}(n) = 1 - \prod_{i=0}^{n}(1-\varepsilon_i), \quad n = 0,1,\dots,N-1 \tag{5.8}$$

Note that a prerequisite for using *Eq(5.8)* is tracking and compensating for the motion of each pixel over the entire sequence of images in order to ensure that the correct strain values are accumulated. Motion vectors are already available via the displacement fields that accompany the strain estimates.

All ε_{ACC} curves have a common baseline of 0% strain. By time reversing the ε_{ACC} sequence, the accumulated strain can be depicted in normal time as shown in Figure 5.5. Curve fitting involved optimizing the η and Δ parameters which would be expected to vary spatially; *1/k* could be found empirically from the maximum accumulated strains, that is

$$1/_k = \max(\varepsilon_{ACC}) \tag{5.9}$$

As *Eq(5.1)* is piecewise continuous, an exhaustive coarse to fine search over a pre-determined range of η and Δ values was used to find the fit with the minimum mean squared error (MMSE). This was accomplished through some initial trial and error and educated guesses considering the expected ranges of τ (~1s) and k (~10-10000). A rough range for η was set at 0-900 in increments of 50 (Note: because a unit step force is assumed in these experiments, stiffness and viscosity cannot be expressed in terms of

Pa and Pa·s, strictly speaking). After one pass of the curve fitting, the best fit was chosen based on the MMSE, an average and max η was calculated and a new search, having been refined about these values, was performed. Ultimately, precision was obtained to within 1 unit of viscosity.

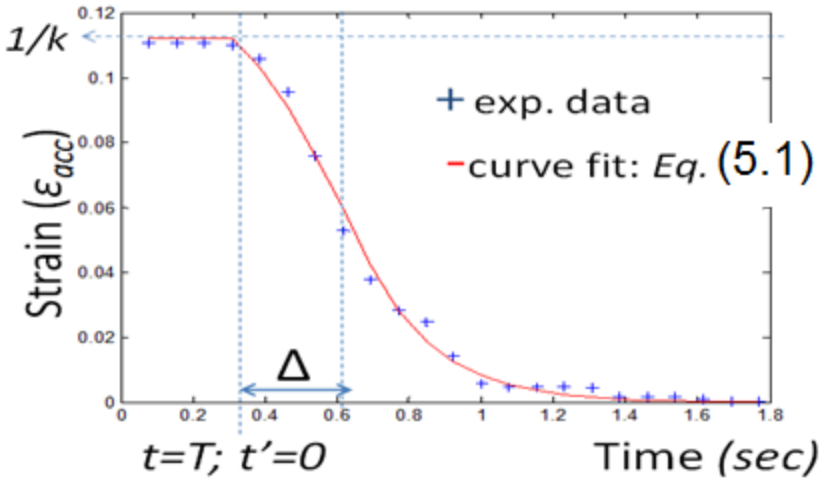


Figure 5.5- Experimental Curve fit of Creep Response to a sudden 'liftoff' force.

The HYFIVE system is thus a combination of the strain and displacement estimators from Chapter 3, a high frame rate US machine and a probe canister device all brought together by equations *5.1*,*5.8* and *5.9*.

5.3 Results

5.3.1 Phantom Experiment

A phantom was constructed to the same specification as that in Chapter 3 (Sect. 3.5.2); a circular inclusion with stiffness of approximately 3 times that of its surroundings. The phantom provided a controlled source for testing the probe canister function and ensuring proper execution of the viscoelastic algorithm. It was not expected to mimic the complex viscoelastic system of real breast tissue. Nor was it possible to specify the

phantom's viscosity, however results from an experiment in [127] using a similar phantom setup suggests a greater viscosity would be exhibited by the stiffer and more dense circular inclusion.

Figure 5.6(a) depicts two representative sample creep responses (point A -inside the inclusion, point B -outside the inclusion) and their respective curve fits. It is clear that the inclusion exhibits less strain. By normalizing the curves, the difference in time constant becomes apparent as well; the circular inclusion is 'slower' to decompress and reach a rest state. This result is consistent with those in [127] where the time constant, τ, is referred to as the tissue retardation time.

Figure 5.6(a)→(b-d) depict the strain ε, viscosity η and time constant τ respectively (all of which are related by $\tau = \eta \cdot \varepsilon$). Consistent with the phantom specifications, the ratio of average strain inside the circular inclusion to that of outside (defined hereafter as a contrast metric) was found to be approximately 1:3. The viscosity image suggests the inclusion has an η approximately 6 times that of its surroundings. Figure 5.6(a)→(e) depicts the r^2 image, defined as the normalized cross correlation between data and curve fit points. In this scan, r^2 values were all well above 0.92 indicating a good quality curve fit.

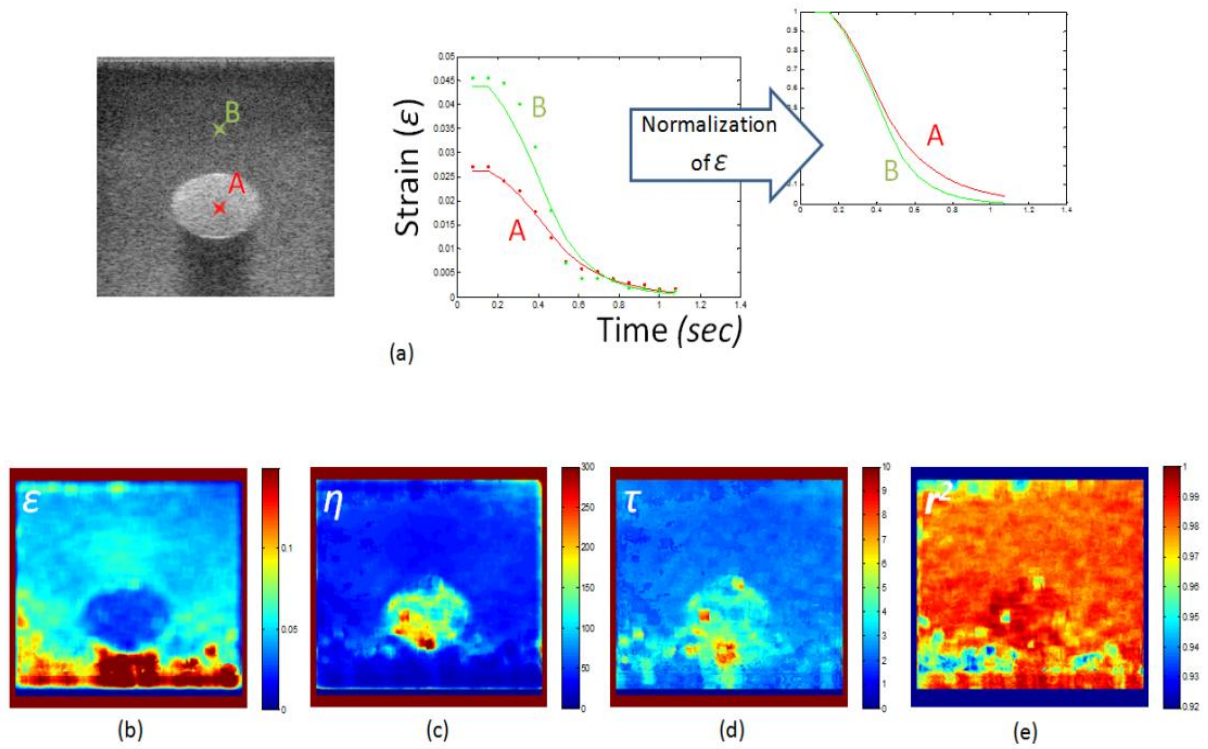


Figure 5.6(a)- (a) B-mode image with points A and B selected from inside and outside the circular inclusion respectively and the resulting creep curves. Note: normalization makes the difference in time constant more prominent visually. (b) Strain Image (Note: blue->low strain, red->high strain), (c) Viscosity Image and (d) Time constant image. (e) r^2 image.

Repeatability

The experiment was repeated again; several minutes later, a second data set was obtained using the canister device on the same phantom in roughly the same slice/imaging plane. The images of Figure 5.6(a) and Figure 5.6(b) are displayed using the same dynamic range/color mapping for easy comparison.

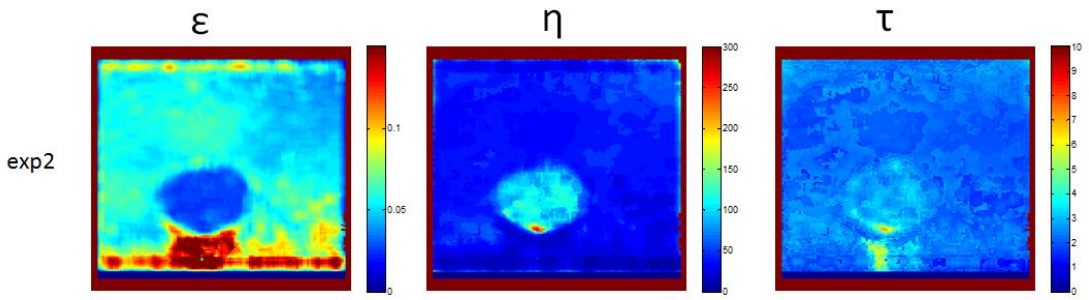


Figure 5.6(b)- Experiment results from another acquisition (see Figure 5.6(a))

The images are comparable but the time constant, τ, is less prominent in the second data set; overall, strain is slightly higher and viscosity lower.

5.3.2 Clinical Data Experiments

Four sets of clinical data are presented in this section. In each case, the r^2 values exceeded 0.9 across the entire ROI. A summary of patient pathology can be found in Table 5.1.

Table 5.1- Patient Summary for HYFIVE clinical data

Patient #	Cancer Type
P1	IDC + DCIS*
P2	IDC + DCIS*
P3	IDC + DCIS*
P4	Mucinous Carcinoma

*IDC + DCIS: An invasive ductal carcinoma is generally found with associated *in situ* disease present

Figure 5.7 depicts the resulting scans from P1. In addition to being stiffer (Figure 5.7(b)) and more viscous (Figure 5.7(c)) than its neighboring tissue, the tumor also

takes longer to decompress after external stress is removed (Figure 5.7(d),(e)). The η image also has an increase in contrast of ~20% over the strain image.

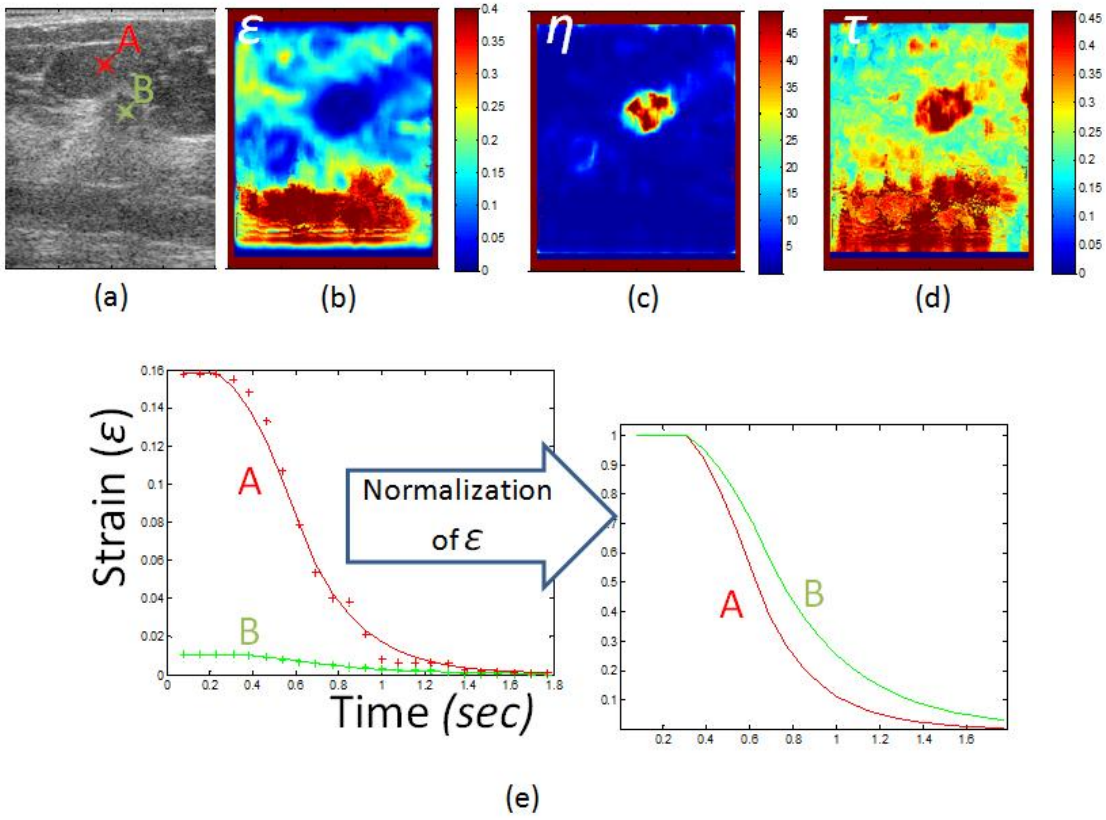


Figure 5.7-P1 results (a) B mode Image,(b) Strain Image, (c) Viscosity Image, (d) Time Constant Image and (e) Points A and B selected from outside and inside the lesion respectively and the resulting creep curves and data points

Figure 5.8 depicts results from the same patient, taken in another plane. However, in this case acquisition failed owing to sticking of the weight ring during the 'lift-off' phase (friction between the weight ring and canister body) leading to a distinctively *non*-ramp like applied force (Figure 5.8(e)). The figure demonstrates the ability of the algorithm to capture various types of tissue motion whether or not it conforms to the model. Of course, none of these image results would be deemed reliable measures of viscosity.

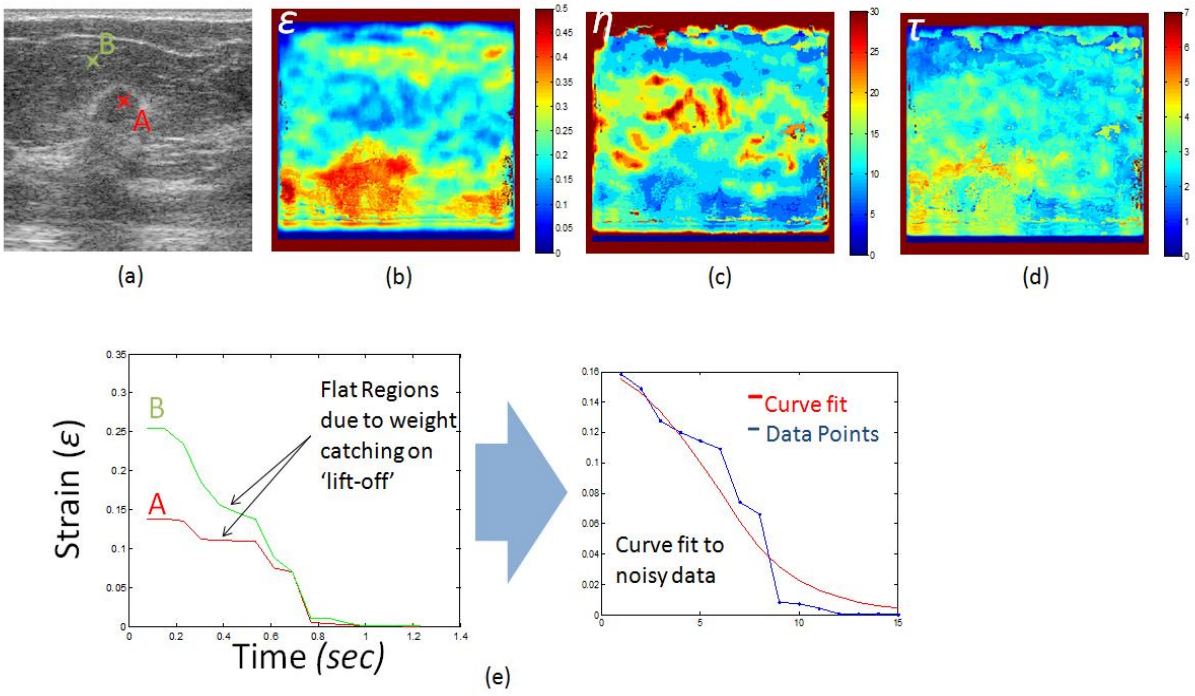


Figure 5.8-P1 results from a failed acquisition (a) B mode Image,(b) Strain Image, (c) Viscosity Image, (d) Time Constant Image and (e) Points A and B selected from inside and outside the lesion respectively and the resulting creep curves and data points. Note: The data is severely corrupted by the noisy acquisition.

Figure 5.9 depicts the results for P2. In this case, no considerable difference in contrast between the η and ε image is apparent. Consequently, the lesion is not clearly observable in the τ image. This characteristic is observed again for P3 in Figure 5.10.

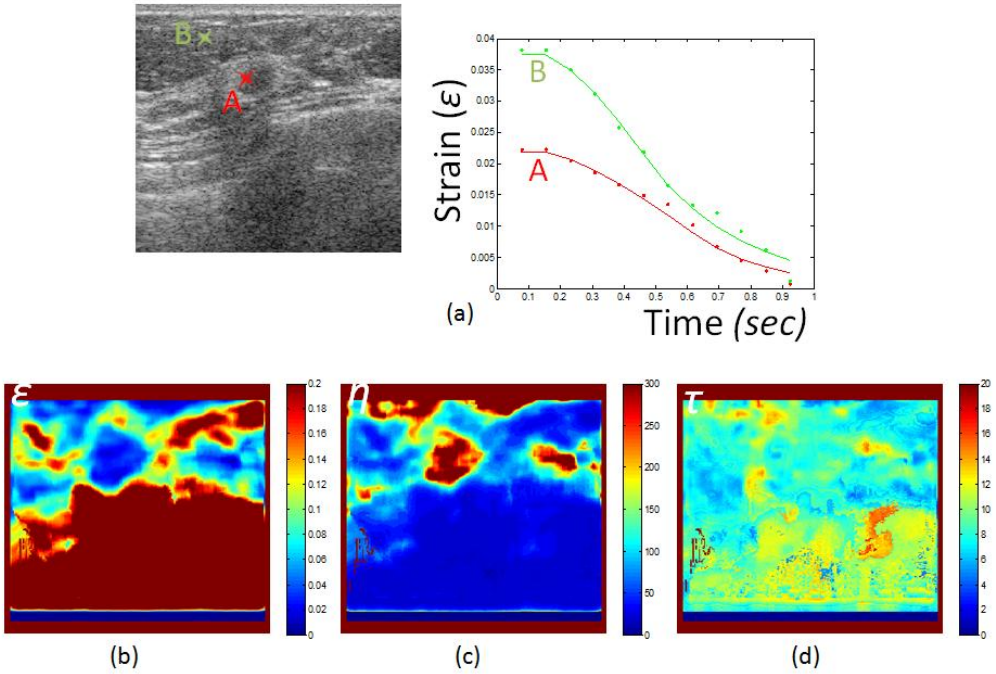


Figure 5.9-P2 results: (a) B-mode and selected strain curves, (b) Strain Image,(c) Viscosity Image (d) Time Constant Image

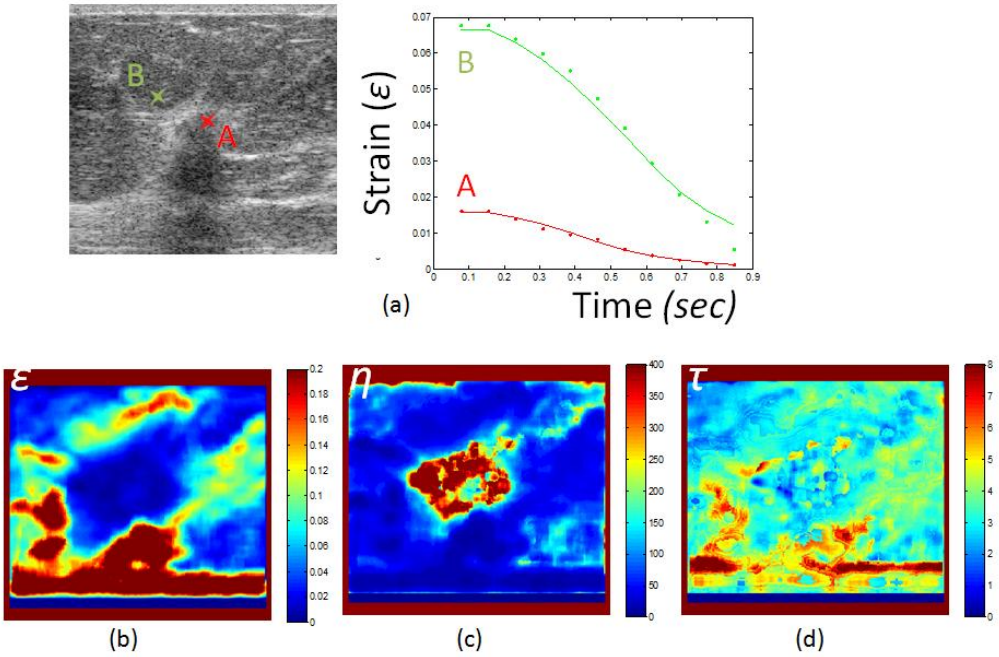


Figure 5.10- P3 results: (a B-mode and selected strain curves,(b) Strain Image,(c) Viscosity Image (d) Time Constant Image

Figure 5.11 shows the results for the mucinous carcinoma of P4. Mucinous means 'contains a lot of mucous'. One would expect a somewhat viscous reaction, as indeed a retarded tissue response from the tumour region is indicated by the τ image.

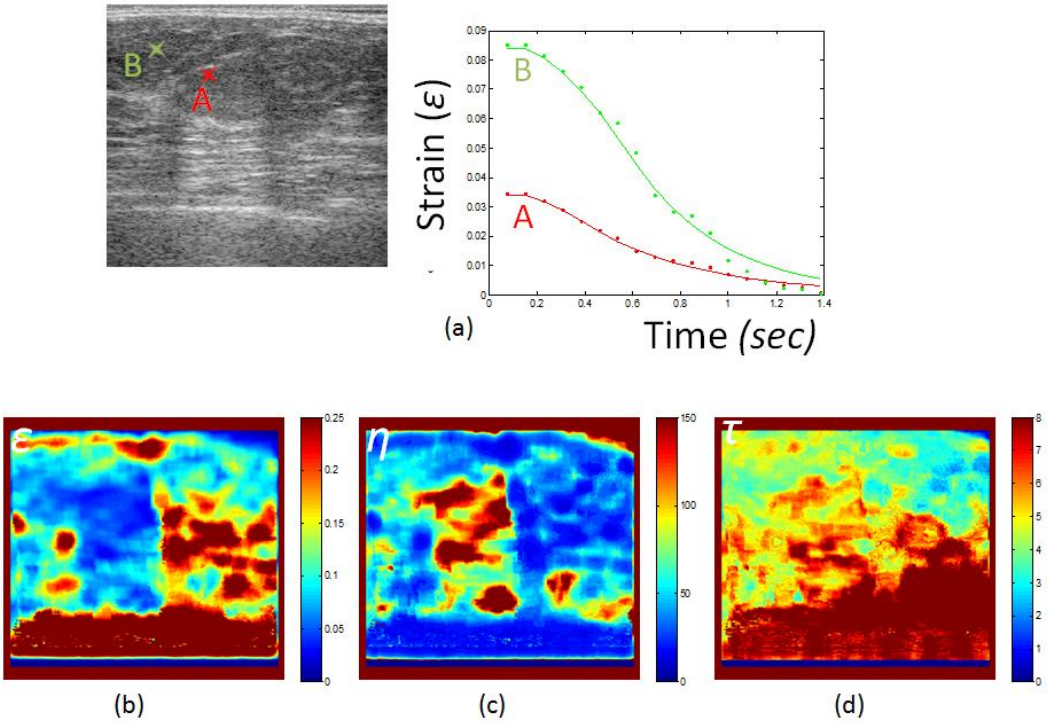


Figure 5.11-P4 results from a Mucinous carcinoma. (a) B-mode and selected strain curves, (b) Strain Image,(c) Viscosity Image (d) Time Constant Image

5.4 Discussion

The 1st order Voigt model and *Eq(5.1)* proved to be accurate representations for the type of motion incurred in tissue by the HYFIVE system. Complicated analysis on more sophisticated models as in [126-127] would seem to be unnecessary. Furthermore, less than 2 seconds worth of frames was sufficient for generating viscoelastic parameters.

Repeatability of the technique is an issue. Slight variations in the results were shown between Figure 5.6(a) and Figure 5.6(b). Possible sources of this variation may include inconsistent 'lift-off' of the probe weight and even the phantom itself; it is not clear if

viscosity (of gelatine or real breast tissue) should be regarded as a time invariant parameter. Temperature and strain history may be some of the subtleties which could play a role in the viscosity output.

This would open up the field of research to more extensive studies to perhaps monitor viscosity at different time points.

Given the current knowledge of tumour physiology it was expected to see a mix of viscoelastic properties in the tumour responses. This supposition was supported by the 4 sample cases presented in this chapter. However, without more in-depth histopathology for these patients any conclusions drawn from the images would be conjecture.

In all cases (including the phantom experiment), η image correlated well with the strain images, that is they would look very similar were it not for the colour mappings used. However, it should be clear that viscosity provides complementary information to strain imaging. If it did not, the τ images would simply be constant/blanks. In half the cases (P1 and P4), this meant an increase in image contrast when viscosity was compared with strain. An increase in image contrast is always a desirable result in image processing.

The curve fitting and strain accumulation process of *Eq(5.8)* effectively filters out outlying strain values. This filtering effect is observed in multi-compression techniques like that in [73], where a series of quasi-static strain images are averaged to remove noise at the expense of some contrast loss. The difference with HYFIVE is that rather than average out data (which generally results in information loss), it regularizes the data by fitting *Eq(5.1)* and obtains useful imaging parameters simultaneously (resulting in an information gain).

5.5 Conclusion

HYFIVE exploits the high frame rate of ultrasound systems to produce parametric images based primarily on tissue stiffness, viscosity and a time constant parameter (sometimes called a tissue retardation time). These images offer new insight into the physiology of tumours and their surroundings; it has been suggested that tissue viscosity could be related to tumour structure and angiogenesis. Further testing on a larger dataset with relevant histopatholgy would need to be done to assess the significance of viscoelasticity imaging.

The simple probe canister device was made from inexpensive materials and produced the desired applied stress in a controlled manner while still maintaining the probe's general purpose functionality.

Fundamentally, creep response estimation is quite reliable; the only variables involved, strain and time, can both be measured with reasonable accuracy. However, the technique is not suitable for quantitative measurement of tissue viscosity. This is owing to the fact that several assumptions were made about the nature of the input force and the loading history of the tissue. Moreover, image acquisition was not without its problems. Because of the rapid movement incurred, it was difficult to keep the ROI within the imaging plane throughout the entire sequence. Also, the fixed weight of the ring was found to be unsuitable for certain patients (either producing too much or too little displacement).

Making the canister more ergonomic and having an adjustable weight would be a priority for any future development of this technique. The system would also benefit from a higher frame rate in order to produce more data points. Given the initial results and potential use of viscoelasticity images for breast cancer imaging, the extra time and cost would be justified. From the point of view of this thesis, HYFIVE has established a

proof of principle, but requires a great deal more research. However, the major focus of this project lies in the proceeding chapters which show the merits of straightforward quasi-static strain images.

Chapter 6
Tumour Sizing Using B-mode and Elastography Features

6.1 Introduction

The purpose of this experiment was to investigate the role of ultrasound elastography in the sizing of breast lesions. Accurate tumour sizing has significant benefits to patients with early breast cancer (cancer that has not yet metastasized); it can provide surgeons with essential information prior to excision which could make the difference between a lumpectomy or a total mastectomy. Moreover, the size and spread of a tumour can also be indicative of certain prognoses [131].

As already mentioned in Chapter 2, combining conventional B-mode imaging with ultrasound elastography to improve diagnostic and sizing accuracy is not a new notion, see for instance [36,67]. However, each group has used its own US hardware, algorithms and acquisition techniques with varying performance results. Hence, one of the motivations for the work in Chapter3 and Chapter 4 was to provide a means of robust strain measurement with consistency in its display.

In order to validate the system, this chapter will describe the clinical study, hardware setup and sizing protocol used (Sect. 6.2) and present results from this tumour sizing experiment (Sect. 6.3). After taking in the discussion (Sect. 6.4) and conclusion (Sect. 6.5) the reader will hopefully be convinced that the colourful strain maps produced so far are more than just pretty images, but actually correlate well with underlying histology.

6.2 Methods

6.2.1 Hardware Setup and Scanning Protocols

All scans were performed with a Zonare z.one system and L10-5 probe (8.5 MHz with a linear footprint of 38.4mm and axial depth set depending on the patient (usually 40.0 or 50.0mm)). The Zonare research package and hardware protocols have already been describe in Chapter 3.



Figure 6.1- The Zonare L10-5 probe

Scans were acquired by the same single clinician in both sagittal and transverse planes (see Appendix A) using a de-compressing motion (the probe was initially pressed slightly into the patient and pressure was slowly released) which was found to be easier to control than a compression. This was in keeping with previous elastography studies performed with the same group of radiologists [12-13,73]. The clinician used feedback from the US monitor B-mode images to help keep the ROI in plane. If significant out of plane motion occurred, the scan was repeated until 'good' motion could be observed (in some cases this never occurred).

In an attempt to ensure consistency and correlation across the US images and pathology slides, the lesions were scanned in a single cross section (in each plane) corresponding to the largest observed area i.e. the biggest section of the tumour was imaged. This

helped later correlate images to pathology slices as pathologist were instructed to slice and analyse the largest cross section of the tumour from the surgical excision. The orientation of the tumour was noted by surgeons prior to excision in order to maintain the sagittal and transverse imaging planes.

In addition to data for this study, viscoelastic data and 3D data was also acquired. The entire scanning session typically took less than 10 minutes which was the approximate time allocated for each patient when conducting the study in clinic. The entire decompression sequence was saved for post processing; a 'movie' of the tissue deformation could be watched and reviewed. This was useful for the selection of frames to be considered for strain analysis as described in the next section.

6.2.2 Data Selection Process and Analysis

The human eye is capable of tracking tissue motion in a sequence of B-mode images [132], elastography is simply an automated and quantitative approach to describe tissue deformation. From the B-mode movies, a subset of frames could be selected as candidates for pre and post compression images for strain analysis. As mentioned in Chapter 4, displacement fields and a quality metrics were used to establish if there was significant signal noise/decorrelation. In good cases, image pairs were chosen such that they had ~2-3% average strain with ~5% maximum strain [76,109,133]. The idea was to maximize contrast at the limit of signal decorrelation. In cases where this criteria could not be achieved, the best image pair based on signal correlation and well defined axial motion was selected.

Taking advantage of the robust nature the strain algorithm, all elastographic parameters were fixed for all cases. The parameters used are given in Table 6.1.

Table 6.1-Strain Algorithm Parameters

Axial Window Size	5 mm
Lateral Window Size	9 samples
Lateral Search Range	± 4 sample
Axial Search range	Computed for ~5% average strain
FFT size	256
Down-Sample Factor	3 (making axial depth ≈ 330 samples typically)

A purpose built GUI was designed in MATLAB for quick loading and analysis of the strain data. It allowed for a view of the entire B-mode movie, strain and displacement fields as well as control of frame selection (pre and post) and the amount of transparency overlay and access to the actual data values by simply pointing and clicking on the image.

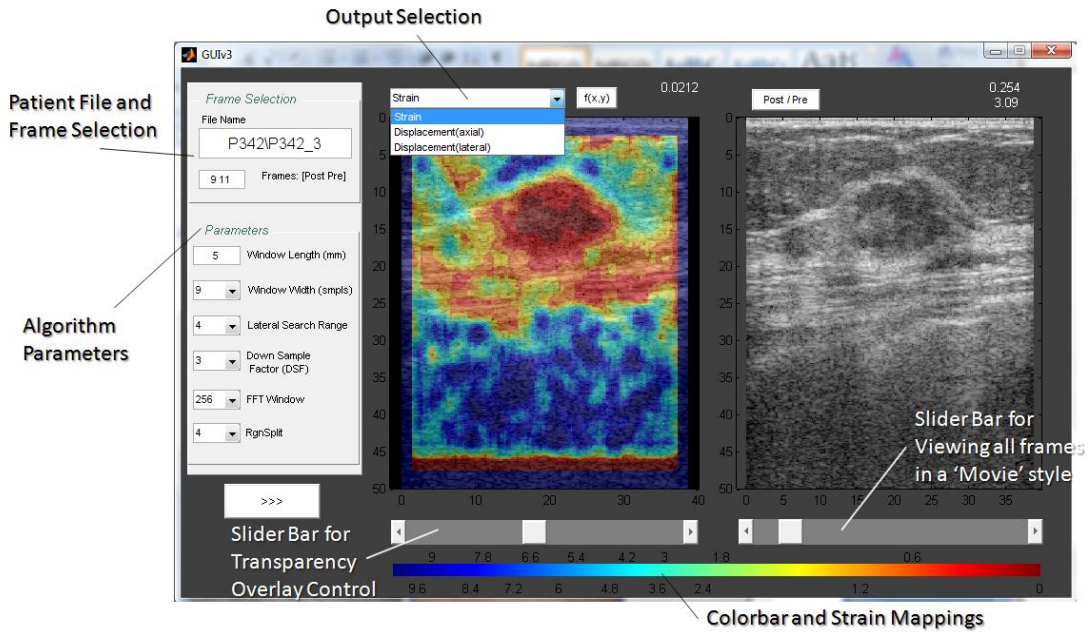


Figure 6.2-GUI for analysing acquired elastography data

6.2.3 Segmentation and Sizing

Segmentation of the tumour was carried out in both B-mode (alone) and using B-mode and Elastogram (B+E mode) analysis. All segmentation was done in the sagittal plane as these corresponded approximately to the cuts/slices of the histology slides. Tumours were sized from images in terms of width, depth and area. Area was computed using a polygon decomposition method using parallelograms (see Appendix B). The clinician simply had to click on an appropriate number of points along the tumour boundary. All images were presented to a single clinician (the same that conducted the scans) >2 months after the original scan in random order. B-mode and B+E mode segmentation were not carried out back to back and the B-mode segmentation was not viewable by the clinician during B+E segmentation. Moreover, the clinician was blinded to the histopathology.

B-mode segmentation followed standard clinical practice and essentially comprised of segmenting the hypoechoic region of the image. B+E segmentation followed the following set of clinically based rules (also found in previous work [13]):

Rule 1. Exclude or ignore obvious artefacts such as posterior shadowing/severe signal attenuation and make appropriate compensations based on following rules

Rule 2. Using B-mode, further exclude regions of obvious normal anatomical origin which may happen to display low strain (e.g. cooper's ligaments) and be in proximity to the tumour

Rule 3. Anything considered tumour in the B-mode image should be included in the B+E segmentation

Rule 4. Otherwise, use transitions from dark orange to yellow in the strain image to delineate tumour boundaries

Yet another GUI was developed to carry out the segmentation efficiently and provide the clinician with all relevant information. A screenshot is shown in Figure 6.3.

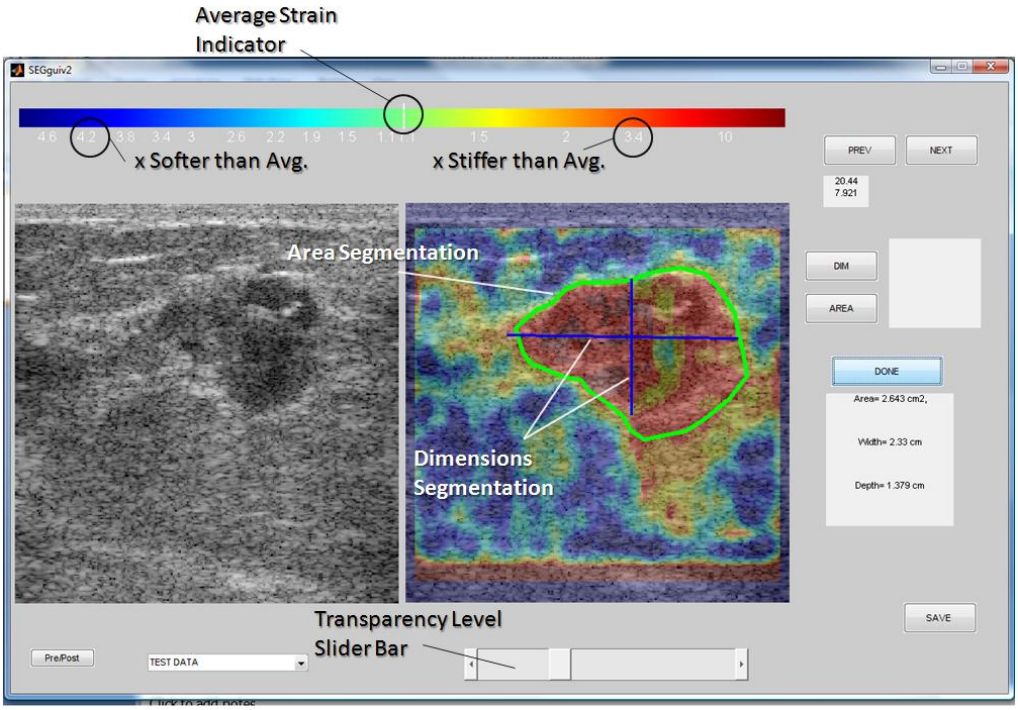


Figure 6.3-GUI developed for B-mode and B+E mode segmentation by clinicians

When considering area as a measurement it is important to consider the possible errors involved. Let us assume tumours have a rough circular shape and consider what happens when an area is segmented with a single pixel error. This error refers to bias when selecting the boundary; whether the clinician chooses point just on, outside or inside the boundary during segmentation. Thus the effect a clinician's subjectivity requires some consideration.

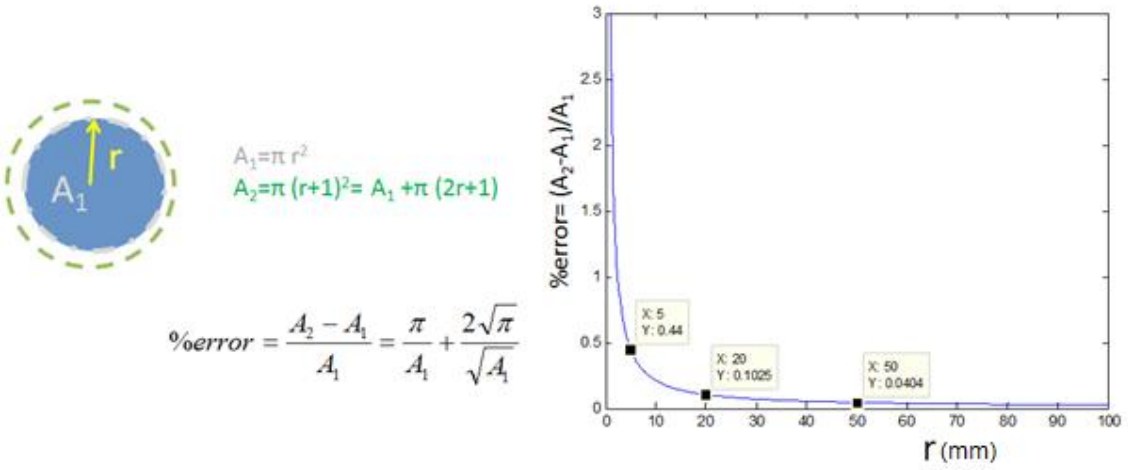


Figure 6.4-Segmentation Bias and resulting error derivation. A_1 is the true area, A_2 is the overestimation

Though barely perceptible visually, the error accumulates over the circumference of the tumour and can result in total error ranging from as little as ~5% for larger tumours to as much as 40% for smaller ones. The variance of these measurements and their dependency on tumour size should be considered when examining the accuracy of the system to size breast lesions.

Therefore, a reasonable margin for error in the area measurement could be derived from *Eq(6.1)*. Note, the error is a function of the tumour area, A.

$$\%error\ (in\ pixels) \approx \frac{\pi}{A} + \frac{2\sqrt{\pi}}{\sqrt{A}} \tag{6.1}$$

where A is the true area.

6.3 Sizing Results

6.3.1 Patient Summary

Ultrasound and histology data from 27 patients was obtained. A summary of these patients is listed in Table 6.2.

Table 6.2-Patient Summary

Tumour Characteristics	Total no. of Patients (27)
IDC	15
ILC	1
Mucinous	3
Lobular	1
Micropapillary	1
Solid Papillary	1
Adenoid cystic Carcinoma	1
Tubulolobular	1
Mixed: Mucinous + IDC	2
Mixed IDC/ILC	1

Just over 80% of patients had associated in situ disease in addition to their invasive carcinomas.

6.3.2 Exemplar Results

In this subsection, a number of typical patient examples are used to illustrate the 4 segmentation rules from 6.2.3 being applied.

In Figure 6.5, signal attenuation has caused a split in the elastogram. This lack of strain data is ignored (as per Rule 1) since continuity is seen in the B-mode image. Moreover, recognizable anatomical features such as layers of ligaments are excluded from the

bottom part of the image and upper right corner, as per Rules 2,3, and 4. All images are to scale; in this case B+E mode shows a significant improvement, with respects to the histology slide as a reference, over the B-mode segmentation in terms of gauging the general shape and size.

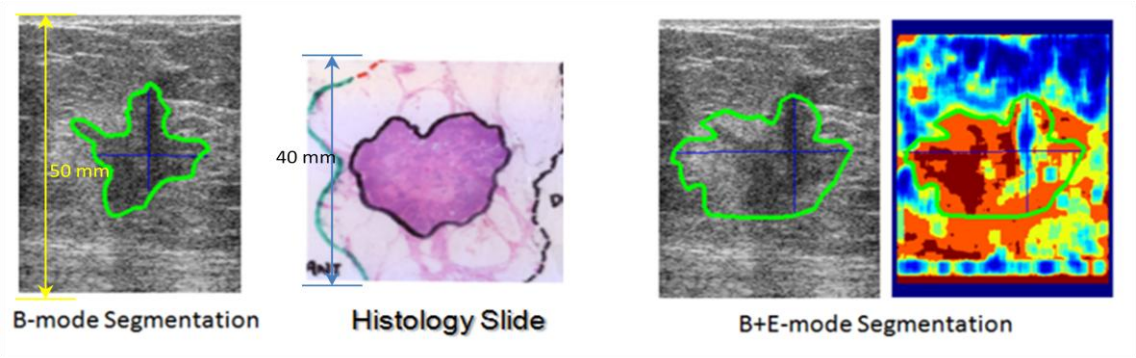


Figure 6.5-B-mode and B+E mode segmentation: More accurate segmentation was achieved using B+E

Figure 6.6 depicts a case where the tumour boundaries far exceed the hypoechoic region segmented in the B-mode image. The segmentation in both cases is otherwise straightforward.

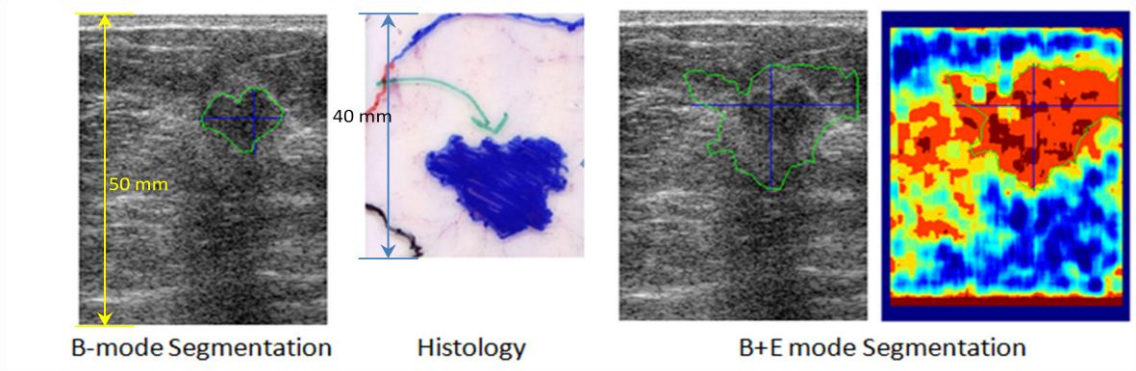


Figure 6.6-Blurred tumour boundaries in B-mode result in significant under sizing of the tumour. B+E mode captures the size and shape significantly better.

Figure 6.7 exemplifies a case where B-mode data and Rule 3 salvages the B+E mode segmentation. The main assumption that all tumours exhibit greater stiffness uniformly throughout does not hold for this patient.

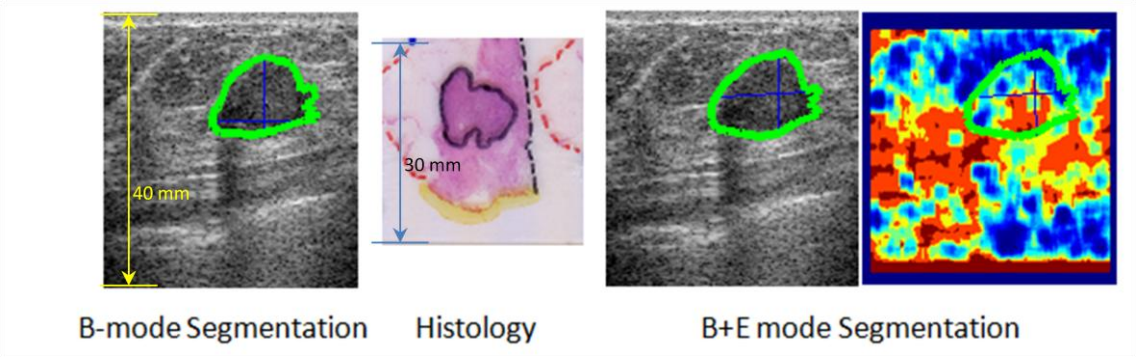


Figure 6.7-A Segmentation case where B-mode data takes precedence.

In many cases the B-mode and B+E mode were in relatively good agreement. A good example is presented in Figure 6.8. Though the boundaries are slightly different, overall area is similar. During scanning, the largest cross section of tumour observed was chosen for imaging. Consequently, with histology slides containing more than one slice, the largest section was chosen as the gold standard.

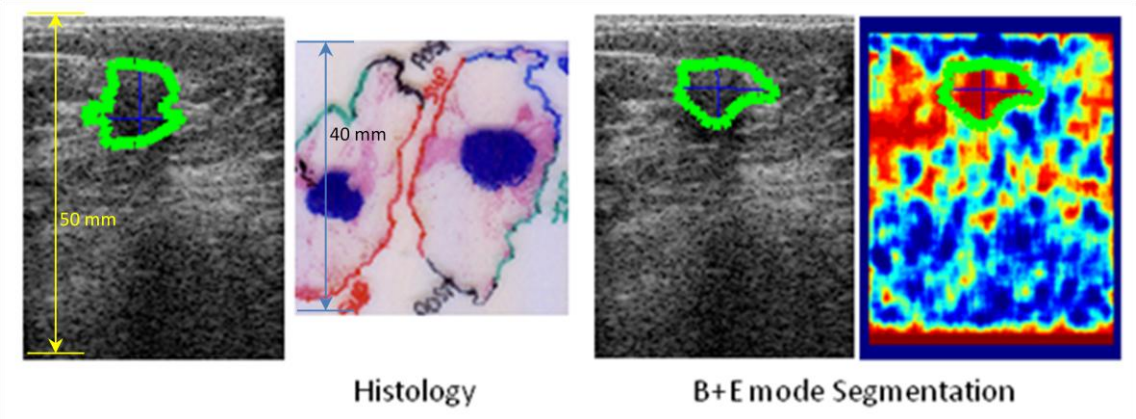


Figure 6.8-B-mode and B+E mode segmentation in relative agreement. Note: area measurements were conducted on the largest slice available from histology

Because of 4 rules used, the effect of posterior shadowing on segmentation in B+E mode were mitigated. Examples of these case have already been shown in Figures 6.5, 6.7 and 6.8. These cases also emphasize the importance of using the B-mode data in *conjunction* with elastography and an awareness of both their limitations.

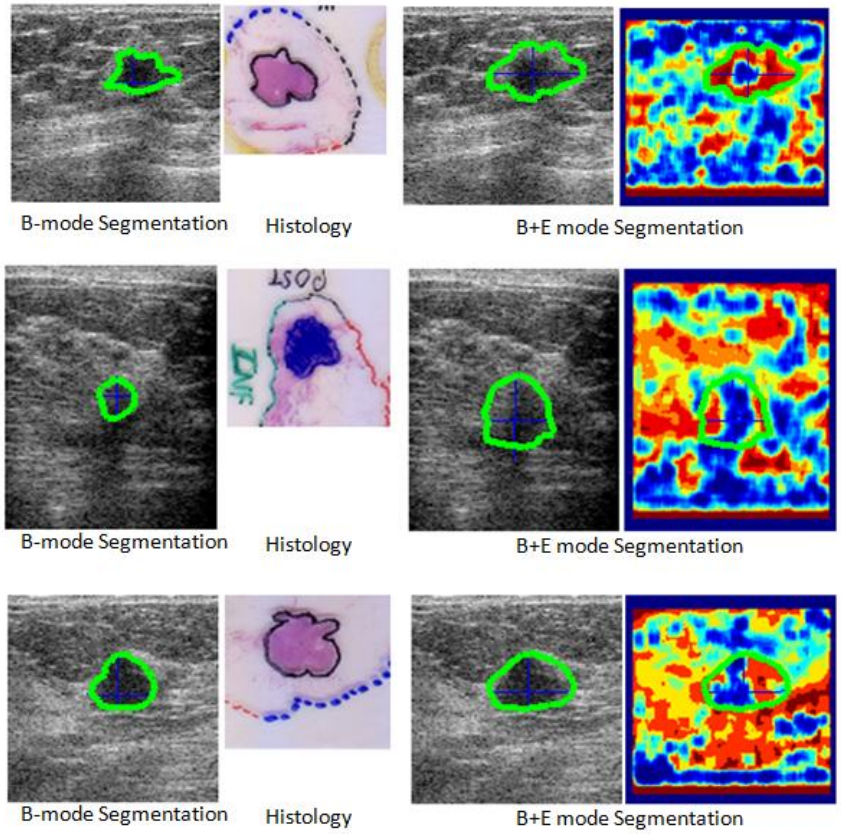


Figure 6.9-Segmentation despite severe posterior shadowing and signal attenuation

6.3.3 Statistical Results

Figure 6.10 shows the percent difference between the B-mode (blue) estimate of area and the equivalent from the histology slide (used as the gold standard and indicated by the 0 line). The B+E mode results are shown in red. Overall, the B+E has a tendency to overestimate the tumour size and the B-mode underestimates it. If we allow for a shrinkage of up to 10% in the tumour after excision we get Figure 6.11 [134].

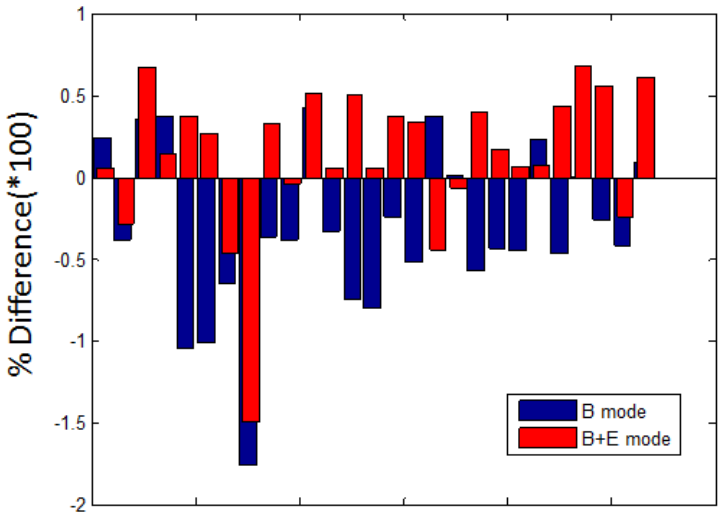


Figure 6.10-Error plot of B-mode and B+E mode segmentation using the histology slide as gold standard

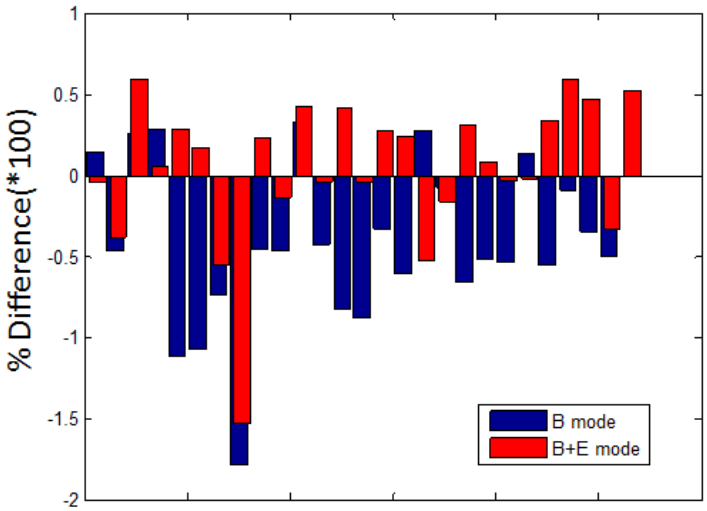


Figure 6.11- Error plot of B-mode and B+E mode segmentation using the histology slide as gold standard. Assume 10% shrinkage occurred in the histology slide after excision.

When considering shrinkage in the histology slides, the overall average. percent difference improves for B+E, from 36% to 33%, and worsens for B-mode from 48 to 52%.

Under assumptions imposed by *Eq(6.1)* we can define accuracy as the proportion of cases where histology slide measurements fall within the range of the B-mode and B+E mode segmentation results. Figure 6.12 plots the results from all 27 cases with error bars defining the allowable margins for an accurate segmentation.

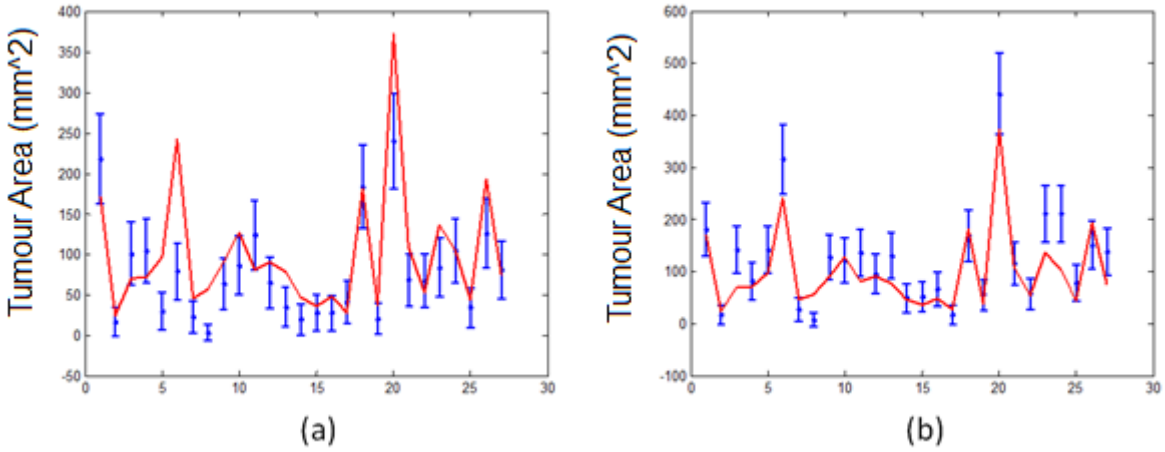


Figure 6.12- No shrinkage assumed: (a) B-mode area measurements, the red curve plots the histology slide areas, error bars are derived from the B-mode area segmentations. (b) same as (a) but using B+E mode segmentation data.

Examining the plots in Figure 6.12 (a) revealed for the B-mode case, 15 out of 27 were sized within margins for error giving an accuracy of 56%. From Figure 6.12(b), using B+E resulted in 19 out of 27 or 70% accuracy. Let us consider what happens when 10% shrinkage is assumed (Figure 6.13).

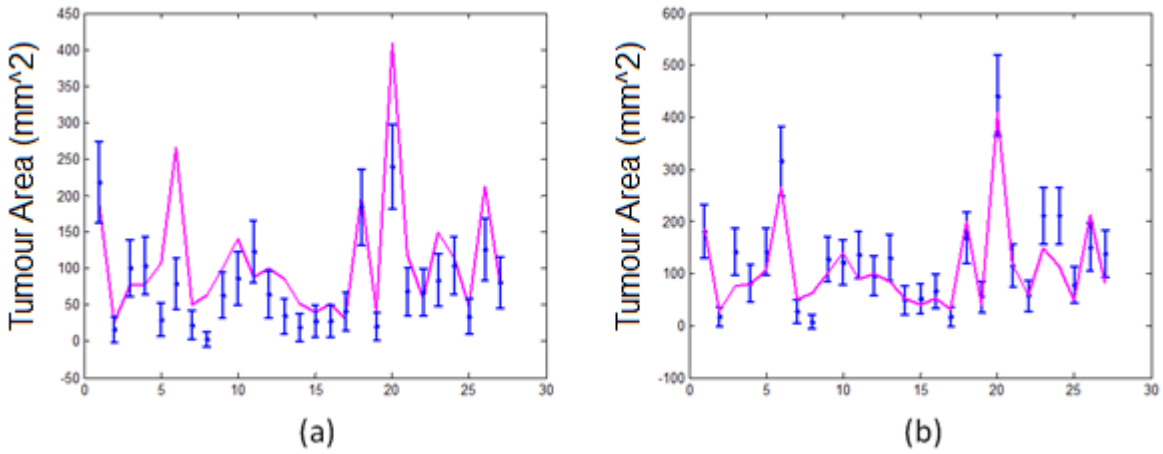


Figure 6.13- 10% shrinkage assumed: (a) B-mode area measurements, the purple curve plots the histology slide areas, error bars are derived from the B-mode area segmentations. (b) same as (a) but using B+E mode segmentation data.

The B+E mode accuracy remains at 70% (though overall % difference dropped). B-mode segmentation worsened, 12 of 27 successful cases results in 44% accuracy. All results are summarize in Table 6.3.

Table 6.3-Summary of statistical results

	No Shrinkage		10% Shrinkage	
	Accuracy	**Avg. %Difference**	**Accuracy**	**Avg.% Difference**
B-mode	56%	48%	44%	52%
B+E mode	70%	36%	70%	33%

In Figure 6.14, the segmentation error (assuming no shrinkage) for both B-mode and B+E mode is plotted versus the tumour size obtained from histology. As predicted by the model set out in *Eq(6.1)*, there is a general trend of smaller errors occurring for larger tumour sizes.

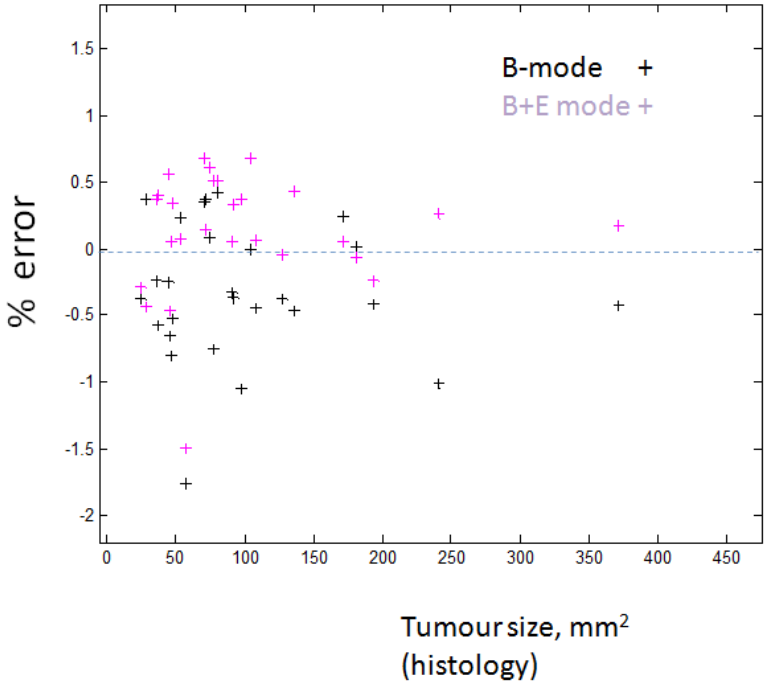


Figure 6.14- Segmentation error as a function of Tumour size. Error tends to increase as tumours get smaller.

6.4 Discussion

Overall, B+E mode segmentation showed an improvement in accuracy over B-mode segmentation alone by 14% (no shrinkage assumed) and 26% (with 10% shrinkage). Moreover, the overall estimate of tumour size was shown to be as much as ~20% better. In general, B+E erred on the side of caution by overestimating tumour size, whereas B-mode segmentation underestimated it. From a clinical perspective, the former would be the safest choice.

Using area as a measure for tumour size has one major disadvantage, slight bias in the segmentation can result in a substantial margin for error. This needs to be taken into consideration, as was done in this chapter, when dealing with area measurements and drawing conclusion from them. A conservative error margin was derived based on the

change in measured area due to a single pixel error during manual segmentation. Having only a single clinician to evaluate the data, this allowed for the consideration of clinician bias due to subjectivity regarding segmentation of boundaries. Ideally, multiple clinicians (and repeated segmentations from each clinician) would have further bolstered the statistical results presented in this chapter.

Also, full 3D analysis and histology was not available for this study so the effects of 3D pose error could not be assessed. Moreover, only absolute area was considered, in keeping with standard clinical practices. The shape of the tumours were only considered qualitatively (with examples of good agreement as in Figures 6.5-6.6. A registration process to evaluate the agreement between US images and histology could provide more insight with regard to shape characteristics and size.

Another important conclusion from this experiment is that elastography alone cannot cope without information from standard B-mode images. Both modalities provide complementary information required for dealing with the complexities of breast cancer imaging. This relationship is embodied in the 4 rules presented in Sect. 6.2.3.

We can conclude from images like those in Figures 6.5 and 6.6 that the full extent of tumours is not always readily visible in B-mode and they do not always conform to the stereotypical dark hypoechoic region. It can also be concluded that elastography has demonstrated the potential to fill this much needed gap in information. The hidden extent of the tumour exhibits different biomechanical properties to that of healthy tissue making it readily visible in strain images.

In general, strain information allows clinicians to reconsider the nature of certain tissues that would otherwise be ignored in conventional B-mode analysis.

It is also interesting to note that certain tumours exhibit this hidden extent (visible in strain images) while others of the same type do not. One possible explanation is the

nature of the tissue surrounding the lesion. Insight may be gained in future work examining the role of breast density and composition in tumour growth. Elastography would play a key role in such an investigation.

6.5 Conclusion

This chapter has helped establish that elastography does indeed correspond well with underlying histology by presenting the results of an extensive tumour sizing study involving data from 27 patients. Not all of a tumour shows up clearly defined as a dark region in the B-mode image. In order to help clinicians, elastography can provide complementary information to conventional ultrasound imaging. With this in mind, we can proceed to Chapter 7, where a tumour's response to chemotherapy and its elastic properties are monitored over time.

Chapter 7
NeoAdjuvant Study

7.1 Introduction

This chapter presents data from a pilot study to monitor the effects of chemotherapy on tumour and peritumour stromal tissue using ultrasound elastography.

Motivation

The need for a chemotherapy monitoring tool has already been elucidated in Chapter 2. Moreover, the motivation for using elastography in this role has been made clear. In Chapter 6 it was established that tumours exhibit distinctive mechanical characteristics, often undetectable by conventional imaging. Elastography can be effective in detecting the full extent of tumours; highlighting the boundary where tumour cell interaction takes place with stromal tissue.

This chapter examines whether the mechanical properties of tumour and stromal tissue are affected by chemotherapy to an extent where ultrasound strain imaging can detect it and provide insight into the therapy's effectiveness.

The eventual goal of this research is to develop a clinical tool (based on ultrasound elastography) which could be used to:

- Assess a patient's treatment plan and improve treatment outcome.
- Gain a better biological understanding of cancer and stromal cell interaction

The improved tumour sizing highlighted in Chapter 6 also suggests the potential for guided surgery applications which could also play a key role in cancer treatment.

7.2 Patients & Methods

7.2.1 Overview

The basic plan for the study was to periodically scan patients with primary breast cancer over the course of their neoadjuvant chemotherapy. Both ultrasound B-mode and elastography data would be acquired and any changes observed would be analysed. In the case of B-mode, conventional analysis involved simply noting any size changes in the tumour attributed to the chemotherapy. With elastography, observable changes in the strain distribution were expected.

Some limited pathology information was available to correlate to the findings. A core biopsy result (taken during the diagnosis stage) and biopsy/surgical excision results proceeding treatment were available as a standard part of patient treatment. In addition, MRI scans also provided a look at any residual disease left behind after treatment; these bits of data primarily provided information as to the type of cancer and whether or not in the end the patient responded to chemotherapy.

As a side attraction to the main experiment, patient lymph nodes were also scanned when possible. Lymph nodes status (*positive* or *negative* for the presence of cancer cells) have been found to correlate with tumour size and their ability to spread [135]. Changes in the lymph node size and composition could potentially provide supporting evidence of a pathological response. Several studies have been performed to examine the elastographic features of lymph nodes.[136-137] Consequently, lymph nodes were scanned as supplementary indicators of tumour response. As with tumours in this study, lymph nodes were examined in two ways: their size (obtainable from B-mode) and their elastographic features. It was of primary interest to see if they were suitable subjects for ultrasound strain imaging.

There were many other challenges to this study, both logistical and image processing related which will all be topics of discussion later in this chapter.

7.2.2 Patient Recruitment

Patients were recruited with full consent and ethical approval through the NHS Oxford Cancer Imaging Centre. In total, 7 patients with early primary breast cancers participated in the study. A summary of their details can be found in Table 7.1

Table 7.1-Neoadjuvant Study: Patient summary

Patient ID	Age (years)	Histology	# Scans	Coil Fitted?	Lymph Node Status	BI-RADS	Clinical Response	Histological Response (residual disease)
1	28	Poorly Differentiated IDC	7	x	Neg	4	Complete Response	NA
2	57	Moderately Differentiated IDC	3	√	Pos.	1		NA
3	40	Poorly Differentiated IDC	5	√	Pos.	3	Complete Response	NA
4	61	Moderately Differentiated IDC	6	√	Pos.	4	Unchanged	Grade 2 ILC 100mm diameter + all lymph nodes pos.
5	47	Poorly Differentiated IDC	7	√	Pos.	3	Partial Response	50mm high grade DCIS low invasive + all lymph nodes neg.
6	59	Poorly Differentiated IDC	3	√	Pos.	1	Partial Response	35mm grade 3 IDC, 3 pos. lymph nodes
7	47	IDC	3	√	Pos.	3	N/A	NA

*Patient 1 had a calcification that could be used as the image landmark so a coil was not used

Scanning Protocol

Patients were scanned just prior to receiving their chemotherapy treatment (~once every 3 weeks), thus mitigating any stress or inconvenience due to extra hospital visits. The scan itself consisted of taking a sequence of RF data, under compression/

decompression in both sagittal and transverse planes. Patients were asked to take standard resting positions for a conventional ultrasound scan (lying on their backs on an elevated examination table). Since patients were arriving just prior to their chemotherapy treatment, time was limited to ~10-15 min per session meaning that undue repeated scanning acquisitions was not a practical option.

To ensure consistent monitoring of the same region of interest (ROI) over the many months of treatment, patients were fitted with acoustically visible coils made from medical grade wiring to serve as imaging landmarks (Figure 7.1). These coils assist surgeons and radiologists in locating tumour and residual tumour areas post treatment. In some cases, these coils took up a significant portion of the tumour area itself. As these coils are considerably stiffer than any soft tissue (tumour or otherwise), the effects they would have on the strain distribution were of concern (method for segmenting coil?). The effects would be expected to be more pronounced in smaller tumours (or tumours that had shrunk during the course of treatment). In larger tumours (or tumours at the early stages of treatment, the effects would be mitigated. In the case of P1, a naturally occurring calcification was used as an imaging landmark.

The coil does provide a constant feature in a series of images where changes are expected to occur, therefore its effects may be limited and would probably vary case by case.

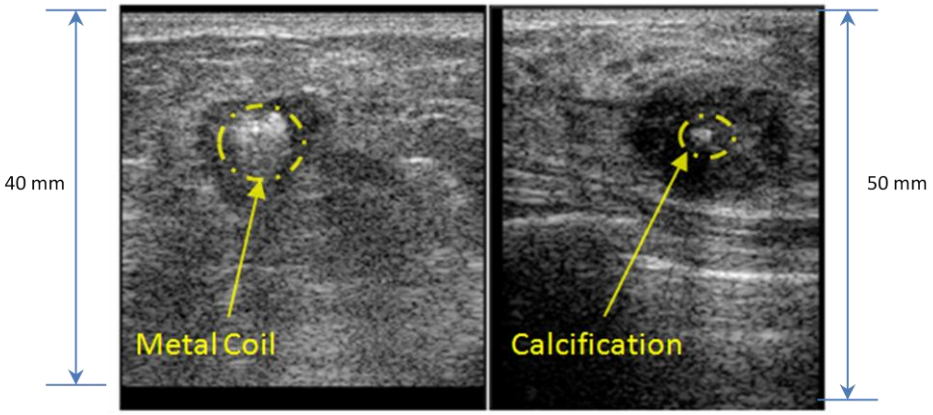


Figure 7.1- (left)P6 with coil fitted. (right)P1 with calcification used as landmark throughout the study

7.2.3 Patient Dropouts\Exclusions

Of the 7 patients, 2 (P6,P7) left the study to continue treatment at another hospital centre. Only lymph nodes could be imaged in P2. P4 and P3 had a relatively fast response to their chemotherapy, meaning that only a 'before and after' set of images could be obtained; any subtle changes in tumour response could not be interpolated. In the end, only 2 datasets met initial criteria set out for the study (P1,P5).

7.2.4 Imaging and Metrics (Post Processing)

Maintaining a constant set of image acquisition parameters over multiple scanning sessions using freehand techniques would be practically impossible. Strain images themselves can only be used to infer *relative* stiffness of tissues. The patient's posture during scanning, the pressure and angle at which the radiologist's applies the probe and resulting stress on the tissue are all sources of variability in these experiments. Moreover, chemotherapy over the course of many weeks can affect a patient's weight

(up or down) which can alter the overall stiffness of breast tissue. (The constancy of breast tissue stiffness could not be assumed).

Consequently, any method to describe pathological changes seen over a sequence of strain images would have to be in relative terms (i.e. a ratio). Chapter 4 provided a means to normalise images relative to the average strain present in the tissue. Image normalization plays a particularly key role in providing consistent colour mapping of strain data which is essential for its proper interpretation.

Though changes may be readily visible in the strain images, a quantification of the change would provide additional help to the analysis. It is hypothesized that the tumour/stromal response to a successful treatment of chemotherapy would result in a spread in the distribution of stiffness due to cancer cell necrosis and fibrosis in the peritumour regions. From this, the ratio of average stiffness outside the tumour to that inside was chosen as one possible measure of chemotherapy response [15]. One would expect this ratio to begin at some number >1 (given the tumour is most likely stiffer than it surrounding tissue prior to treatment) and approach ~1 if chemotherapy is successful, as tumour cells disintegrate and scaring of the peritumour region takes effect.

By comparison, sizing of the tumour is the conventional clinical practice for gauging tumour response as well as suitability for future surgical treatment options. Sizing in ultrasound B-mode involves a coarse B-mode segmentation (max depth and width of the lesion), typically focused on the hypoechoic region.

The strain ratio metric

Several assumptions are necessary to use a metric like the strain ratio:

The strain ratio metric is dependent on delineation of the tumour and peritumour regions; a particularly difficult task given that, as shown in Chapter 6, the extent of tumours is not always clearly visible in standard B-mode. Outside the hypoechoic region, tumour cells may still be present and visible (by their stiffness) in elastograms. Statistical evidence in Chapter 6 (that indicates elastography tends to overestimate tumour size) would suggest that there is a good chance these regions (outside the hypoechoic region but still exhibiting high stiffness) are composed of a combination of tumour and stromal cells, possibly still in a intermediary state; it is this region that is the transition zone between healthy and malignant tissue.

It was therefore decided to segment the hypoechoic region in the B-mode image as tumour (which could be done with high certainty). Tissue outside would be labelled peritumour; whether or not it contained tumour cells, the strain ratio would still be expected to change along the prescribed lines.

The strain ratio is also dependant on the size selected to delineate the outer boundaries of the peritumour region. In this case, the extent of peritumour region was set at baseline (from the first scanning session data) and held fixed throughout. Whatever the makeup of the tumour, it was supposed the baseline parameters provided some consistency over time. To test this assumption a sensitivity analysis was conducted to see how the output might be affected.

7. 3 RESULTS

7.3.2 Results from Tumour Response

A complete dataset

Figures 7.2 and 7.3 show the elastograms and B-mode over the 7 cycles of chemotherapy in both the transverse and sagittal plane respectively, for P1.

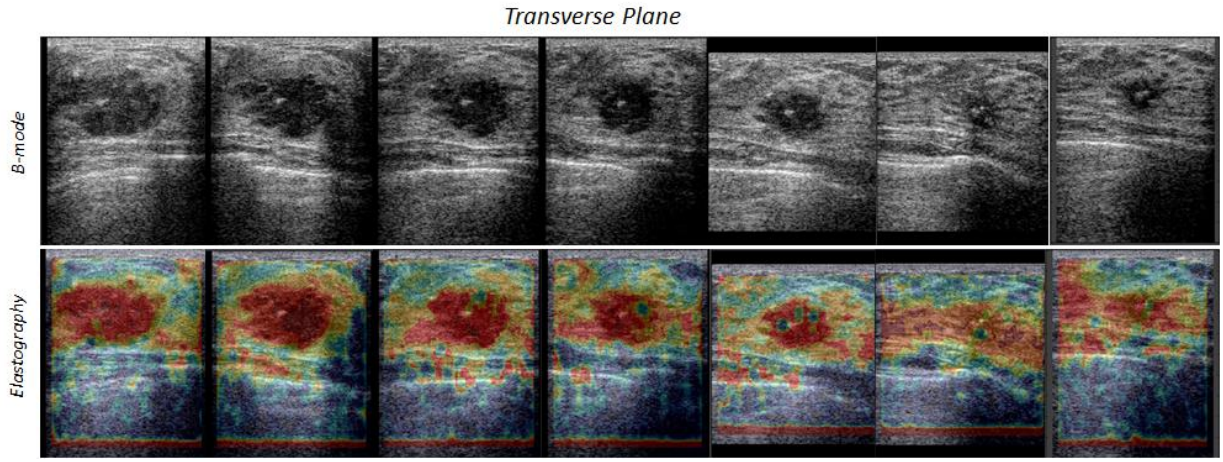


Figure 7.2- P1 dataset, transverse plane. Images taken over 7 cycles of chemotherapy. Note the gradual spread of strain relative to the hypoechoic region in the B-mode image

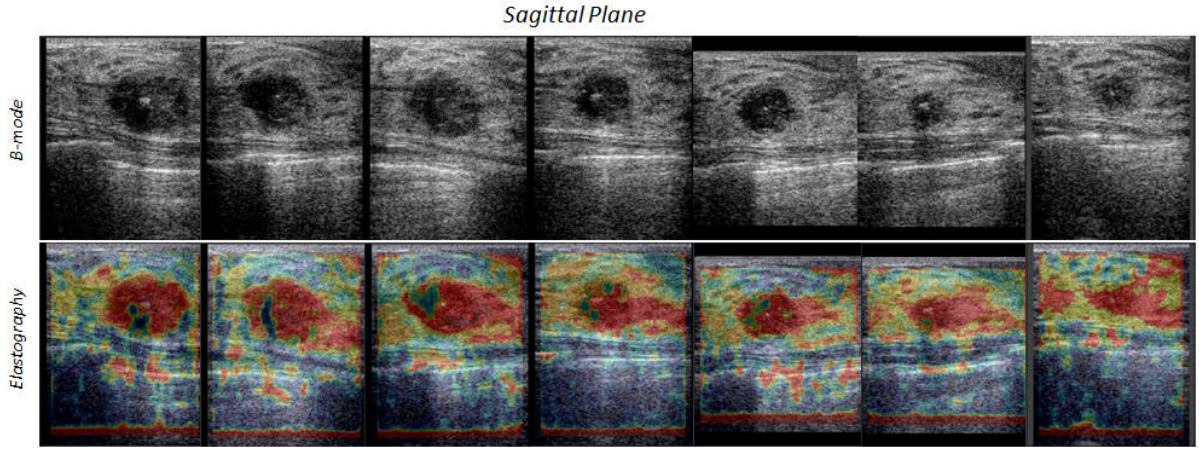


Figure 7.3- P1 dataset, sagittal plane Images taken over 7 cycles of chemotherapy. As with the images taken in the transverse plane, note the gradual spread of strain relative to the hypoechoic region in the B-mode image

In the baseline images, both the hypoechoic and low strain (red) regions are in good agreement. This clearly changes over the course of treatment leading to a discernable spread/redistribution of strain relative to the hypoechoic region of the B-mode image; the acoustic and mechanical properties of the tissue have deviated from one another.

In an attempt to quantify the spread of change in distribution of tissue stiffness, images were segmented in B-mode (delineated by the hypoechoic region) and tumour and peritumour regions were segmented as per Figure 7.4. The ratio of average peritumour strain over average tumour strain is plotted in Figure 7.5(a). The outer boundary limit of the peritumour region was selected to be 190% of the average tumour radius (this was later altered to assess the sensitivity) of the baseline image and held fixed over all subsequent images to try and encompass as much of the same tissue each scan. For comparison with conventional sizing analysis, Figure 7.5(b) shows the tumour size (mm^2) over the same period.

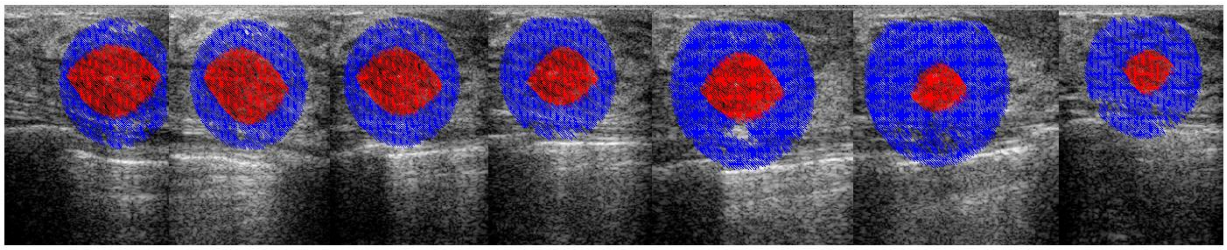


Figure 7.4- Tumour (red) and Peritumour (blue) regions from sagittal plane. The size of the peritumour region was kept fixed at twice the initial average radius of the tumour (i.e. taken from the first image in the sequence). Note: the 5^{th} and 6^{th} images from the left appear to have a larger segmented region; this is due to slightly different imaging parameters. Imaging depth was set to 40mm for theses two images. The rest were imaged with a depth of 50mm, hence the difference in apparent size.

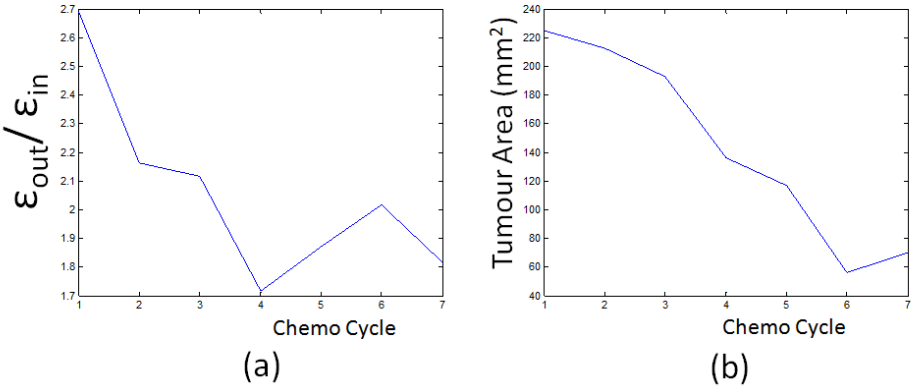


Figure 7.5-(a) Ratio of average peritumour strain over average tumour strain. (b) Tumour size (mm^2) as measured from the sagittal plane

The same analysis was done in the transverse plane (Figure 7.6).

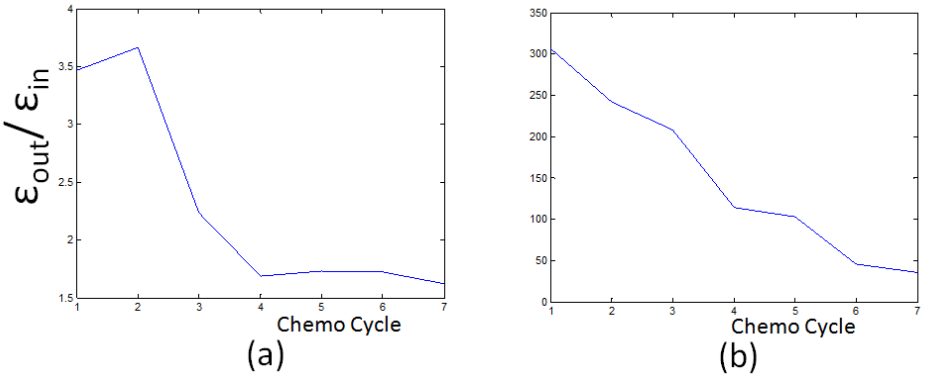


Figure 7.6- (a) Ratio of average peritumour strain over average tumour strain. (b) Tumour size (mm^2) as measured in the transverse plane

In both planes (essentially two separate, independent experiments), the overall change in tumour area (or size) was gradual over the course of 7 chemotherapy cycles. Certainly in the first 2-3 cycles, visual perception of size changes in the B-mode images is exceedingly difficult. In contrast, the strain ratio undergoes a much more rapid change over the first 3 cycles.

Sensitivity of ratio

The tumour delineation relies on manual segmentation. The peritumour extent was chosen somewhat arbitrarily; the main consideration was to include as much of the peritumour as possible without including obvious unrelated tissue found in the extreme margins of the image. It was therefore necessary to examine how the strain ratio was affected by any change to this limit.

In the first experiment, the tumour delineating points where adjusted by increasing (and later decreasing) them by 1mm (in the radial direction, with respects to the tumour centre); making the final segmentation of the tumour slightly larger or smaller. The resulting strain ratio was compared to that from the original segmentation; though some deviation is present, the general trend of the strain ratio is retained. Initially, the increase in tumour segmentation size causes a drop in the strain ratio with respects to the original sizing, and a decrease causes a rise in the strain ratio. This was expected as incorporating more tissue along the tumour boundary would most likely mean that non-tumour (and consequently softer) tissue would drive the average tumour strain down. Conversely, creating a smaller boundary for the tumour would drive the average strain inside it up. As the tumour responded to treatment and shrank in size, the behaviour of the strain ratio becomes less predictable and more prone to error due to the fact that fewer and fewer pixels are representing the lesion.

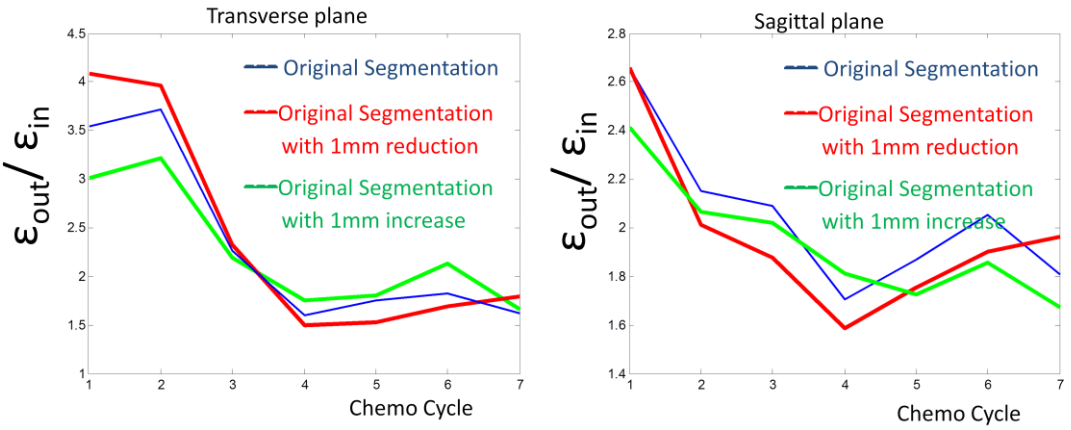


Figure 7.7- Introduction of +/- 1mm error in the tumour segmentation coordinates to evaluate strain ratio sensitivity to segmentation error

Next, the outer boundaries of the peritumor region were adjusted (see Figure 7.8) to include significantly less and significantly more area compared to the original parameters. Again, the general trend of the strain ratio is unaffected but the absolute values of the ratio differ by as much as 40%. Since, this ratio is used to monitor change, it is the trend that is significant.

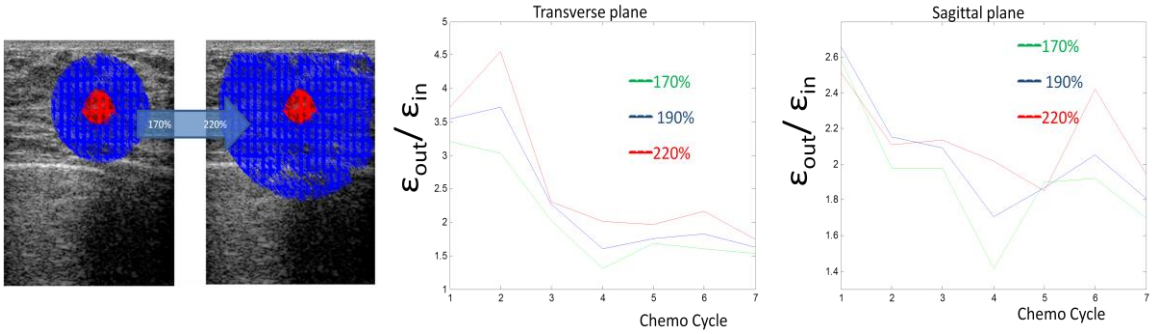


Figure 7.8- (left) Highlights the difference in size of the overall region.(right) Shows the effect on the strain ratio. Overall trend remain with some variation.

7.3.3 Additional Cases

Figure 7.9 spans the complete chemotherapy treatment of P5. Severe signal attenuation in the tumour meant that anomalies occurred in the strain patterns making interpretation difficult (Figure 7.10). However, it is clear that very little change occurred in terms of tumour size until after the 5th chemo cycle where dramatic effects are evident in both B-mode and strain images.

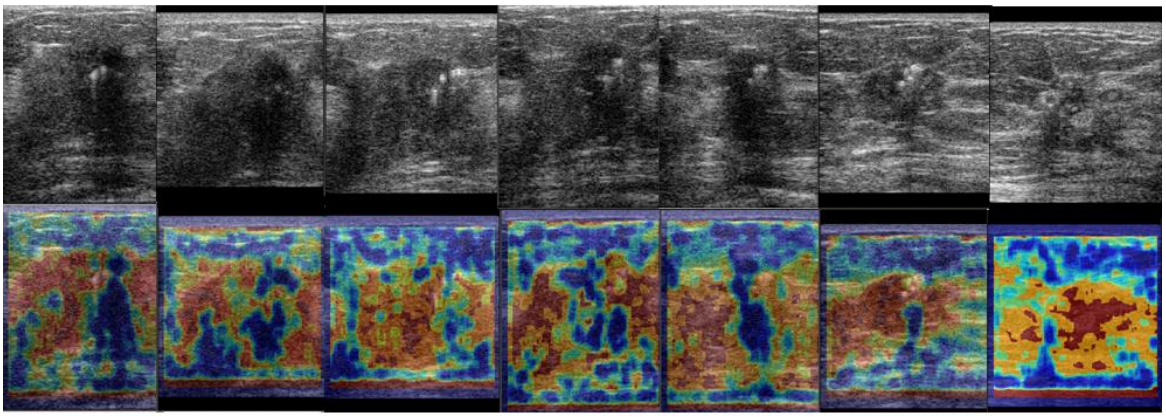


Figure 7.9- P5, 7 scan sessions. Very little reaction or change in tumour size is apparent until after the 5th cycle of chemotherapy. Note, the first image in this sequence is a baseline (before chemo). Thus, dramatic shrinking in the tumour shows up in the 6th image, taken just prior to the 6th chemotherapy treatment.

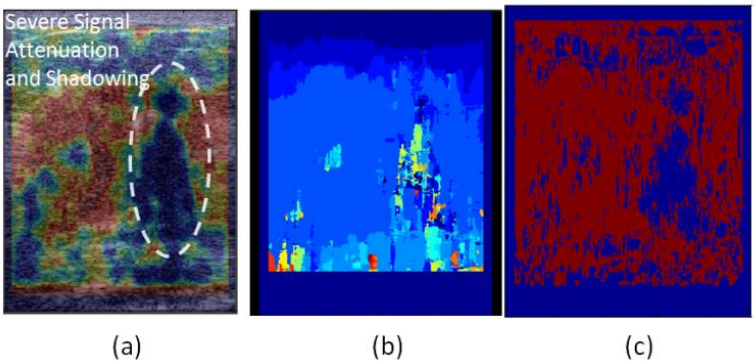


Figure 7.10- (a) Strain Image, (b) Axial Displacement Field (c) Strain Estimate Mask for first image in sequence of Figure 7.9

The strain ratio metric (Figure 7.11(a)) in this case is extremely difficult to interpret though the lack of change in any particular direction is consistent with lack of response to treatment experienced by the patient. In the end, P5 had only a partial response to chemotherapy an had a total mastectomy.

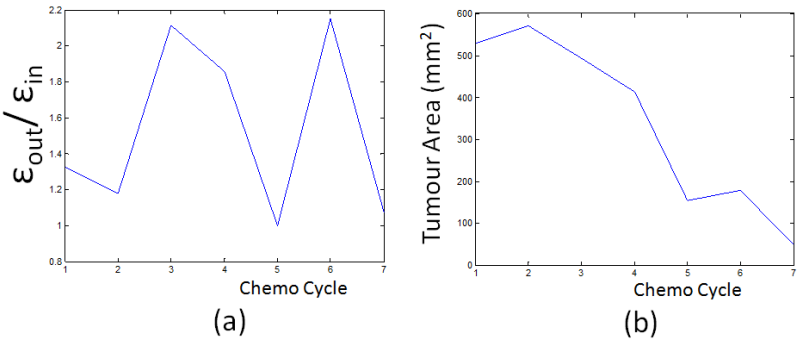


Figure 7.11- (a) Ratio of average peritumour strain over average tumour strain. (b) Tumour size (mm^2)

Incomplete Data Sets

Figure 7.12 shows how quickly a tumour can respond to treatment; after only 2 cycles of chemotherapy all that remains visible is the coil implant.

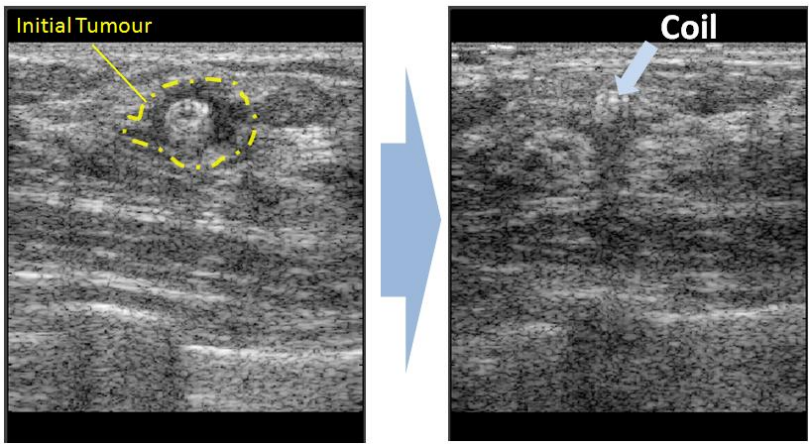


Figure 7.12- 1st and 3rd scan of patient P3: only the coil remains (6 weeks apart)

Figure 7.13 shows the change in strain patterns over the first 3 cycles of chemotherapy. The B-mode exhibits marginal changes in the tumour size. The strain ratio metric was calculated despite the lack of a full data set and is depicted in Figure 7.14. In this case, visual interpretation of tumour spread may prove a better choice of analysis since there clearly was insufficient data points to analyse. Patient 6 ultimately did not respond to chemotherapy treatment.

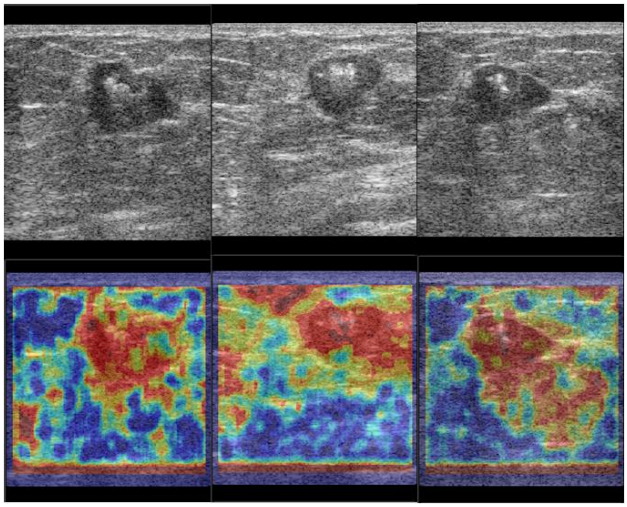


Figure 7.13-P6 3 sessions of tumour response: change in size from B-mode data is small, strain data is inconclusive.

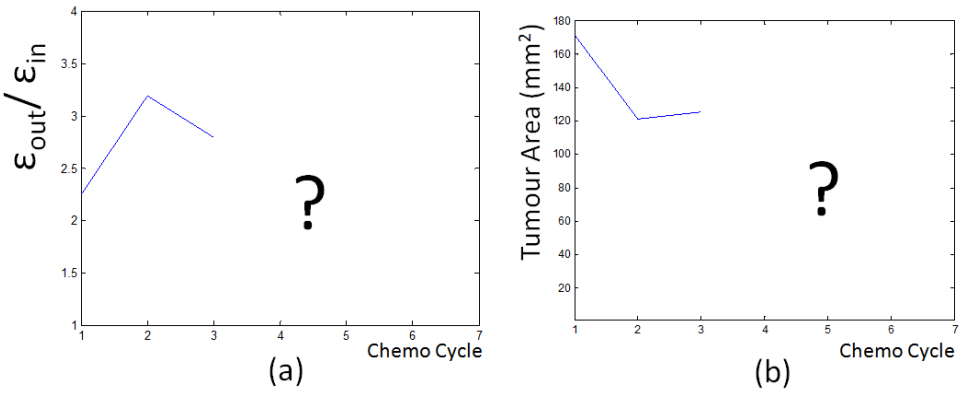


Figure 7.14- Ratio of average peritumour strain over average tumour strain. (b) Tumour size (mm^2). Insufficient data is present to interpolate the final result

Lymph Nodes

The effects of chemotherapy on lymph nodes was of particular interest because they may provide supplementary indication of treatment response; moreover these results can be obtained during treatment (rather than having to wait for pathology reports after surgical excision) and can be obtained non-invasively, in vivo via standard B-mode scanning. Consequently, the results from 2 patients are shown below. In both cases the gradual shrinking of the node is apparent; due primarily by cancer cell death.

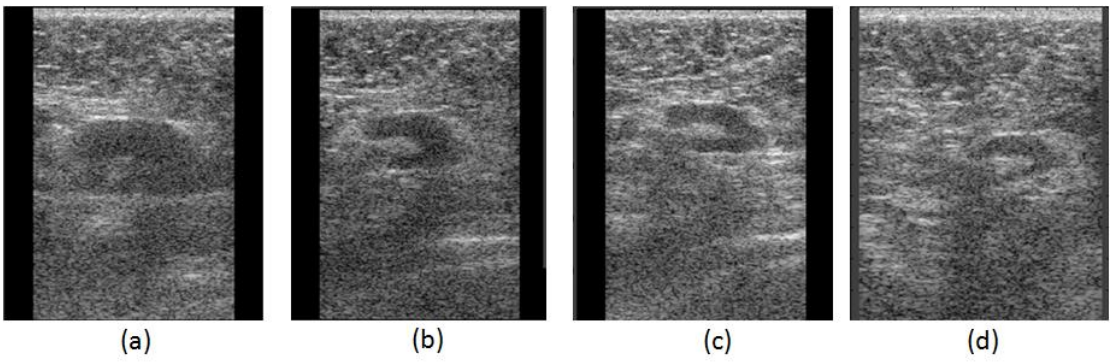


Figure 7.15(a)-The gradual shrinking of lymph nodes during neoadjuvant chemotherapy after (a) 1, (b) 3, (c) 4 and (d) 6 chemotherapy cycles P4

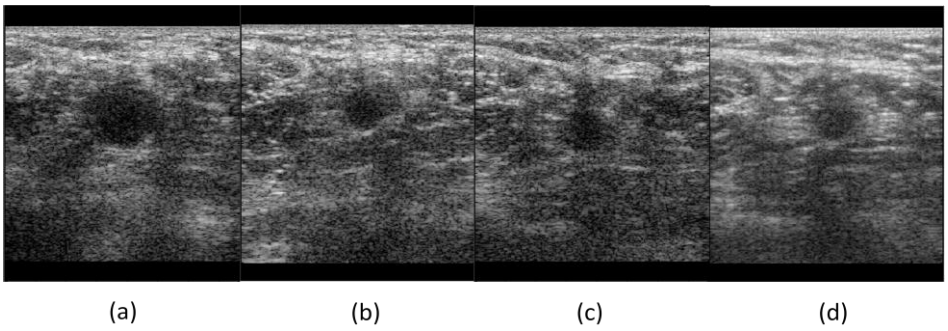


Figure 7.15(b)-The gradual shrinking of lymph nodes during neoadjuvant chemotherapy after (a) 2, (b) 3, (c) 4 and (d) 5 chemotherapy cycles P3

Elastography of lymph nodes provided a particular challenge. The lymph node sinus has extremely poor speckle correlation; by default the strain algorithm tends to calculate

unrealistically high strain values for these regions, hence the dark blue colouring in the image. In Chapter.4 an algorithm was developed to identify poor strain estimates. The binary mask produced from this algorithm is shown in Figure 7.16(b); any measurement taken within the sinus would not be reliable. The signal decorrelation present within a lymph node is yet again depicted in Figure 7.17 in another patient.

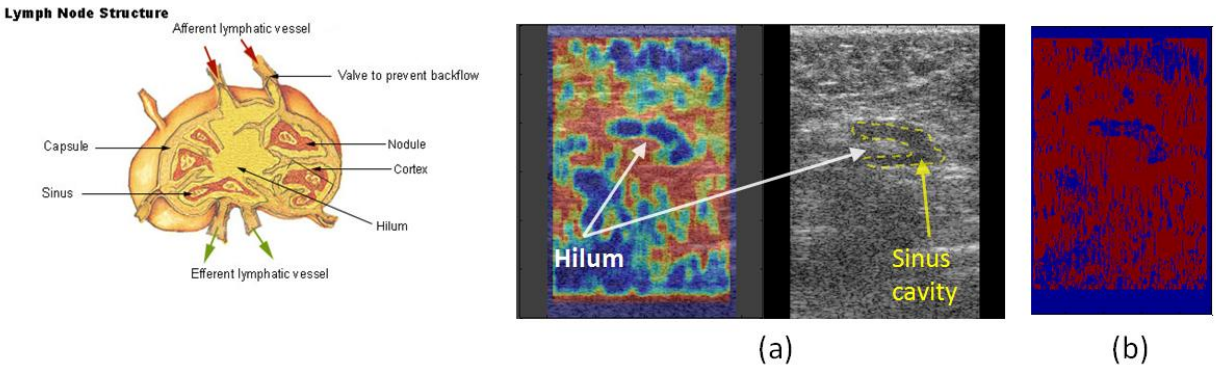


Figure 7.16-The sinus cavity of the lymph node produces poor strain estimates. (a) B-mode and strain images. (b) Binary mask for identifying poor strain estimates (blue indicates poor estimates) Lymph node diagram from: http://www.wereyouwondering.com/what-is-the-smallest-organ-in-the-human-body/

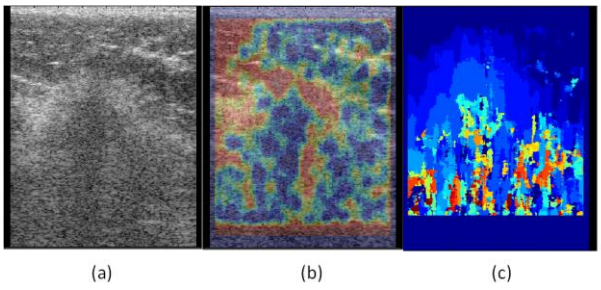


Figure 7.17-A large lymph node of P2; (a)B-mode and (b)Strain image, and (c) axial displacement field which demonstrates the signal decorrelation in the form of a noisy displacement field

7.4 Discussion

In the case of P1, the use of relative strain ratios between tumour and peritumour regions not only indicated change due to therapy, it showed greater sensitivity compared to standard B-mode sizing. This is significant as it is in the first cycles of chemotherapy where one would like to assess the chemotherapy's effectiveness.

The chosen size of the peritumour region is a source of variability in the strain ratio. However, the general trends were found to be similar over a relatively large range of peritumour sizes; from including tissue just beyond tumour boundaries to including most of the image.

An attempt was made to provide some consistency in the calculation by asserting certain assumptions on the baseline image (like define definite tumour regions and correlating low strain with low echogenicity). Regardless of the accuracy of these assumptions, it provides a baseline that would change with some consistency over the course of treatment. Manual segmentation of the tumour region is a serious drawback of this method, however introducing reasonable amount of error to the measurements led to marginal changes to the overall ratio trend.

In summary, the strain ratio is a useful metric but difficult to calculate. Every effort was made in this study to provide a consistent and reliable grounds for implementing this metric. Results from 1 patient are encouraging, however more patient data is needed to make any conclusive remarks.

Qualitative image analysis was also made effective through the normalisation of strain images for consistent colour mapping which could be seen in all tumour images.

Incomplete data sets still provided insight into the behaviour of tumour and stroma during chemotherapy. We know from Figures 7.12 that tumour change can happen very rapidly; this was apparent from the B-mode data alone. Both B-mode and strain images in Figure 7.9 confirm that response to chemotherapy can happen very slowly as well.

It is clear that some of these cases could have been helped by scanning patients more frequently thus providing more data points to analyse. However, when patients show such a quick response to chemotherapy, the issue of treatment monitoring becomes somewhat of a moot point. From patients like P5, it is clear that some tumours are not well suited for ultrasound/elastography analysis; heavy attenuation and a tumour that did not initially fit within the probe footprint is problematic. Elastograhy data could be further improved by oversampling at each session (taking repetitive/redundant scans) but ultimately the proposed technique will not be suitable for all cases.

Coils did not play a significant role in the 2 complete data sets acquired however dealing with them may be as simple as segmenting and excluding them from any strain ratio calculation. Alternatively, these landmarks could be used to guide the clinician to an adjacent cross section of tissue, devoid of the coil itself, for imaging purposes.

Constraints on patient availability and time prevent a rigorous study to examine the techniques repeatability. However, scans of P1 were conducted in both sagittal and transverse planes providing similar results. Repeatability of freehand ultrasound elastography was demonstrated in Chapter 3. Moreover, Chapter 4 provide a method whereby the confidence in the strain measurement could be assessed as well as consistency in the colour mapping and presentation of elastograms. The multiple cases

presented in Chapte 6 and previous work [13] demonstrated that histology does indeed correlate with strain images. The point of these experiments was to instil confidence in using ultrasound elastography for these types of measurements.

Lymph nodes were able to provide corroborative evidence of change as in the case of P3. Lymph nodes were found to undergo gradual size changes during chemotherapy. Unfortunately, they were found to be unsuitable for strain imaging analysis. Nonetheless, they do provide supplementary evidence of a therapeutic response and further correlative studies with B-mode and elastography of breast lesions may provide more insight

7.5 Conclusion

It was seen quite clearly from histology results that a dramatic change in tissue composition can be observed after successful chemotherapy treatment (see Chapter 2: Figure 2.4, actual samples taken from P3). The large concentration of fibrosis, and the stiffness associated with these type of tissues, strongly suggests that ultrasound elastography is suited for the task of monitoring cancer therapy.

Moreover, unlike more sophisticated PET and MRI scans US can be used as often as necessary, safely and at low cost. It is also worth noting that the breast cancer neoadjuvant patients benefitted from participating in this study by receiving feedback after every scan on the size of their tumour. It was stressed to them by the radiologist that measurements were approximate and did not necessarily reflect a positive or negative prognosis, nor would they have any impact on their standard treatment. Nonetheless, patients (who generally receive little to know feedback while undergoing

gruelling chemotherapy) found the scans to have an overall positive psychological effect.

Lymph nodes were found to provide some insight into cancer therapy effectiveness; namely they tend to shrink back to normal size as a result of successful treatment. However, in the limited number of cases presented in this chapter, the shrinking was too gradual and too late into treatment to provide a good initial prognosis for chemotherapy. Moreover, lymph nodes proved wholly unsuitable for elastography owing to ultrasound signal attenuation and shadowing.

The potential of this research is indeed great. Its future will involve overcoming particular challenges. The method is limited by tumour size (that can be practically scanned with a standard probe) and shadowing. Moreover, the strain distribution may be better described by a less user-dependant metric than the strain ratio; this should be a major focus of future work. In addition, more complete histology (possibly in conjunction with lymph node scanning) would provide a more complete picture and further support elastography findings.

Chapter 8
Summary & Future Work

Summary

The hypothesis set out by this thesis was to determine if ultrasound elastography could be used as a helpful clinical tool in breast cancer therapy. It was from an engineering approach that this project was tackled; identify the problem and find the best solution.

The problem was that clinicians lacked a full picture of what takes place in breast cancer. Moreover, they needed investigative methods which would ideally be non-invasive and cost effective. The virtues of ultrasound imaging for this task over other modalities was hopefully well established in the discussion of Chapter 2.

Also, the simpler the overall design of the solution, the more likely it would eventually be taken up in the real clinical world. It was with this in mind that a new elastograpahy algorithm in Chapter 3 and image display techniques in Chapter 4 were developed.

The design of the strain algorithm was centred around computational efficiency (for quick results) and robustness (to cope with freehand acquisition of a wide range of patient data). No parameters needed adjusting for any of the images presented in this thesis and images were displayed with relative consistency in their colour mapping; a property which has great significance to a radiologist. It was also essential for the subsequent data analysis in Chapter 6 and Chapter 7, sizing of tumours and monitoring changes over time.

Chapter 5 took advantage of a valuable property of ultrasound; a high frame rate. With a good strain algorithm already developed, it was only logical to explore strain vs. time relationships of tissue and HYFIVE was the result.

At all times, the work presented in this thesis has been steered by a single goal of improving breast cancer therapy. To summarize some of this thesis' achievements:

- A new efficient block matching algorithm for displacement tracking
- An efficient and robust spectral shift estimator for strain calculation
- A novel probe canister design for viscoelasticity measurements
- A technique for image normalization and display for consistent subsequent image interpretation

All of which resulted in tumour sizing which outperformed conventional B-mode in both accuracy and precision in addition to new imaging techniques which may help uncover the underlying processes of tumour structure and chemotherapy response.

Future Work

3D Elastography

One initial goal of this project was to evaluate the use of 3D ultrasound probe technology in ultrasound elastography. As discussed in Chapter 3, the obstetrics C8-3 3D probe from Zonare proved unsuitable for clinical use in breast cancer due primarily to its poor resolution and extremely slow data transfer rate.

A better research package would have helped solve the latter. Simply allowing the memory buffer to store at least *two* 3D volumes at the same time would have made a significant difference in the quality of the clinical data obtained.

3D volumes would have also solved other limitations of this study; better sizing and motion tracking being an obvious gain. Though the right probe for the job was not selected in this case, it was shown that under controlled conditions (as in the CIRS phantom experiments) good quality strain images could be achieved.

The main challenges to overcome for 3D elastography are thus related to hardware and scanning protocol; the strain algorithms themselves are reliable.

Probe Canister (HYFIVE)

The HYFIVE experiments were conducted with the notion of taking advantage of everything ultrasound imaging has to offer; namely a high frame rate. This opened the doors to examining mechanical properties of tissue beyond simply strain. An accurate measure of tissue viscosity had the potential of providing important insight into cancers, however the application of HYFIVE was not without its shortcomings.

Out of plane motion was the primary culprit; forcing clinicians to repeat scan acquisitions several times (often to no avail) to capture a reasonable set of data. As a clinical tool, HYFIVE needs much refinement.

Changes to the probe canister used in the HYFIVE system would help improve results. Allowing for a quick way to adjust the weight ring would help to compensate for the variation in breast tissue density and size. A slightly more ergonomic design would also help clinicians keep hold of it. On a hardware note, higher frame rates would be ideal as well to obtain more data points in the creep curve.

The potential for HYFIVE in breast cancer imaging is great, given the performance of quasi-static elastography in Chapter 6 and Chapter 7. A more in depth study with detailed histopathology would certainly be justified to help establish this new technology.

Tumour Sizing

Chapter 6 helped establish that tumour sizing was markedly improved when elastography was incorporated with B-mode, compared to standard B-mode alone. It would be of particular interest to follow up the initial tumour sizing study with a more in depth correlative study involving BI-RADs and breast density measures. The goal would be to ascertain if the different strain patterns and tumour behavior were related to the overall density and composition of the breast as the surrounding tissue may also may play an important factor in tumour proliferation. Indeed, this is the scientific basis for the neoadjuvant study of Chapter 7

NeoAdjuvant Study

Probably the most exciting and valuable implementation of ultrasound elastography is in monitoring the tumour response to neoadjuvant chemotherapy. Success in this field of research would have positive implications for doctors, drug developers and patients. A recently proposed project aims to further this research by including extensive histopathology to search for relevant cells types such as fibroblasts, collagen and proteins like Ki67 (thought to have connections with cell proliferation) [138]. An additional biopsy mid-way through therapy would also help confirm elastography results. This correlative study between elastography and histology would help reveal more insight into tumour/stroma reaction and could lead to new clinical tools like the strain ratio metric in Chapter 7.

Additional requirements would be to have more patients and to scan them more frequently so that crucial data points are not missed. It would also be useful to explore

more powerful image registration techniques to help compare strain images and more accurately quantify the changes observed.

What is most encouraging about this research is that the overall concept is actually quite straightforward, the equipment required is readily available and the costs and time required is low. Consequently, the technique has a good chance in future of becoming a standardize clinical technique.

This is significant as it has also been an aim in this thesis to develop truly practical techniques that others would benefit from; which would hopefully keep this manuscript from collecting dust on a quiet shelf. The future of ultrasound elastography remains secure as long as researchers continue to find innovative applications for this outstanding technology.

Appendix A

Coordinates Systems in Medical Imaging

This appendix provides a quick reference to some of the terminology used when defining coordinates and planes in medical imaging.

- The 3 planes of an Ultrasound probe

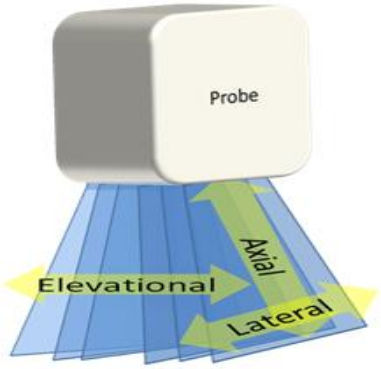
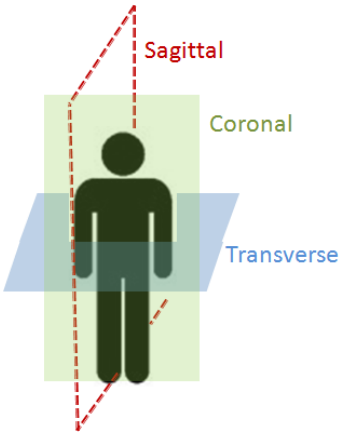


Figure A.1

- Sagittal, Transverse and Coronal planes and the relative image coordinate nomenclatures



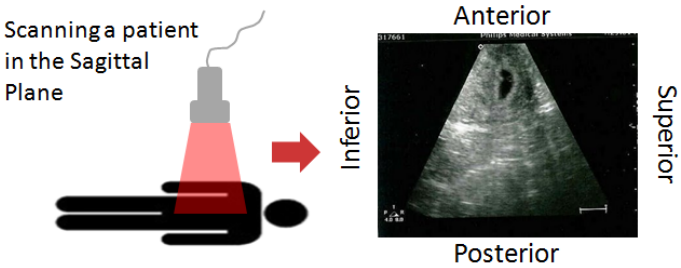


Figure A.2

Appendix B

Area Measurements Using Polygon Decomposition Method

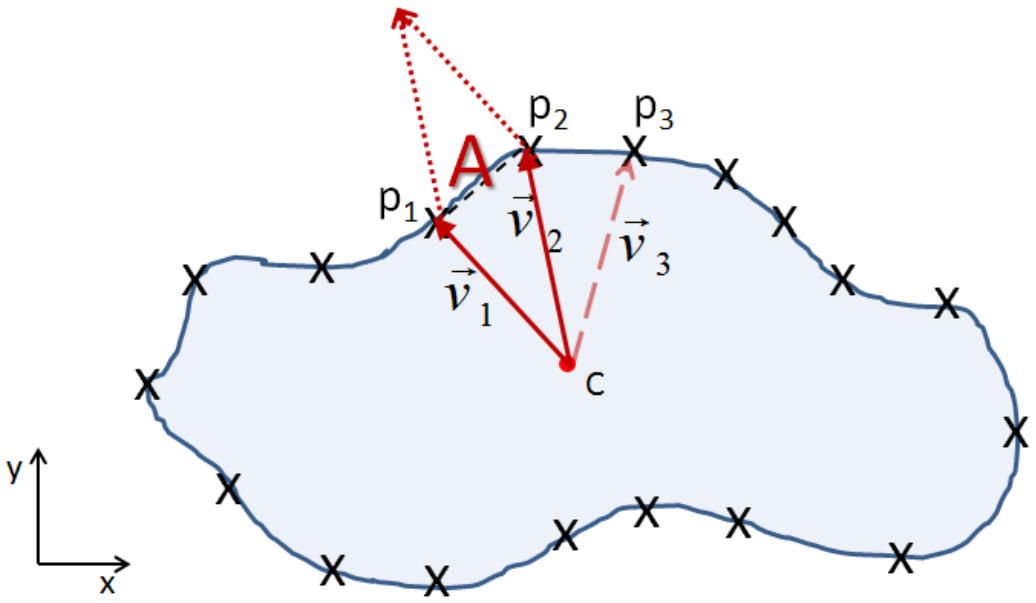


Figure B.1- Illustration of Polygon Decomposition Method

Consider the cloud like shape in the figure above. Its area is delineated by a series of points (marked as 'x') around its boundary. Taking any point ***c*** (Note: it need not be anywhere near the centre or even inside the boundaries!), the signed area, ***A***, of the parallelogram can be measured by

$$A = \overrightarrow{v1} \times \overrightarrow{v2} = (p_1 - c) \times (p_2 - c)$$

This actually results in a *scalar* quantity for ***A*** because we force all the points, p_1,p_2 and *c*, to lie in the *xy*-plane, that is:

$$\overrightarrow{p_1} = \begin{pmatrix} p1_x \\ p1_y \\ 0 \end{pmatrix}, \overrightarrow{p_2} = \begin{pmatrix} p2_x \\ p2_y \\ 0 \end{pmatrix}, \vec{c} = \begin{pmatrix} c_x \\ c_y \\ 0 \end{pmatrix}$$

The resulting cross product then simplifies to

$$A = (p1_x - c_x)(p2_y - c_y) - (p2_x - c_x)(p1_y - c_y)$$

The portion of the parallelogram that lies inside our cloud-like shape can then be approximated as *A/2*.

By repeating this procedure using adjacent points, $\vec{v}_2$ and $\vec{v}_3$ and so on, the entire area can be measured. The more points used, the better the approximation. The final sign of the total area, $\boldsymbol{A_{total}}$, will depend on whether one proceeds clockwise or anti-clockwise. However, it is essential to hold off taking the absolute value of the *A's* until the total signed area is computed. This allows for any type simple polygon (convex and concave) to be measured as areas where parallelograms overlap will add up and cancel out as appropriate.

REFERENCES

[1] Varghese, T.; Ophir, J.; Konofagou, E.; Kallel, F. & Righetti, R.
Tradeoffs in elastographic imaging
Ultrasonic Imaging, **2001**, *23*, 216-248

[2] Doyley, M. M.; Bamber, J. C.; Fuechsel, F. & Bush, N. L.
A freehand elastographic imaging approach for clinical breast imaging: system development and performance evaluation
Ultrasound in Medicine & Biology, **2001**, *27*, 1347–1357

[3] Egorova, V.; Tsyuryupaa, S.; Kaniloa, S.; Kogita, M. & Sarvazyana, A.
Soft tissue elastometer
Medical Engineering and Physics, **2008**, *30*, 206-212.
(doi:10.1016/j.medengphy.2007.02.007)

[4] Alam, S. K.; Ophir, J. & Konofagou, E. E.
An adaptive strain estimator for elastography
IEEE Transactions on Ultrasonics, Ferroelectrics, and Frequency Control, **1998**, *45*, 461-472

[5] Nitta, N.; Yamakawa, M.; Shiina, T.; Ueno, E.; Doyley, M. M. & Bamber, J. C.
Tissue elasticity imaging based on combined autocorrelation method and 3-D tissue model
IEEE Ultrasonics Symposium, **1998**, 1447-1450

[6] Rivaz, H.; Boctor, E.; Foroughi, P.; Zellars, R.; Fichtinger, G. & Hager, G.
Ultrasound Elastography: A Dynamic Programming Approach
IEEE Transactions on Medical Imaging, **2008**, *27*, 1373-137

[7] Treece, G.; Lindop, J.; Chen, L.; Housden, J.; Prager, R. & Gee, A.
Real-time quasi-static ultrasound elastography
Interface Focus, **2011**, (doi:10.1098/rsfs.2011.0011)

[8] Parker, K. J.; Doyley, M. M. & Rubens, D. J.
Imaging the elastic properties of tissue: the 20 year perspective
Physics In Medicine And Biology, **2011**, *56*, 1-29

[9] Duenwald, S.; HirohitoKobayashi; KaytFrisch; RodericLakes & RayVanderbyJr
Ultrasound echo is related to stress and strain in tendon
Journal of Biomechanics, **2011**, *44*, 424-429

[10] Deffieux, T.; Montaldo, G.; Tanter, M. & Fink, M.
Shear wave spectroscopy for in vivo quantification of human soft tissues viscoelasticity
IEEE Transactions on Medical Imaging, **2009**, *28*, 313-322

[11] Wellman, P. S.; Howe, R. D.; Dalton, E. & Kern, K. A.
Breast tissue stiffness in compression is correlated to histological diagnosis
Harvard BioRobotics Laboratory, **1999**,
http://biorobotics.harvard.edu/pubs/1999/mechprops.pdf

[12] Kadour, M. J.
Assisted-Freehand Ultrasound Elasticity Imaging of the Breast
Oxford University, **2007**

[13] English, R.; Li, J.; Parker, A.; Roskell, D.; Adams, R.; Parulekar, V.; Baldwin, J.; Chi, Y. & Noble, A.
A pilot study to evaluate assisted freehand ultrasound elasticity imaging in the sizing of early breast cancer: a comparison of B-mode and assisted freehand ultrasound elasticity ultrasound with histopathology measurements
The Journal of British Radiology, **2011**, *84*, 1011-1019

[14] Rao, M.
Shear strain elastography for breast cancer diagnosis
ProQuest, UMI Dissertation Publishing, **2011, ISBN-13: 978-1243529541**

[15] Zhi, H.; Xiao, X.; Yang, H.; Ou, B.; Wen, Y. & Luo, B.
Ultrasonic elastography in breast cancer diagnosis: strain ratio vs 5-point scale
Academic Radiology, **2010**, *17*, 1227-1233

[16] Ophir, J.
New medical imaging technique improves chances of early cancer detection
Algor., **June 16, 1998**, http://www.algor.com /news_pub/cust_app/cancer /cancer.asp

[17] MSNBC.com
Elastogram' instantly diagnoses breast cancer
Dec. 1, 2006, http://www.msnbc.msn.com/id/15990645

[18] Hitachi Medical Systems Ultrasound elastography
*[online] http://www.hitachi-medical.com.sg/products/elastography.html,***2011**

[19] Siemens
Case study: Elastography detects isoechoic breast cancer
Healthcare News, **16 August, 2011**

[20] Friedrich-Rust, M.; Ong, M.-F.; Herrmann, E.; Dries, V.; Samaras, P.; Zeuzem, S. & Sarrazin, C.
Real-time elastography for noninvasive assessment of liver fibrosis in chronic viral hepatitis
American Journal of Roengenology, **2007**, *18*, 758-764

[21] Dudea, S. M.; Giurgiu, C. R.; Dumitriu, D.; Chiorean, A.; Ciurea, A.; Botar-Jid, C. & Coman, I.
Value of ultrasound elastography in the diagnosis and management of prostate cancer
Medical Ultrasonography, **2011**, *13*, 45-53

[22] Chopra, R.; Huang, A. A. Y.; Musquera, M.; Wachsmuth, J.; Bronskill, M. & Plewes, D.
In vivo MR elastography of the prostate gland using a transurethral actuator
Magnetic Resonance Medicine, **2009**, *62*, 665-671

[23] Carrión, J. A.; Navasa, M. & Forns, X.
MR elastography to assess liver fibrosis
Radiology, **2008**, *247*, 591-592

[24] McKnight, A. L.; Kugel, J. L.; Rossman, P. J.; Manduca, A.; Hartmann, L. C. & Ehman, R. L.
MR elastography of breast cancer: preliminary results
American Journal of Radiology, **2002**, *178*, 1411-1417

[25] Dighe, M.; Bae, U.; Richardson, M. L.; Dubinsky, T. J.; Minoshima, S. & Kim,Y.
Differential diagnosis of thyroid nodules with US elastography using carotid artery pulsation
Radiology, **2008**, *248*, 662-669

[26] Goddi, A.; Sacchi, A.; Magistretti, G.; Almolla, J. & Salvadore, M.
Real-time tissue elastography for testicular lesion assessment
Eur. Radiology, **2011**

[27] Weinberg, R. A.
Science, G. *(Ed.)*
The Biology of Cancer
Taylor & Francis Group, **2007**

[28] American Cancer Society, What is breast cancer?
2012 ,
http://www.cancer.org/docroot/CRI/content/CRI_2_4_1X_What_is_breast_cancer_5.asp

[29] Breakthrough Breast Cancer, Are all lumps cancer?
http://www.breakthrough.org.uk/about_breast_cancer/understanding_breast_cancer/are_all_lumps.html

[30] Arpino, G.; Bardou, V. J.; Clark, G. M. & Elledge, R. M.
Infiltrating lobular carcinoma of the breast: tumor characteristics and clinical outcome
Breast Cancer Research, **2004**, *6*, 149-156

[31] Samani, A.; Zubovits, J. & Plewes, D.
Elastic moduli of normal and pathological human breast tissues: an inversion-technique-based investigation of 169 samples
Physics In Medicine And Biology, **2007**, *52*, 1565-1576

[32] Sinkus, R.; Bercoff, J.; Tanter, M.; Gennisson, J.-L.; Khoury, C. E.; Servois,V.; Anne Tardivon & Fink, M.
Nonlinear viscoelastic properties of tissue assessed by ultrasound
IEEE Transactions on Acoustics, Speech and Signal Processing, **2006**, *53*, 2009-2018

[33] NHS Cancer Screening Programmes, Breast screening resource pack for training primary care nurses
NHSBSP Publication, **2003**, *39*

[34] NHS Cancer Screening Programmes, Consolidated Guidance on Standards for the NHS Breast Screening Programme
NHSBSP Publication, **2005**, *60*, ISBN 1 84463 022 6

[35] Richards, M. S.; Feldman, J.; Smith, R. A. & DeBuono, B. A.
Breast biopsy rate and positivity in Rhode Island
American Journal of Public Health, **1994**, *84*, 1310-1312

[36] Moon, W.; Huang, C.; Shen, W.; Takada, E.; Chang, R.; Joe, J.; Nakajima, M. & Kobayashi, M.
Analysis of elastographic and B-mode features at sonoelastography for breast tumor classification
Ultrasound in Medicine & Biology, **2009**, *35*, 1794-1802

[37] Thomas, A.; Fischer, T.; Frey, H.; Ohlinger, R.; Grunwald, Z.; Blohmer, J.-U.; Winzer, K.-J.; Weber, S.; Kristiansen, G.; Ebert, B. & Kümmel, S.
Real-time elastography — an advanced method of ultrasound: first results in 108 patients with breast lesions
Ultrasound in Obstetrics & Gynecology, **2006**, *28*, 335–340

[38] Krouskop; Wheeler; Kallel; Garra & Hall
Elastic moduli of breast and prostate tissues under compression
Ultrasonic Imaging, **1998**, *20*, 260-274

[39] Wells, P. N. T. & Liang, H.-D.
Medical ultrasound: imaging of soft tissue strain and elasticity
Journal of the Royal Society: Interface, **2011**, *8*, 1521-1549

[40] Eberl, M. M.; Fox, C. H.; Edge, S. B.; Carter, C. A. & Mahoney, M. C.
BI-RADS classification for management of abnormal mammograms
Journal of the American Board of Family Medicine, **2006**, *19*, 161–164

[41] White, J.
Breast density and cancer risk: What is the relationship?
Journal of the National Cancer Institute, **2000**, *92*, 443

[42] Irwin, M. L.; Aiello, E. J.; McTiernan, A.; Bernstein, L.; Gilliland, F. D.; Baumgartner, R. N.; Baumgartner, K. B. & Ballard-Barbash, R.
Physical activity, body mass index, and mammographic density in postmenopausal breast cancer survivors
Journal of Clinical Oncology, **2007**, *25*, 1061-1066

[43] Harvey, J. A. & Bovbjerg, V. E.
Quantitative assessment of mammographic breast density: relationship withbreast cancer risk
Radiology, **2004**, *230*, 29-41

[44] Zhou, C.; Chan, H.-P.; Petrick, N.; Helvie, M. A.; Goodsitt, M. M.; Sahiner, B. & Hadjiiski, L. M.
Computerized image analysis: Estimation of breast density on mammograms
Medical Physics, **2001**, *28*, 1-14

[45] Budak, M.; Thomson, K.; Whelehan, P.; Vinnicombe, S. & Evans, A.
Correlations between shear wave elastography and mammographic findings in invasive breast cancer
Breast Cancer Research, **2011**, *13*

[46] National Cancer Institute, Adjuvant and neoadjuvant therapy for breast cancer
http://www.cancer.gov/cancertopics/factsheet/Therapy/adjuvant-breast

[47] Sawyers, C.
Targeted cancer therapy
Nature, **2004**, *432*, 294-297

[48] Marte, B.
Cell division and cancer
Nature, **2004**, *432*, 293-341

[49] Genentech USA, Inc., Who is Herceptin for?
http://www.herceptin.com/breast/

[50] MacMillan Cancer Support, Trastuzumab (Herceptin)
2010
http://www.macmillan.org.uk/Cancerinformation/Cancertreatment/Treatmenttypes/Biologicaltherapies/Monoclonalantibodies/Trastuzumab.aspx

[51] Pickles, M. D.; Lowry, M.; Manton, D. J.; Gibbs, P. & Turnbull, L. W.
Role of dynamic contrast enhanced MRI in monitoring early response of locally advanced breast cancer to neoadjuvant chemotherapy
Breast Cancer Research and Treatment, **2005**, *91*, 1-10

[52] Drew, P. J.; Kerin, M. J.; Mahapatra, T.; Malone, C.; Monson, J. R. T.; Turnbull, L. & Fox, J. N.
Evaluation of response to neoadjuvant chemoradiotherapy for locally advanced breast cancer with dynamic contrast-enhanced MRI of the breast
European Journal of Surgical Oncology, **2001**, *27*, 617-620

[53] Martincich, L.; Montemurro, F.; Rosa, G. D.; Marra, V.; Ponzone, R.; Cirillo, S.; Gatti, M.; Biglia, N.; Sarotto, I.; Sismondi, P.; Regge, D. & Aglietta, M.
Monitoring response to primary chemotherapy in breast cancer using dynamic contrast-enhanced magnetic resonance imaging
Breast Cancer Research and Treatment, **2004**, *83*, 67-76

[54] Roman-Goldstein, S.; Barnett, P.; McCormick, C.; Ball, M.; Ramsey, F. & Neuwelt, E.
Effects of gadopentetate dimeglumine administration after osmotic blood-brain barrier disruption: toxicity and MR imaging findings
American Journal of Neuroradiology, **1991**, *12*, 885-890

[55] Ray, D.; Cavanagh, J.; Nolan, C. & Williams, S.
Neurotoxic effects of gadopentetate dimeglumine: behavioral disturbance and morphology after intracerebroventricular injection in rats
American Journal of Neuroradiology, **1996**, *17*, 365-373

[56] Berriolo-Riedinger, A.; Touzery, C.; Riedinger, J.-M.; Toubeau, M.; Coudert, B.; Arnould, L.; Boichot, C.; Cochet, A.; Fumoleau, P. & Brunotte, F.
[18F]FDG-PET predicts complete pathological response of breast cancer to neoadjuvant chemotherapy
European Journal of Nuclear Medicine and Molecular Imaging, **2007**, *34*, 1915-1924

[57] Schwarz, J. D.; Bader, M.; Jenicke, L.; Hemminger, G.; Jaonicke, F. & Avril, N.
Early prediction of response to chemotherapy in metastatic breast cancer using sequential 18F-FDG PET
Journal of Nuclear Medicine, **2005**, *46*, 1144-1150

[58] Hicks, R.; Kalff, V.; MacManus, M.; Ware, R.; Hogg, A.; McKenzie, A.; Matthews, J. & Ball, D.
(18)F-FDG PET provides high-impact and powerful prognostic stratification in staging newly diagnosed non-small cell lung cancer
Journal of Nuclear Medicine, **2001**, *42*, 1596-1604

[59] Kurata, A.; Murata, Y.; Kubota, K.; Osanai, T. & Shibuya, H.
Multiple (18)F-FDG, PET-CT for postoperative monitoring of breast cancer patients
Acta Radiologica, **2009**, *50*, 979-983

[60] Sameni, M.; Dosescu, J.; Moin, K. & Sloane, B.
Functional imaging of proteolysis: stromal and inflammatory cells increase tumor proteolysis
Molecular Imaging, **2003**, *2*, 159-175

[61] Gauthier, M.; Pickering, C.; Miller, C.; Fordyce, C.; Chew, K.; Berman, H. & Tlsty, T.
p38 regulates cyclooxygenase-2 in human mammary epithelial cells and is activated in premalignant tissue
Cancer Research, **2005**, *65*, 1792-1799

[62] Schedin, P.; O'Brien, J.; Rudolph, M.; Stein, T. & Borges, V.
Microenvironment of the involuting mammary gland mediates mammary cancer progression
Journal of Mammary Gland Biology and Neoplasia, **2007**, *12*, 71-82

[63] Mueller, M. & Fusenig, N.
Friends or foes - bipolar effects of the tumour stroma in cancer
Nature Reviews- Cancer, **2004**, *4*, 839-849

[64] Radisky, D.; Kenny, P. & Bissell, M.
Fibrosis and cancer: do myofibroblasts come also from epithelial cells via EMT?
Journal of cellular Biochemistry, **2007**, *101*, 830-839

[65] Turk, H.; Camci, C.; Buyukberber, S.; Tuncozgur, B.; Sivrikoz, C.; Elbeyli, L. & Sari, I.
Superior vena cava syndrome caused by chemotherapy-induced fibrosis
Journal of Chemotherapy, **2002**, *14*, 417-419

[66] Callaway, M.; Tyrrell, C.; Williams, M. & Marshal, A.
Chemotherapy induced myocardial fibrosis
Clinical Oncology, **1994**, *6*, 55-56

[67] Isermann, R.; Grunwald, S.; Hatzung, G.; Könsgen-Mustea, D.; Behrndt, P.; Geaid, A.; Jäger, B. & Ohlinger, R.
Breast lesion sizing by B-mode imaging and sonoelastography in comparison to histopathological sizing--a prospective study
Ultraschall Med, **2011**, *32*, 21-26

[68] Bando, H.; Ishii, M.; Tohno, E. & Ueno, E.
Real time ultrasound elastography for monitoring tumour response to neoadjuvant chemotherapy in primary breast cancer
Journal of Clinical Oncology, **2007**, *25*

[69] Nitta, N.; Shiina, T. & Ueno, E.
Hysteresis parameter imaging of soft tissue under quasi-static deformation
IEEE Ultrasonics Symposium, **2003**, *2*, 1606-1609

[70] Bucciarelli, L. L.
Engineering Mechanics for Structure: Chapter 4 Stress, Strain, Stress-Strain
Dover, **2009**

[71] Hall, T. J.; Oberai, A. A.; Barbone, P. E.; Sommer, A. M.; Gokhale, N. H.; Goenezen, S. & Jiang, J.
Imaging the elastic nonlinearity of tissues
IEEE Ultrasonics Symposium, **2007**, 452-455

[72] T.Matsumura; T.Umemoto; Y.Fujihara; E.Ueno; M.Yamakawa; T.Shiina & T.Mitake
Measurement of elastic property of breast tissue for elasticity imaging
IEEE International Ultrasonics Symposium Proceedings, **2009**, 1451-1454

[73] Li, J.; Cui, Y.; Kadour, M. & Noble, J. A.
Elasticity reconstruction from displacement and confidence measures of a multi-compressed ultrasound RF sequence
IEEE Transactions on Ultrasonics, Ferroelectrics, and Frequency Control, **2008**, *55*, 319-326

[74] Fehrenbach, J.
Influence of Poisson's ratio on elastographic direct and inverse problems
Physics In Medicine And Biology, **2007**, *52*, 707-716

[75] Doyley, M.; Meaney, P. & Bamber, J.
Evaluation of an iterative reconstruction method for quantitative elastography
Physics In Medicine And Biology, **2000**, *45*, 1521-1540

[76] Doyley, M.; Srinivasan, S.; Pendergrass, S.; Wu, Z. & Ophir, J.
Comparative evaluation of strain-based and model-based modulus elastography
Ultrasound in Medicine & Biology, **2005**, *31*, 787-802

[77] Kallel, F. & Bertrand, M.
Tissue elasticity reconstruction using linear perturbation method
IEEE Transactions on Medical Imaging, **1996**, *15*, 299-313

[78] Oberai, A.; Gokhale, N.; Doyley, M. & Bamber, J.
Evaluation of the adjoint equation based algorithm for elasticity imaging
Physics In Medicine And Biology, **2004**, *49*, 2955-2974

[79] Lorenz, R. G. & Boyd, S. P.
Robust minimum variance beamforming
IEEE Transactions On Signal Processing, **2005**, *53*, 1684-1696

[80] Viola, F. & Walker, W. F.
Adaptive signal processing in medical ultrasound beamforming
IEEE Ultrasonics Symposium, **2005**, 1980-1983

[81] Kennedy, R. A.; Ward, D. B. & Abhayapala, T. D.
Nearfield beamforming using radial reciprocity
IEEE Transactions On Signal Processing, **1999**, *47*, 33-40

[82] Dantas, R. G.; Costa, E. T. & Leeman, S.
Ultrasound speckle and equivalent scatterers
Ultrasonics, **2005**, *43*, 405-420

[83] Xia, Z.-G. & Sheng, Y.
Radar speckle: noise or information?
IEEE Geoscience and Remote Sensing Symposium, **1996**, *1*, 48-50

[84] Tao, Z.; Tagare, H. & Beaty, J.
Evaluation of four probability distribution models for speckle in clinical cardiac ultrasound images
IEEE Transactions on Medical Imaging, **2006**, *25*, 1483-1491

[85] Revell, J.; Mirmehdi, M. & McNally, D.
Ultrasound speckle tracking for strain estimation
University of Bristol, Department of Computer Science, **2003**, http://www.cs.bris.ac.uk/Publications/Papers/2000106.pdf

[86] Palmeri, M. L. & Nightingale, K. R.
Acoustic radiation force-based elasticity imaging methods
Interface Focus, **2011**, *1*, 553-564

[87] Doyley, M. Model-based elastography: a survey of approaches to the inverse elasticity problem
Physics In Medicine And Biology, **2012**, *57*, 35–73

[88] Tanter, M.; Bercoff, J.; Athanasiou, A.; Deffieux, T.; Gennisson, J.-L.; Montaldo, G.; Muller, M.; Tardivon, A. & Fink, M.
Quantitative assessment of breast lesion viscoelasticity: Initial clinical results using supersonic shear imaging
Ultrasound in Medicine & Biology, **2008**, *34*, 1373-1386

[89] McAleavey, S.; Menon, M. & Elegbe, E.
Shear modulus imaging with spatially modulated ultrasound radiation force
Ultrasonic Imaging, **2009**, *31*, 217-234

[90] McAleavey, S. A.
Shear modulus imaging by spatially modulated ultrasound radiation force
IEEE International Ultrasonics Symposium Proceedings, **2009**, 487-490

[91] Fels, I. G.
Hydration and density of collagen and gelatin
Journal of Applied Polymer Science, **2003**, *8*, 1813-1824

[92] Suetens, P.
Fundamentals of Medical Imaging
Cambridge University Press, **ISBN: 0521803624**

[93] Mast, T. D.
Empirical relationships between acoustic parameters in human soft tissues
Acoustical Society of America, **2000**, *1*, 37-42

[94] Nightingale, K.; McAleavey, S. & Trahey, G.
Shear-wave generation using acoustic radiation force: in vivo andex vivo results
Ultrasound in Medicine and Biology, **2003**, *29*, 1715–1723

[95] Transient ultrasound radiation force elastography. Preliminary comparison with surface palpation elastography
IEEE Ultrasonics Symposium, **2006**, 1672-1675

[96] McKnight, A. L.; Kugel, J. L.; Rossman, P. J.; Manduca, A.; Hartmann, L. C. & Ehman, R. L.
MR elastography of breast cancer: preliminary results
American Journal of Roentgenology, **2002**, *178*, 1411-1417

[97] Venkatesh, S. K.; Yin, M.; Glockner, J. F.; Takahashi, N.; Araoz, P. A.; Talwalkar, J. A. & Ehman, R. L.
MR elastography of liver tumors: preliminary results
American Journal of Roentgenology, **2008**, *190*, 1534-1540

[98] Kruse, S. A.; Smith, J. A.; Lawrence, A. J.; Dresner, M. A.; Manduca, A.; Greenleaf, J. F. & Ehman, R. L.
Tissue characterization using magnetic resonance elastography: preliminary results
Physics In Medicine And Biology, **2000**, *45*, 1579–1590

[99] Sharma, A. C.; Soo, M. S.; Trahey, G. E. & Nightingale, K. R.
Acoustic radiation force impulse imaging of in vivo breast masses
IEEE Ultrasonics Symposium, **2004**, 728-731

[100] Athanasiou, A.; Tardivon, A.; Tanter, M.; Sigal-Zafrani, B.; Bercoff, J.; Deffieux, T.; Gennisson, J.-L.; Fink, M. & Neuenschwander, S.
Breast Lesions: quantitative elastography with supersonic shear imaging-preliminary results
Radiology, **2010**, *256*, 297-303

[101] Revell, J.; Mirmehdi, M. & McNally, D.
Combined ultrasound speckle pattern similarity measures
University of Bristol, Department of Computer Science, **2004**,
http://www.cs.bris.ac.uk/Publications/Papers/2000178.pdf

[102] Viola, F. & Walker, W. F.
A comparison of the performance of time-delay estimators in medical ultrasound
IEEE Transactions on Ultrasonics, Ferroelectrics and Frequency Control, **2003**, *50*, 392-401

[103] Chen, L.; Housden, R. J.; Treece, G. M.; Gee, A. H. & Prager, R. W.
A hybrid displacement estimation method for ultrasonic elasticity imaging
IEEE Transactions on Ultrasonics, Ferroelectrics, and Frequency Control, **2010**, *57*, 866-882

[104] Khadem, A. & Setarehdan, S. K.
Smoothing-spline based strain estimation in ultrasound elastography
IEEE International Conference on Signal Processing and Communications, **2007**, 680-683

[105] Nitta, N.; Shiina, T.; Ueno, E. & Yamakawa, M.
Real time tissue elasticity imaging using the combined autocorrelation method
Journal of Medical Ultrasonics, **2002**, *29*, 119-128

[106] Yamakawa, M. & Shiina, T.
Strain estimation using the extended combined autocorrelation method
Japanese Journal of Applied Physics, **2001**, *40*, 3872-3876

[107] Bae, U. & Kim, Y.
Angular strain estimation method for elastography
IEEE Transactions on Ultrasonics, Ferroelectrics, and Frequency Control, **2007**, *54*, 2253-2261

[108] Jiang, J. & Hall, T. J.
A generalized speckle tracking algorithm for ultrasonic strain imaging using dynamic programming
Ultrasound in Medicine & Biology, **2009**, *35*, 1863-1879

[109] Srinivasan, S.; Kallel, F.; Souchon, R. & Ophir, J.
Analysis of an adaptive strain estimation technique in elastography
Ultrasonic Imaging, **2002**, *24*, 109-118

[110] Deprez, J.-F.; Brusseau, E. & Basset, O.
3D strain imaging method adapted to large deformations and freehand scanning
IEEE International Ultrasonics Symposium Proceeding, **2008**, 544-547

[111] Deprez, J.-F.; Brusseau, E.; Schmitt, C.; Cloutier, G. & Basset, O.
3D estimation of soft biological tissue deformation from radio-frequency ultrasound volume acquisitions
Medical Image Analysis, **2009**, *13*, 116-127

[112] Viola & Jones
Robust real-time face detection
International Journal of Computer Vision, **2004**, *57*, 137–154

[113] Varghese, T.; Konofagou, E. E.; Ophir, J.; Alam, S. K. & Bilgen, M.
Direct strain estimation in elastography using spectral cross-correlation
Ultrasound in Medicine & Biology, **2000**, *26*, 1525–1537

[114] Hoyt, K.; Forsberg, F. & Ophir, J.
Comparison of shift estimation strategies in spectral elastography
Ultrasonics, **2006**, *44*, 99-108

[115] Jensen, J. A.
Simulation of advanced ultrasound systems using FIELD II
IEEE International Symposium on Biomedical Imaging, **2004**, *1*, 636 - 639

[116] Madsen, E.; Zagzebski, J. & Frank, G.
Oil-in-gelatin dispersions for use as ultrasonically tissue-mimicking materials
Ultrasound in Medicine & Biology, **1982**, *8*, 277-287

[117] Madsen, E. L.; Zagzebski, J. A.; Banjavie, R. A. & Jutila, R. E.
Tissue mimicking materials for ultrasound phantoms
Medical Physics, **1978**, *5*, 391-395

[118] Kadour, M. J.
Guide to making phantoms
Dept. Of Engineering Science, Oxford University, **2007**

[119] Chakraborty, A.; Bamber, J. C. & Dorward, N. L.
Slip elastography: A novel method for visualising and characterizing adherence between two surfaces in contact
Ultrasonics, **2012**, *52*, 364-376

[120] Varghese, T. & Ophir, J.
Estimating tissue strain from signal decorrelation using the correlation coefficient
Ultrasound in Medicine & Biology, **1996**, *22*, 1249-1254

[121] Lindop, J.; Treece, G.; Gee, A. & Prager, R.
An intelligent interface for freehand strain imaging
Ultrasound in Medicine & Biology, **2008**, *34*, 1117–1128

[122] Stark, J. A.
Adaptive image contrast enhancement using generalizations of histogram equalization
IEEE Transactions on Image Processing, **2000**, *9*, 889-896

[123] Kim, Y.-T.
Contrast enhancement using brightness preserving bi-histogram equalization
IEEE Transactions on Consumer Electronics, **1997**, *43*, 1-8

[124] Menotti, D.; Najman, L.; Facon, J. & de A. Araújo, A.
Multi-Histogram equalization methods for contrast enhancement and brightness preserving
IEEE Transactions on Consumer Electronics, **2007**, *53*, 1186-1194

[125] Han, J.-H.; Yang, S. & Lee, B.-U.
A novel 3-D color histogram equalization method with uniform 1-D gray scale histogram
IEEE Transactions on Image Processing, **2011**, *20*, 506-512

[126] Qiu, Y.; Sridhar, M.; Tsou, J. K.; Lindfors, K. K. & Insana, M. F.
Ultrasonic viscoelasticity imaging of nonpalpable breast tumors: preliminary results
Academic Radiology, **2008**, *15*, 1526-1533

[127] Sridhar, M.; Liu, J. & Insana, M.
Viscoelasticity imaging using ultrasound: parameters and error analysis
Physics In Medicine And Biology, **2007**, *52*, 2425-2443

[128] Sridharand, M. & Insana, M. F.
Ultrasonic measurements of breast viscoelasticity
Medical Physics, **2007**, *34*, 4757–4767

[129] Thukral, A.; Thomasson, D. M.; Chow, C. K.; Eulate, R.; Wedam, S. B.; Gupta, S. N.; Wise, B. J.; Steinberg, S. M.; Liewehr, D. J.; Choyke, P. L. & Swain, S. M.
Inflammatory breast cancer: dynamic contrast-enhanced MR in patients receiving bevacizumab—initial experience
Radiology, **2007**, *244*, 727-735

[130] Wenkel, E.; Geppert, C.; Uder, M.; Kiefer, B.; Bautz, W. & Janka, R.
Diffusion-weighted imaging in breast MRI, An easy way to improve specificity
Magnetom Flash (Siemens Medical Solutions), **2007**, *3*, 28-32

[131] American Cancer Society, "Detailed guide to breast cancer"
2011, *http://www.cancer.org/Cancer/BreastCancer/DetailedGuide/breast-cancer-staging*

[132] Kvitting, J.; Wigström, L.; Strotmann, J. & Sutherland, G.
How accurate is visual assessment of synchronicity in myocardial motion? An In vitro study with computer-simulated regional delay in myocardial motion: clinical implications for rest and stress echocardiography studies
Journal of the American Society of Echocardiography, **1999**, *12*, 698-705

[133] Doyley, M.; Bamber, J.; Fuechsel, F. & l. Bush, N.
A freehand elastographic imaging approach for clinical breast imaging: system development and performance evaluation
Ultrasound in Medicine & Biology, **2001**, *27*, 1347-1357

[134] Yeap, B.; Muniandy, S.; Lee, S.; Sabaratnam, S. & Singh, M.
Specimen shrinkage and its influence on margin assessment in breast cancer
Asian Journal of Surgery, **2007**, *30*, 183-187

[135] Christine L Carter, Carol Allen & Henson, D. E.
Relation of tumor size, lymph node status, and survival in 24,740 breast cancer cases
Cancer, **1989**, *63*, 181-187

[136] Bhatia, K. S. S.; Cho, C. C. M.; Yuen, Y.-H.; Rasalkar, D. D.; Ann D. King & Ahuja, A. T.
Real-time qualitative ultrasound elastography of cervical lymph nodes in routine clinical practice: interobserver agreement and correlation with malignancy
Ultrasound in Medicine & Biology, **2010**, *36*, 1990-1997

[137] Taylor, K.; O'Keeffe, S.; Britton, P.; Wallis, M.; Treece, G.; Housden, J.; Parashar, D.; Bond, S. & Sinnatamby, R.
Ultrasound elastography as an adjuvant to conventional ultrasound in the preoperative assessment of axillary lymph nodes in suspected breast cancer: A pilot study
Clinical Radiology, **2011**, *66*, 1064-1071

[138] Bottini, A.; Berruti, A.; Bersiga, A.; Brizzi, M.; Bruzzi, P.; Aguggini, S.; Brunelli, A.; Bolsi, G.; Allevi, G.; Generali, D.; Betri, E.; Bertoli, G.; Alquati, P. & Dogliotti, L.
Relationship between tumour shrinkage and reduction in Ki67 expression after primary chemotherapy in human breast cancer
British Journal of Cancer, **2001**, *85*, 1106–1112

[139] Sebag, F.; Vaillant-Lombard, J.; Berbis, J.; Griset, V.; Henry, J.; Petit, P. & Oliver, C.
Shear wave elastography for thyroid nodules
Clinical Thyroidology, **2011**, *23*, 7-8

[140] Lazarou, S.
Elasticity patterns of solid breast lesions with transient shear wave elastography
European Society of Radiology [online], **2010**, doi: 10.1594/ecr2010/C-0417

[141] Chang, J.; Moon, W.; Cho, N.; Yi, A.; Koo, H.; Han, W.; Noh, D.; Moon, H. & Kim, S.
Clinical application of shear wave elastography (SWE) in the diagnosis of benign and malignant breast diseases
Breast Cancer Research and Treatment, **2011**, *129*, 89-9

[142] Pernot, M.; Couade, M.; Mateo, P.; Crozatier, B.; Fischmeister, R. & Tanter, M.
Real-time assessment of myocardial contractility using shear wave imaging
Journal of the American College of Cardiology, **2011**, *58*, 65-72

[143] Tanter, M.; Pernot, M.; Montaldo, G.; Gennisson, J.-L.; Bavu, E.; Macé, E.; Nguyen, T.-M.; Couade, M. & Fink, M.
Real time quantitative elastography using supersonic shear wave imaging
IEEE International Symposium on Biomedical Imaging, **201**, 276-279

[144] Taylor, L. S.; Lerner, A. L.; Rubens, D. J. & Parker, K. J.
A kelvin-voight fractional derivative model for viscoelastic characterization of liver tissue
Proceedings of IMECE ASME International Mechanical Engineering Congress & Exposition, **2002**, 447-448

[145] Walker, W. F.; Fernandez, F. J. & Negron, L. A.
A method of imaging viscoelastic parameters with acoustic radiation force
Physics In Medicine And Biology, **2000**, *45*, 1437–1447